
Wayne State University Dissertations

January 2019

Analysis And Mitigation Of The Impacts Of Delays In Control Of Power Systems With Renewable Energy Sources

Chang Fu

Wayne State University, fk7408@wayne.edu

Follow this and additional works at: https://digitalcommons.wayne.edu/oa_dissertations

 Part of the [Electrical and Computer Engineering Commons](#)

Recommended Citation

Fu, Chang, "Analysis And Mitigation Of The Impacts Of Delays In Control Of Power Systems With Renewable Energy Sources" (2019). *Wayne State University Dissertations*. 2219.
https://digitalcommons.wayne.edu/oa_dissertations/2219

This Open Access Dissertation is brought to you for free and open access by DigitalCommons@WayneState. It has been accepted for inclusion in Wayne State University Dissertations by an authorized administrator of DigitalCommons@WayneState.

**ANALYSIS AND MITIGATION OF THE IMPACTS OF DELAYS IN
CONTROL OF POWER SYSTEMS WITH RENEWABLE ENERGY
SOURCES**

by

CHANG FU

DISSERTATION

Submitted to the Graduate School

of Wayne State University,

Detroit, Michigan

in partial fulfillment of the requirements

for the degree of

DOCTOR OF PHILOSOPHY

2019

MAJOR: ELECTRICAL ENGINEERING

Approved By:

Caisheng Wang

Date

Le Yi Wang

Feng Lin

Fengwei Zhang

© COPYRIGHT BY

CHANG FU

2019

All Rights Reserved

DEDICATION

This thesis is dedicated to my parents, my wife and all my teachers.

ACKNOWLEDGMENTS

I believe that Dr. Wang, my thesis advisor, molded my thought process as a researcher immensely. He also gave me tremendous support to go into a research area which is very new to me. Without his encouragements I may not be able to achieve whatever I have now as a researcher. Dr. Wang supported my Ph.D study and related research, for his patience, motivation, and immense knowledge. His guidance helped me in all the time of research and writing of this thesis. I will be always grateful to Dr. Wang for his nurturing and guidance, not only for my research, but also for making me an even better person.

I am extremely grateful to my thesis committee members: Dr. Le Yi Wang, Dr. Feng Lin, and Dr. Fengwei Zhang. They were always willing to give valuable suggestions, and feedback for making my research fruitful. Particularly their suggestion during my prospectus helped me in designing my thesis work in a more professional way. I would also like to thank Dr. Carol J. Miller for encouraging me throughout my research.

I would also like to express my gratitude to Dr. Di Shi, Dr. Zhe Yu, and other teammates for their warm guide and help during my internship. The warm of the group members makes the internship experience in California more colorful and fruitful.

I would also like to thank my lab-mates with whom I spent most of my life at Wayne State University. The discussions we had on the experimental parts on the implementation of different works help me a lot in my research. In particular, I would like to thank Zhongyang Zhao, Ishak O K, Ishan Jindal, Mohammad Ashraf Ali, Tingli Hu, A K George and Wasseem Al-Rousan. Wayne State University is truly a great place to do scientific work.

In conclusion, I would like to thank my family for everything. I would like to thank my father Gang Fu, mother Na Li for being with me in completing all my dreams, aspirations,

and wishes. Finally, a big thank to my wife Lu Bai, who stood as a pillar of support with love, care, and support throughout the journey.

TABLE OF CONTENTS

DEDICATION	ii
ACKNOWLEDGMENTS	iii
LIST OF FIGURES	viii
LIST OF TABLES	xi
CHAPTER 1: Introduction	1
1.1 Renewable Energy Worldwide and in the U.S.	1
1.2 Literature Review	3
1.2.1 Power System Composite Load Modeling	3
1.2.2 Control of Power Grid with Renewable Resources Connected	5
1.2.3 Active Power Control for Voltage Regulation	7
1.2.4 Delay in Control System	9
1.3 Motivation and Scope of Study	15
CHAPTER 2: Bayesian Based Composite Load Modeling	19
Nomenclature	19
2.1 Formulation	20
2.1.1 ZIP Model	21
2.1.2 IM Model	22
2.1.3 Composite Load	23
2.2 Bayesian Estimation in Composite Load Parameter Identification	25
2.2.1 Gibbs sampling	25
2.2.2 Gibbs in ZIP Model	27
2.2.3 Gibbs in IM models	30
2.3 Case Study	32

2.3.1	Composite Model Parameters Identification	32
2.3.2	Benchmarks & Comparison	35
CHAPTER 3:	PV Active Power Control with Communication Delays	42
3.1	Model of a grid-tied PV system with power control capability	42
3.2	PV Real power Control for Voltage Regulation	50
3.3	Controller Design to Compensate Communication Delays	53
3.3.1	Delay Margin	53
3.3.2	Controller Design with Single Communication Delays	54
3.3.3	Delay-Dependent Time-Invariant Stability Criterion	56
3.3.4	Time-varying Communication Delays	57
3.4	Simulation Study	59
3.4.1	Active Power Voltage Regulation using LMI	59
3.4.2	Delay-dependent Stability Criterion	60
3.4.3	Phase Lead Compensator	63
3.4.4	Switching System with Time-varying Delays	67
CHAPTER 4:	Load Frequency Control with Communication Delays	70
	Nomenclature	70
4.1	LFC Schemes with Communication Delays	71
4.1.1	One-area LFC Model	71
4.1.2	Multi-area LFC Model	74
4.2	Load Frequency Control Design with Communication Delay	77
4.2.1	Delay Margin	77
4.2.2	Compensator Design for One-area LFC with Communication Delay	78
4.2.3	Multi-area LFC with Communication Delays	79

4.3	Simulation Study	83
4.3.1	One-area LFC	83
4.3.2	Multi-area LFC	86
4.4	Discussion	90
4.4.1	Comparison with LMI Method	90
4.4.2	Couplings in Multi-area LFC Scheme	91
CHAPTER 5: Conclusion		94
BIBLIOGRAPHY		97
PUBLICATIONS		117
ABSTRACT		119
AUTOBIOGRAPHICAL STATEMENT		122

LIST OF FIGURES

Figure 1.1	Comparison of Bode plots for a delayed system and a delay free system.	11
Figure 2.1	The composite model of ZIP+IM.	21
Figure 2.2	The flowchart of proposed algorithm.	26
Figure 2.3	The 33bus test system for synthetic data.	33
Figure 2.4	The estimated parameters of the ZIP model.	34
Figure 2.5	Comparison of system active response between the original system and the estimated system.	35
Figure 2.6	The active power response comparison by using LS and GA.	36
Figure 2.7	Error of active power using GS, GA, LS with 10% measurement error.	37
Figure 2.8	Error of active power using GS, GA, LS with measurement anomalies.	39
Figure 2.9	The active power response at the same bus using composite and static load models.	40
Figure 2.10	The voltage response at the same bus using composite and static load models.	40
Figure 3.1	Schematic diagram of a grid-connected PV system.	43
Figure 3.2	Detailed model of the grid-connected PV system at bus j	44
Figure 3.3	PV I-V curve and the linearization of R_{pv}	44
Figure 3.4	The control loop with delay and compensator for bus j in the system.	49
Figure 3.5	Tested distribution network with six sub-communities.	50
Figure 3.6	Voltages at some nodes & comparison.	51
Figure 3.7	Control strategy implementation and comparison.	51

Figure 3.8	Voltage output at Node 6 with control strategy implemented to the small test system (communication delay $\tau = 0.3s$, $K_{I4} = 1$).	52
Figure 3.9	Bode plot for different K_{I4} .	54
Figure 3.10	Bode plot of the original system & compensated system using G_c .	55
Figure 3.11	Control performance when system switched before it is settled down.	57
Figure 3.12	Tested distribution network with six sub-communities.	60
Figure 3.13	Voltage and PV active power output at Node 6.	61
Figure 3.14	Relationships among τ_d , K_{P4} & K_{I4} .	62
Figure 3.15	Voltage profile at Node 6 with different communication delays.	62
Figure 3.16	Voltage output with different K_{I4} (time delay $\tau = 0.4s$).	64
Figure 3.17	Voltage output with different delays ($K_{I4} = 0.5$).	64
Figure 3.18	Output Voltage with $\tau = 0.4s$ with and without G_c .	64
Figure 3.19	PV-connected 33-bus test feeder.	65
Figure 3.20	Voltage magnitude profile at selected buses.	65
Figure 3.21	Output voltage at bus 21 with different delays in 33-bus test system.	65
Figure 3.22	Output voltage at bus 21 with/without the compensator ($\tau = 1.5s$).	66
Figure 3.23	Output voltage at bus 21 with/without the compensator ($\tau = 2s$).	66
Figure 3.24	Output voltage at bus 6 with different compensators (τ varies with respect to time).	68
Figure 3.25	Output voltage at bus 6 with/without the low pass filter (τ varies with respect to time).	69
Figure 4.1	One-area LFC scheme with communication delay.	72
Figure 4.2	Area i in a multi-area LFC scheme with communication delay.	75
Figure 4.3	Area 1 to the i th area of a multi-area LFC scheme.	80

Figure 4.4	A generic two-area LFC scheme.	81
Figure 4.5	Bode plot of the original system (Dash) and the compensated system (Solid).	84
Figure 4.6	One-area system response of 0.5s delay following a 0.2 p.u. load change using proposed compensator (Solid) and without compensator (Dash).	85
Figure 4.7	Proposed method in a 5-area system: a) Only a 4s communication delay is applied to Area 3, the delay in other areas are 0s. b) Each area has a communication delay: 4s, 5s, 4s, 6s, 3s, respectively.	87
Figure 4.8	10 area system LFC with random delay (Only three areas are shown. The time-varying random delays in these three areas are shown at the bottom of this figure).	89
Figure 4.9	The comparison of the proposed method and LMI method when the delay $\tau=4.0s$	90
Figure 4.10	Calculated $\ \mathbf{N}_n^{-1}\mathbf{\Delta}_n\ _\infty$ value and comparison, up to 15-area LFC.	92

LIST OF TABLES

Table 1.1	Worldwide Renewable Energy Capacity by Type [1].	1
Table 1.2	U.S. Renewable Energy Capacity by Type [1].	2
Table 1.3	Comparison of Centralized/decentralized Control Approach.	5
Table 1.4	Communication Delay with Respect to Different Communication Links [2].	13
Table 1.5	Wireless Communication Delays with Respect to Different Data Rate [3,4].	13
Table 2.1	Estimated and Real Value of the Parameters for ZIP+IM Model with 0 Measurement error.	36
Table 2.2	Estimated and Real Value of the Parameters for ZIP+IM Model with 10% Measurement Errors and Anomalies. (The value in the paren- thesis is the estimation error in percentage.)	37
Table 2.3	Composite Model Parameter Estimations without Measurement Er- ror by Different Methods. (The value in the parenthesis is the estimation error in percentage.)	38
Table 2.4	Composite Model Parameter Estimation with Different Methods Considering 10% Measurement Errors. (The value in the parenthesis is the estimation error in percentage.)	38
Table 2.5	Composite Model Parameter Estimations with Different Methods Considering Anomalies. (The value in the parenthesis is the estimation error in percentage.)	39
Table 3.1	Resident load profile	51
Table 3.2	Different Delay Margins with respect to K_{P4} & K_{I4}	61

Table 4.1	Parameters of One-area LFC Scheme	83
Table 4.2	Parameters of Five-area LFC Scheme	88

CHAPTER 1: INTRODUCTION

1.1: Renewable Energy Worldwide and in the U.S.

Energy collected from renewable resources such as sunlight, wind, rain, tides/waves, and geothermal heat, is called renewable energy. According to the Renewable Energy Policy Network for the 21st Century (REN21) [5], huge achievements in renewable energy development have been accomplished in the past decade. The renewable energy capacity has reached 2195 gigawatts (GW) worldwide by the end of 2017. The wind energy capacity increased from 467 GW in 2016 to 513 GW in 2017, and 100GW more solar energy capacity has been added since it reaches 300GW total capacity in 2016 [1]. The increasing of renewable energy worldwide by different types can be found in Table 1.1 [1].

Table 1.1: Worldwide Renewable Energy Capacity by Type [1].

	Hydropower(GW)	Solar(GW)	Wind(GW)	Total(GW)
2015	1210	224	416	1849
2016	1248	296	467	2012
2017	1270	390	513	2179

In the U.S., the renewable energy contributes around 12.2% of total energy consumptions in 2014. The renewable energy capacity increasing during the past three years in U.S. can be found in Table 1.2. In the past decade, the electricity generated by renewable energy has increased from 7.7% in 2001 to 15% in 2016 [6]. Hydropower, wind and solar power are the “3-big” renewable resources in generating electricity. The installed wind power capacity exceeds 75 GW in 2016 [6] with 226.5 terawatt-hours (TWh) energy generated in that year. Texas, Iowa and California led the wind power deployment in 2016. Solar power also contributes a big amount of electricity in recent years. According to the

U.S. Energy Information Administration (EIA), solar energy generated by distributed PVs in 2014, 2015, and 2016 are 11.2 TWh, 14.1 TWh, and 19.5 TWh, respectively [7].

Table 1.2: U.S. Renewable Energy Capacity by Type [1].

	Hydropower(GW)	Solar(GW)	Wind(GW)	Total(GW)
2015	101.54	23	72	195
2016	101.95	34	81	215
2017	102.13	42	87	229

The Department of Energy's (DOE's) National Renewable Energy Laboratory (NREL) estimates that by 2050, 80% of the electricity will be generated from renewable energy [8]. The 80% generation target is feasible with currently available technologies such as solar PVs, wind turbine, hydropower, concentrating solar power [9], etc. The DOE's SunShot program has a target to reduce the price of the solar energy to \$0.03/ kWh in utility-scale generation and reduce the electricity price from rooftop solar panels to \$0.05/kWh. This price is almost the 1/9 of the current PV price in utility size and 1/10 in residential size. It is foreseeable, with the declining of the price of the electricity generated by solar panel and other types of renewable energy, the installation and penetration of renewable energy will increase significantly. Consequently, some issues will rise with the increasing of the penetration of PVs and other renewable energy resources. For instance, the stability and reliability issues will rise in power systems, as well as energy management issue, particularly when the penetration level of PV and other renewable resources is high.

A lot of research focusing on addressing these related topics with the increasing of the renewable energy resources has been carried out, such as different control/optimization strategies. To validate different control approaches in different models, an accurate load

model is always necessary. Therefore, in this thesis, a robust time varying load modeling method will be proposed first to generate an accurate load model. Control approaches commonly used in power grid will also be investigated by considering renewable energy resources when there are delays. Delays can be generated either during control interfaces, e.g., control command sending from a central controller to a target plant, or communication channels and processes. Impacts of delays in active power control in a microgrid and load frequency control in bulk power systems will be studied as well. The literature review of these topics will be presented in the following sections.

1.2: Literature Review

In this section, literature review is carried out for the state of the art technologies used in load modeling, control of power grid with renewable energy resources connected, especially for active power voltage regulation for microgrids and distribution networks, as well as delay compensation in power systems.

1.2.1: Power System Composite Load Modeling

It is crucial to have a load model that can represent the dynamics and statics of the load accurately in power system research. Power system load models can be categorized into two types, i.e., static model and dynamic model, based on different mathematical representations of the relationships between power and voltage. Conventional static models include ZIP (constant impedance (Z), current (I) and power (P) model.) model, exponential model, frequency dependent model, *etc.*, and the induction motor (IM), exponential recovery load model (ERL) [10] are the major dynamic load models used in research studies recently. Different composite load models, such as Complex Load Model (CLOD), Western Electricity Coordinating Council (WECC) Composite Load Model (CLM), Artificial Neural Network-Based Modeling, *etc.*, were proposed in [11]. Among

these different load models, the composite load model of ZIP+IM can be implemented for various conditions, locations and compositions. It has been widely used in academic research and industry applications such as planning, operation and control of power systems [10, 12–16].

Load models are typically identified by component and measurement based approaches [10, 17–29]. Component based approaches highly rely on characteristics of components and compositions of load, and consequently, the computational cost is higher than measurement approaches. In order to obtain an accurate load compositions, behaviors of individual consumers are required. However, the accuracy of individual consumers is greatly affected by non-electric factors such as data and weather [10, 19]. In [19], the ZIP coefficients for widely used electrical appliances are determined by experiments, and the overall ZIP model was established with respect to the predetermined appliances. The difficulty in obtaining load composition information is another factor to be considered when implementing component based identification approach. It is reported in [30] that to obtain consumption information of all electrical components in a power system is the most challenging task in such approach.

Measurement-based approaches, such as least-squares (LS) and genetic algorithm (GA), are another mainstream for load parameter identification. Different techniques are reported in [21, 31] to identify the parameters for composite load models. In [30], a robust time-varying load parameters identification approach was proposed by using batch-model regression in order to obtain the updated system parameters. One disadvantage of the measurement based approach is the dependence on data quality. Measurement anomalies and outliers may affect the robustness of estimation in both time-varying and time-invariant load models [30]. Moreover, these approaches only estimate the expected

value of coefficients, and provide the point estimations of parameters, which may not be able to accommodate the characteristics of the ever changing power system accurately.

1.2.2: Control of Power Grid with Renewable Resources Connected

Active control strategies can be developed for power grid control with renewable energy resources connected [32]. For instance, in [33], a hierarchical control structure for microgrid was introduced. In such structure, the primary control performs the control of local power and voltage while voltage and frequency restoration is taken care of by the secondary level control. The tertiary level control usually carries out optimization of the microgrid. Centralized and decentralized control are two different approaches to implement the grid control implementation. The advantages and disadvantages by implementing centralized/decentralized control are listed in Table 1.3. In [34], a novel current

Table 1.3: Comparison of Centralized/decentralized Control Approach.

	Computational cost	Communication facilities cost	Flexibility	Reliability	Implementation difficulty
Cent.	High	High	Low	Low	Low
Dece.	Low	Low	High	High	High

control method is proposed to control both active and reactive power flows from a renewable energy source feeding a microgrid system through a single-phase parallel-connected inverter. A decentralized power management and a sliding model control strategy considering renewable energy were proposed in [35]. Other methods such as droop control, adaptive droop control, were proposed in [36,37] for voltage regulation, frequency control, etc., due to the fact that droop control can better coordinate the distributed generators, e.g.,

solar panel, wind turbine, among parallel-connected inverters.

Voltage regulation is one of the main targets of implementing control strategies for the power grid since a poor voltage profile may lead to many issues such as power quality, equipment safety, system reliability and stability, and thus can raise system losses and cause equipment damages. Moreover, the power quality and system reliability issues caused by the increasing penetration level of PVs and other renewable resources in distribution networks can limit the accommodation capability of power networks. Voltage regulation, especially for overvoltage issues in low voltage feeders, is one of the most urgent issues to be addressed [38–41]. The disadvantages of overvoltage have been widely investigated in [42]. Overvoltage issues limit the installation of PVs and may require extral energy storage systems (ESSs) to manage the surplus energy . Using ESSs is a very efficient approach, however, the costs of such devices are expensive and the cost benefit ratio is low at the current stage. Related research can be found in [42], where a coordinated control of distributed ESSs with traditional voltage regulator including the on-load tap changer transformers (OLTC) was proposed. Moreover, in contrast, if the numbers of ESSs are insufficient, the overvoltage issue may still occur. Demand-side management can help further increase the penetration level of renewables; however, only system owners are able to put them into practice. In [43], a method was introduced to reduce the secondary low voltage by adjusting the transformer tap. However, the tap positions cannot change frequently. There has to be a setting need to be found so that it can be used for rated and no generation of PV without violating the voltage limits. In [44], PV capacity limitation method is carried out to keep the voltage in an acceptable range, but this method may not be the best solution since there will be a significant amount of energy to be wasted.

It is worth noticing that in the past 5 years, with the acceleration of the processor operation capability, it is possible now to implement advanced control schemes, such as embedding the Artificial intelligent (AI), into the control system. By using some AI technologies, such as deep learning and reinforcement learning, the power system may be able to learn from the predefined decisions and eventually be able to make the decision by itself. Some pioneers have already implemented some machine learning method into power system. For instance, the usage of Q learning has been reported in the voltage control and AGC control in [45,46]. Wind power also benefits from such technology and related study was reported in [47].

Besides these approaches, significant amount of research efforts have been focused on active power curtailment to improve the voltage profile recently, which will be reviewed in the following sub-section.

1.2.3: Active Power Control for Voltage Regulation

Due to the stochastic characteristic of solar irradiance, the output power of the PV panels is somehow unpredictable and uncontrollable [48]. It was reported in [49] that with the increasing of the PV penetrations, the weather change will significantly vibrate the voltage profile. It is highly possible that the voltage profile will exceed the maximum threshold value when the solar irradiance is high and the load level is relatively low, especially in a system with a high penetration of PVs. Analysis was done in [50] to address the possibilities of voltage increasing towards the end of the distribution feeders due to higher line impedance. Define the power loss at the transmission line as L , the active and reactive power flowing away from bus as P and Q , respectively, the complex impedance of the transmission line as $r + jx$, then the following equations can be derived

$$L = r \cdot \frac{P^2 + Q^2}{V_0^2} \quad (1.1)$$

$$\Delta V = -\frac{rP + xQ}{V_0} \quad (1.2)$$

From 1.1, the minimum power loss through the transmission line requires the reactive power equals 0. According to 1.2, due to the high R/X ratio in low voltage networks, the real power fluctuation brings a proportional change of voltage. Since the active power control approach does not increase the device ratings of PV systems, and does not require system upgrades or extra reactive power compensation equipment, it has been accepted by utilities and customers [3, 51–66]. In [51], a droop based active power curtailment strategy was proposed. The global voltage sensitivity matrix information is used to analyze the impact of the change of the active power and to design a shared active power curtailment scheme among all PVs [51]. The active power injected by the inverter can be represented by 1.3:

$$P_{inv} = P_{MPPT} - m(V - V_{cri}) \quad (1.3)$$

where P_{MPPT} is the maximum power point under the corresponding solar irradiance and temperature, m is the droop factor, V_{cri} is the threshold value that the decreasing power injection starts. An equal output power curtailment method was carried out based on the voltage sensitivity matrix [52].

An adaptive real power capping method was proposed in [52], in which, a consensus based method was presented to regulate the PVs outputs adaptively so that each of the PV units in the network shares the equal curtailment responsibility without knowing the global information of the system. This approach can maximize the PV output without requiring global information and can be implemented either in a centralized supervisory

control or in a distributed way via consensus control [52]. In [67], the maximum active power can be injected to the grid is shown in 1.4:

$$P_{DK_k}^m = \frac{\Delta V_m}{J_{PQ_{mk}}} \quad (1.4)$$

where $P_{DK_k}^m$ is the maximum active power of the m th distributed generator, $J_{PQ_{mk}}$ is calculated real power according to 1.5. The $J_{RPV_{m,k}}^{-1}$ and $J_{RQV_{m,k}}^{-1}$ are calculated based on 1.6, and can be found in 1.7 and 1.8. ΔV_m represents the voltage difference between the voltage limit V_m and the real voltage V_0 .

$$J_{PQ_{mk}} = J_{RPV_{m,k}}^{-1} + J_{RQV_{m,k}}^{-1} \tan[\cos^{-1}(pf_k)] \quad (1.5)$$

$$\begin{bmatrix} \Delta P \\ \Delta Q \end{bmatrix} = \begin{bmatrix} J_{P\theta} J_{PV} \\ J_{Q\theta} J_{QV} \end{bmatrix} \begin{bmatrix} \Delta \theta \\ \Delta V \end{bmatrix} \quad (1.6)$$

$$\Delta P = (J_{PV} - J_{P\theta} J_{Q\theta}^{-1} J_{QV}) \Delta V = J_{RPV} \Delta V \quad (1.7)$$

$$\Delta Q = (J_{QV} - J_{Q\theta} J_{P\theta}^{-1} J_{PV}) \Delta V = J_{RQV} \Delta V \quad (1.8)$$

1.2.4: Delay in Control System

Different types of control methods have been introduced in the previous section. However, most of those approaches are studied based on the assumption that the control signals and all the measurements are obtained, processed and delivered in an ideal communication environment with no time delays. Time delay always exists in a communication network, affecting the veracity and accuracy of information exchange and may degrade any control procedures chosen to stabilize the power grid [51, 68–73]. The delayed signal received by the controllers, as well as the signal sent by the controllers will not be able to

be executed by the corresponding equipment effectively. Due to the delay in the control loop, it makes the controller design much more complicated and inapplicable for some classical methods [74]. Moreover, due to large numbers of components in distribution networks, it is not economically feasible to have dedicated channels for communications among local control devices and between local control devices and the central controller. For communications over a shared channel, delays and losses are inevitable, which introduce a great challenge for the control of distribution networks with high penetration of PVs.

For a given delay $\tau(t)$, the delayed system can be represented as $x(t - \tau(t))$. Delays can be categorized into constant delays and time-varying delays, as shown in 1.9:

$$\tau(t) = \begin{cases} \tau, & \text{Constant Delay} \\ \tau(t), & \text{Time - varying} \end{cases} \quad (1.9)$$

The Laplace transform for a given constant delay $x(t - \tau)$ can be written as: $\mathcal{L}x(t - \tau) \leftrightarrow e^{-\tau s} X(s)$ where $X(s)$ is the Laplace transform of $x(t)$.

Effect of Delays on Closed-loop System Dynamics

For an open-loop system, the system with delay can be written as: $X_d(s) = X(s)e^{-\tau s}$.

The transfer function $X(s)$ is assumed to be stable. The frequency response of X is:

$$X_d(j\omega) = |X(j\omega)|e^{j(\angle X(j\omega) - \omega\tau)} \quad (1.10)$$

As we can see, the magnitude of $X_d(j\omega)$ is not effected by the delay. However, an additional phase lag in $X_d(j\omega)$ is introduced. This phase lag grows proportionally with the frequency ω and τ . In the Bode diagram of the system, the magnitude plot does not change, according to 1.10, but the phase plot is shifted down by $\frac{180}{\pi}\omega\tau$ degrees, which shows an exponentially decreasing in the logarithmic scale. Fig. 1.1 shows the impact of

delay in the Bode plot of a typical load frequency control. The solid line is the system Bode plot without delay. In comparison, the dash line shows the delayed system. As aforementioned, there is no difference in the magnitude of the two systems. However, the phase drops significantly when a 0.3s delay is added to the system: the phase drops to around -2000 degree with 100 rad/s frequency. In contrast, the phase is -180 degrees at 100 rad/s when $\tau = 0$.

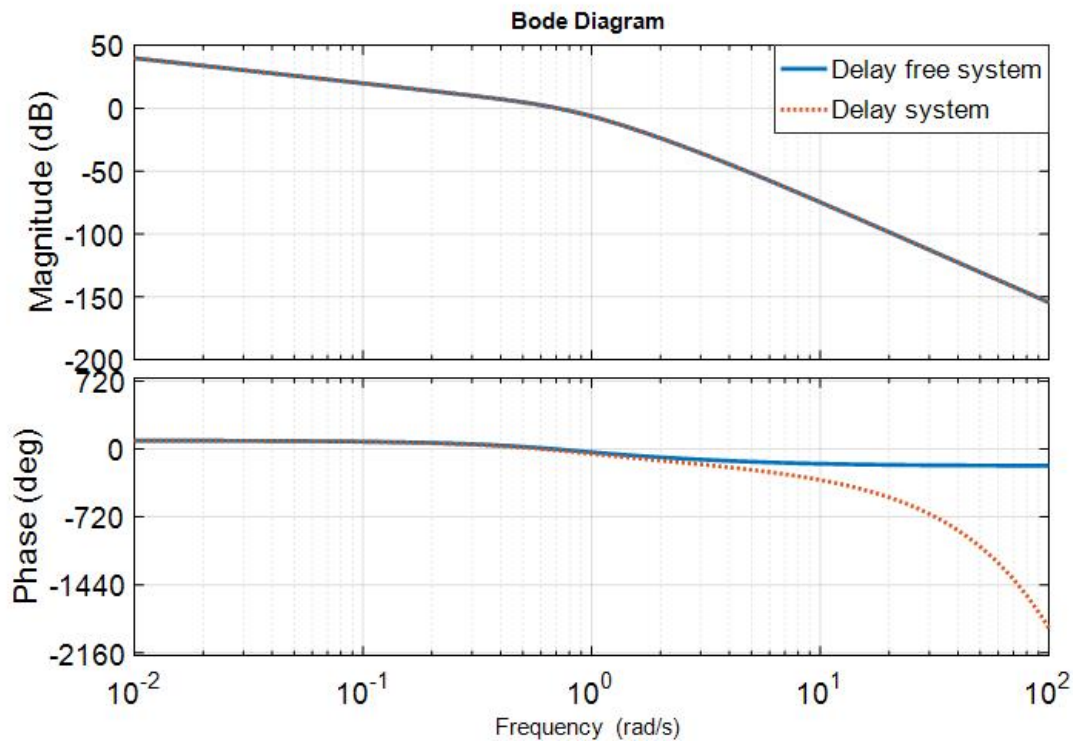


Figure 1.1: Comparison of Bode plots for a delayed system and a delay free system.

From the state space point of view, a typical state space representation of a system can be written as:

$$\begin{cases} \dot{x}(t) = Ax(t) + Bu(t) \\ y(t) = Cx(t) + Du(t) \end{cases} \quad (1.11)$$

where A, B, C, and D is the system matrix with appropriate dimensions. The state space in 1.11 is called history accumulator, which means one can get the future outputs with

knowing the future inputs. The knowledge of previous input is not required. However, in the delayed system, at a specified time t_0 , the input $u(t_0)$ is not sufficient to calculate $\dot{x}(t_0)$ without considering the knowledge of the input with the historical data, which is $(t_0 - \tau, t_0)$. Thus, the delayed system can be written as:

$$\dot{x} = Ax(t) + A_d x(t - \tau(t)) + Bu(t) \quad (1.12)$$

Delays in Power System Control

In automatic generation control, a protocol for synchro-phasor measurement communication used in wide area measurement system (WAMS) was defined in IEEE Standard C37.118 [75]. According to [76], the communication delay in distribution system is usually less than 10 ms. But in wide-area power system, this value may vary [77–81]. In the Bonneville Power Administration (BPA) system, the communication delay of fiber optic digital system researches 38 ms for one way, and the potential delay in the modems are over 80 ms [82]. In reality, communication delays may vary due to the large number of factors such as network traffic, re-transmission due to the transmission errors, etc. [83–91]. The delay usually reaches the order of 100ms in a wide-area power system for closed-loop control. The delay may be even longer if multiple signals are routed in the system. Table 1.4 lists the communication delays with respect to different communication links [92–94].

Wireless communication has been becoming more and more popular and widely used in power system communication recently due to its flexibility and cost saving in development and maintenance . In [2], the typical latency with respect to different data rate was studied (shown in Table 1.5). Latency is the time it takes for a packet to travel from the measurement to the destination and back. According to [95], the delay in large LFC systems can reach 15s with the utilization of open and distributed communication links as well.

Table 1.4: Communication Delay with Respect to Different Communication Links [2].

Communication link	Associated delay one way (milliseconds)
Fiber-optic cables	50-100
Digital microwave links	100-150
Power line (PLC)	150-350
Telephone lines	200-300
Satellite link	500-700

Table 1.5: Wireless Communication Delays with Respect to Different Data Rate [3, 4].

Data Rate (average)	Latency (average)
Low: < 500 kbps	<250ms
Moderate: 500 kbps-1500 kbps	250ms-1s
High: >1500 kbps	>1s

In [3, 61] typical communication delays among different devices and with respect to different data rates were studied in wired and wireless communication channels, respectively. The communication delays in a relatively small distribution network are normally smaller than 1s while for a relatively larger system, particularly with wireless communication, the delay can go over 1s. For instance, the maximum delay in a real system was found to be around 600 ms in an area of 2-mile radius with a wired communication scheme [3]. According to [4], depending on the data rate, the maximum communication delay in a wireless network can reach over 1.5s when the average data rate is higher than 1500 kbps.

Communication delays can also happen in load frequency control. LFC has been

widely used in maintaining the balance between the load and generation in a specified control area and a large interconnected power system with multiple control areas over a wide region [96]. Dedicated communication channels have been used to transmit control signals between remote terminal units (RTUs) and a control center in a typical centralized LFC design. In such a traditional control scheme, most previous research work has ignored the problems due to communication delays [97]. Moreover, with the development of electricity market, the control processes involved in ancillary services require an open communication infrastructure that can rapidly respond to customers and utilities with large amounts of information exchanges [98]. How to efficiently integrate all the information, such as control, computing and communication, under deregulation and market environment [99] has drawn lots of attention. It is urgent to have an open framework that fully considers communication delays to support such rising control needs. For instance, as introduced in [98], a new communication framework called GridStat has been introduced for data sharing. In this system, the impact of communication delays should be considered and carefully analyzed in order to maintain a secure and effective power system and market.

In order to mitigate negative impacts of delays, various research efforts have been carried out recently [43, 44, 67, 83, 100–102]. An event-trigger control method was introduced in [100] to update the PI controller parameters regarding different communication delays. In [102], a model predictive controller and a Smith predictor-based controller were proposed to overcome delays in communication channels in frequency restoration in an islanded microgrid. These delays usually range from milliseconds or tens of milliseconds, which are small compared to those that can happen in a large area LFC system. A networked predictive control approach considering the round-trip time delay in the feedback

loop [103] was studied in [104] in wide area damping control for power system inter area oscillations. However, this approach requires the information of the entire system and thus can be computationally intensive for a large system.

Linear matrix inequality (LMI) based methods have been studied in power systems with communication delays mainly on frequency control. A frequency regulation controller was designed in [97] based on an asymptotically stable LMI constraint illustrated in [105]. The same LMI stability criterion was also used in [99] to design different controller parameters under different communication delays. A multi-agent-system (MAS) based distributed control strategy for radial dc microgrids considering transmission time delays was presented in [98]. The proposed controller was designed based on solving LMIs. An LMI based method provides a sufficient condition of stability in controller design. In other words, if the LMI stability criterion is not met, it is still not clear whether the system is stable or not. Moreover, it does not tell us how to design the controller. For distribution networks with high penetration of PVs, it is necessary to have a controller that can guarantee the systems' stability and performance while the systems are subject to various disturbances (load and solar irradiance variations) and communication delays.

1.3: Motivation and Scope of Study

First, an accurate load model is essential for power system analysis, especially for system stability and reliability analysis [106–110]. In this thesis, an time-varying robust load model identification method will be developed. As introduced in Section 1.2, traditional load modeling methods, such as using maximum likelihood estimation method, can only provide point estimations. However, in reality, such estimations may have limits to accommodate the characteristics of the ever-changing power system. Therefore, it is necessary to develop a method that can better represent the attributes of the power system,

especially the load, to carry out more accurate analysis and produce more meaningful results.

In this thesis, Bayesian estimation (BE) [55] based composite load parameter identification approaches will be investigated since they can provide distributions of each parameter and overcome the disadvantages in traditional load modeling technologies. BE is a distribution estimation rather than point estimation, which provides the likelihood of each parameter within a certain range. In this case, this method can provide accurate estimation of the parameters in both time invariant and time-varying cases. BE does not require the information of load compositions, nor coefficients of appliances. The estimations rely on the observations or measurements, such as active power, reactive power, bus voltage, etc., as well as expert opinions. BE is a robust estimation method due to its statistical characteristics: measurement anomalies and outliers will not significantly affect the results if the number of samples is large enough, and the effect of measurement error is also mitigated. The study of BE based load modeling is given in Chapter 2. Detailed advantages can be found in following chapters.

Second, the active power control in power systems with renewable resources connected is also important for the network management (such as voltage regulation) and becomes critical when the penetration level of renewable resources is high. Communication delays are inevitable in power systems that either cover large areas at transmission level or contain a large number of components at the distribution level. It is necessary and important to study the impact of delays in the system, especially when there is centralized control framework exists. The model used for analyzing delay impacts plays an important role in the whole, and therefore should be: (1) simple enough to be studied and can be used in other related research efforts, (2) can represent the characteristics of the real

system and thus the analysis based on the model is correct and representative.

The last but not the least, according to the literature review, although there have been many delay related research efforts in control theory, the study on the control of renewable integrated power systems with delays is still limited and deserves more investigations. The most frequently used approach is LMI based methods [97–99,105], and it has been studied for LFC control with communication delays. However, the LMI based methods have a common drawback in only providing a sufficient condition, which is not enough from the control perspective. It is necessary and of great practical importance to determine a sufficient and necessary condition for designing a delay compensator controller for power systems with renewable generation sources.

Therefore, in this thesis, studies will be focused on the BE based composite load modeling, as well as control the design for voltage regulation and LFC with communication delays considered. In Chapter 2, a probabilistic parameter estimation method for composite load models, i.e. ZIP and IM model, will be carried out. This method is a time-varying estimation approach, and it is robust to measurement errors and outliers. The comparisons by using the traditional composite load model estimation method and the BE based approach will be studied as well. In Chapter 3, an active power control approach for voltage regulation considering communication delays will be proposed. A delay compensator is designed to mitigate the impacts of delay by increasing the delay margin of the system. The method also works with multiple PVs and other renewable resources connecting in the distribution network. Same delay compensator design strategy is also used in LFC control considering communication delays in Chapter 4. By implementing small gain theorem, it can be proven that, if certain criterion can be satisfied, the design of the delay compensators in a multi-area LFC scheme can be treated in the way as the

design of compensators in each area separately without using the information from other areas.

CHAPTER 2: BAYESIAN BASED COMPOSITE LOAD MODELING

Nomenclature

α_i	Parameter of ZIP model, active power coefficients: α_1 to α_3 , reactive power coefficients: α_4 to α_6 .
e	Estimated value.
E'_d, E'_q	d-axis and q-axis of transient EMF.
H	Inertia constant of induction motor.
i_d, i_q	d-axis and q-axis of stator current.
m	Measurement value
P	Active power of ZIP+IM load.
P_{ZIP}	Active power of ZIP load.
P_{ZIP0}	Initial active power of ZIP load.
P_{IM}	Active power of induction motor model.
Q	Reactive power of ZIP+IM load.
Q_{ZIP}	Reactive power of ZIP load.
Q_{ZIP0}	Initial reactive power of ZIP load.
Q_{IM}	Reactive power of induction motor model.
R_r	Rotor resistance.
R_s	Stator resistance.
T_0	Initial load torque.
U_d, U_q	d-axis and q-axis bus voltage.

V_0	Nominal voltage.
X_m	Magnetizing reactance.
X_s	Stator reactance.
X_r	Rotor reactance.
λ_p, λ_q	Proportions of ZIP load in active and reactive power
ε	Distribution of measurement error.

2.1: Formulation

In this chapter, a composite load model consisting of a ZIP and an IM sub-model is introduced [12], followed by the formulation of a composite model identification method by using Gibbs Sampling (GS). The derivation steps and assumptions in the proposed parameter estimation method, the updating strategy are introduced in this chapter as well.

The introduction of different composite load models can be found in Chapter 1. In this thesis, the well-known ZIP+IM model is selected, and the identification processes are developed based on this model. A composite load represented by the ZIP+IM model is shown in Fig. 2.1, in which the ZIP model models the steady-state behavior and the IM model corresponds to the dynamic process of the load. The mathematical representations of the ZIP and IM model are given in 2.1 and 2.2, respectively.

$$\begin{cases} P_{ZIP} = P_{ZIP0}(\alpha_1 \bar{V}^2 + \alpha_2 \bar{V} + \alpha_3), \\ Q_{ZIP} = Q_{ZIP0}(\alpha_4 \bar{V}^2 + \alpha_5 \bar{V} + \alpha_6), \end{cases} \quad (2.1)$$

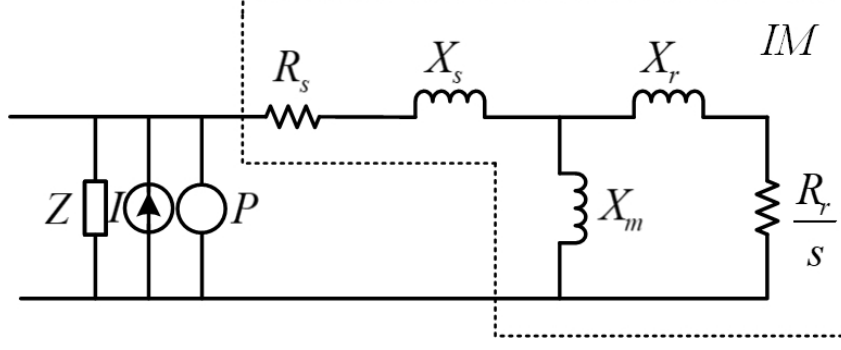


Figure 2.1: The composite model of ZIP+IM.

$$\left\{ \begin{array}{l} \frac{dE'_d}{dt} = -\frac{1}{T'}[E'_d + (X - X')I_q] - (\omega - 1)E'_q \\ \frac{dE'_q}{dt} = -\frac{1}{T'}[E'_q - (X - X')I_d] + (\omega - 1)E'_d \\ \frac{d\omega}{dt} = -\frac{1}{2H}[(A^2\omega + B\omega + C)T_0 - (E'_d I_d + E'_q I_q)] \\ I_d = \frac{1}{(R_s^2 + X'^2)}[R_s(U_d - E'_d) + X'(U_q - E'_q)] \\ I_q = \frac{1}{(R_s^2 + X'^2)}[R_s(U_q - E'_q) - X'(U_d - E'_d)] \end{array} \right. \quad (2.2)$$

The parameters identified in this composite model are $\alpha_1 \dots \alpha_6$, $\sum_{i=1}^3 \alpha_i = 1$, $\sum_{i=4}^6 \alpha_i = 1$, X_m , X_r , X_s , R_r , A , B , C , H . Some notations in equations (2.1) and (2.2) are defined as follows:

$$X' \triangleq X_s + X_m X_r / (X_m + X_r),$$

$$X \triangleq X_s + X_m,$$

$$T' \triangleq (X_r + X_m) / R_r$$

2.1.1: ZIP Model

The ZIP model describes how the power of load changes as voltage varies in the steady-state condition. The ZIP model is formulated in (2.1), where $\bar{V} = V/V_0$. When voltage V deviates from V_0 , real and reactive power of the load is assumed to follow a quadratic model. As the real power and reactive power follow the same type of model, we will discuss only the real power as an example in the following. The estimation of

coefficients for the reactive power will follow the same procedure.

Define $y[t] = P[t]/P_0$, $x[t] = V[t]/V_0$, where $P[t]$ and $V[t]$ are the t th measurements of the real power and voltage magnitude of the ZIP load. The following assumptions are made in the identification process:

- The measurement noise follows a normal distribution, *i.e.*,

$$y[t] = \alpha_1 x[t]^2 + \alpha_2 x[t] + \alpha_3 + \varepsilon[t], \text{ where } \varepsilon[t] \sim \mathcal{N}(0, 1/\tau), \text{ and } 1/\tau \text{ is the variance.}$$

The reasons for making this assumption are: 1) According to the law of large numbers, a normal distribution would be the best one to represent the characteristics of the noise if the number of experiment is large enough. 2) Since normal distribution is a conjugate distribution, it is easy for updating model parameters when implementing Gibbs sampling.

- Total number of n independent and identically distributed (i.i.d.) samples are drawn, namely $(\mathbf{x}, \mathbf{y}) \triangleq \{(x[1], y[1]), \dots, (x[n], y[n])\}$. Thus, take the active power for instance, the likelihood of observing x, y given by $\alpha_1, \alpha_2, \alpha_3, \tau$ can be written as:

$$L(\mathbf{x}, \mathbf{y} | \alpha_1, \alpha_2, \alpha_3, \tau) \propto \prod_{t=1}^n \exp[-(y[t] - \mu[t])^2 \tau / 2], \quad (2.3)$$

where $\mu[t] \triangleq \alpha_1 x[t]^2 + \alpha_2 x[t] + \alpha_3$, is the mean value of the observations.

2.1.2: IM Model

The dynamic part of load is usually represented by an IM model. The mathematical representation of such model can be found in (2.2).

The parameters to be identified in the IM model are: $X_r, X_m, X_s, R_r, R_s, A, B, C, H$. Typically, A is assumed to be 1 as the mechanical torque is assumed to be proportional to the square of the rotation speed of the motor [22]. B and C are both equal to 0. For simplicity, define $y_{Ed} \triangleq dE'_q/dt$, $y_{Eq} \triangleq dE'_d/dt$, $y_\omega \triangleq d\omega/dt$, $y_{Id} \triangleq I_d$, $y_{Iq} \triangleq I_q$, $\beta_1 \triangleq$

$$-1/T', \beta_2 \triangleq -(X - X')/T', \beta_3 \triangleq -T_0/2H, \alpha_b \triangleq R_s/(R_s^2 + X'^2), \alpha_c \triangleq X'/(R_s^2 + X'^2).$$

Assuming that the measurement noise is i.i.d. and follows a normal distribution, we can rewrite the IM model as follows:

$$\begin{cases} y_{E_d}[t] = \beta_1 E'_d[t] + \beta_2 I_q[t] - (\omega - 1)E'_q[t] + \varepsilon_{E_d}[t] \\ y_{E_q}[t] = \beta_1 E'_q[t] - \beta_2 I_d[t] + (\omega - 1)E'_d[t] + \varepsilon_{E_q}[t] \\ y_\omega[t] = \beta_3(\omega^2 - E'_d[t]I_d[t] - E'_q[t]I_q[t]) + \varepsilon_\omega[t] \\ y_{I_d}[t] = \alpha_b(U_d[t] - E'_d[t]) + \alpha_c(U_q[t] - E'_q[t]) + \varepsilon_{I_d}[t] \\ y_{I_q}[t] = \alpha_b(U_q[t] - E'_q[t]) + \alpha_c(U_d[t] - E'_d[t]) + \varepsilon_{I_q}[t] \end{cases} \quad (2.4)$$

where $\varepsilon_{E_d}[t], \varepsilon_{E_q}[t], \varepsilon_\omega[t], \varepsilon_{I_d}[t], \varepsilon_{I_q}[t]$ all follow normal distributions with means equal 0, variances equal $1/\tau_E, 1/\tau_E, 1/\tau_\omega, 1/\tau_I, 1/\tau_I$, respectively.

2.1.3: Composite Load

For a composite load with ZIP+IM model, the total active power and reactive power of the load can be respectively computed as:

$$P = \lambda_p P_{ZIP} + (1 - \lambda_p) P_{IM}$$

$$Q = \lambda_q Q_{ZIP} + (1 - \lambda_q) Q_{IM}$$

The weights λ_p and λ_q represent the percentage of the static part of the active and reactive power of the load, respectively. As a result, the weights of the dynamic part of the active and reactive power are $(1 - \lambda_p)$ and $(1 - \lambda_q)$, accordingly. Since the available data that can be used for identification of aforementioned parameters is limited by the fact that the composite model proposed in Fig. 2.1 is an equivalent model, some of the parameters are not able to be directly measured, such as E'_d, E'_q, ω , etc. Thus, it is challenging to identify all the parameters by only using P, Q and U, especially for parameters in equation (2.2). Therefore, in [11] and other load modeling papers, such problems were considered as optimization problems. The procedures of a widely used parameter identification method

presented in [11,18] are summarized as follows: 1. Typical values of some parameters, e.g., R_s, X_m, X_r , were selected to estimate I_d and I_q in 2.2, and the values of I_d and I_q are substituted back to the first three equations in (2.2) to calculate the values of E_d, E_q, ω . 2. By using the value calculated in step 1, an optimization problem will be solved subject to (2.5), and the coefficients of each term will be identified. If (2.5) is smaller than the predefined threshold value, the identification procedure will be terminated, the solution of the optimization problem will be the estimates of each parameters in (2.2). Otherwise, a new typical value will be selected to follow the same steps until the threshold is met.

$$\min [(P^m - P^e)^2 + (Q^m - Q^e)^2] \quad (2.5)$$

Other than the aforementioned optimization based algorithm, in this thesis, a BE based method is proposed without optimizing the error between the measured value and the estimated value. The proposed algorithm in Fig. 2.2 is inspired by the traditional method by with some differences: The initial active power consumed by ZIP part is calculated by using priors, which are typically some expert opinions or hypotheses of the portion of the static load. The results of calculated E'_d, E'_q, ω are used in GS to sample the parameters in 2.2, and the sampled values are used to calculate the updated value of P_{IM} by using 2.6, and P_{ZIP} by using 2.1. The updated value of P_{IM} and P_{ZIP} will be used in the next iteration as the updated values of the parameters. The detailed steps of this algorithm can be found in Fig. 2.2.

$$\begin{aligned} P_{IM} &= U_d I_d + U_q I_q, \\ Q_{IM} &= U_d I_q - U_q I_d \end{aligned} \quad (2.6)$$

2.2: Bayesian Estimation in Composite Load Parameter Identification

2.2.1: Gibbs sampling

Gibbs sampling is an extension of Monte Carlo Markov Chain method [111], which performs well when there are multiple parameters to identify. The detailed sampling algorithm is shown in Algorithm 1.

Algorithm 1 Gibbs Sampling

- 1: Draw initial samples $\boldsymbol{\theta}^{(0)} \sim q(\boldsymbol{\theta})$, where $q(\boldsymbol{\theta})$ is the prior.
 - 2: **for** iteration $i = 1, 2, \dots, M$ **do**
 - 3: Calculate $p(\theta_1 | \theta_2^{(i-1)}, \theta_3^{(i-1)}, \dots, \theta_n^{(i-1)})$ and sample $\theta_1^{(i)} \sim p(\theta_1 | \theta_2^{(i-1)}, \theta_3^{(i-1)}, \dots, \theta_n^{(i-1)})$
 - 4: Calculate $p(\theta_2 | \theta_1^{(i)}, \theta_3^{(i-1)}, \dots, \theta_n^{(i-1)})$ and sample $\theta_2^{(i)} \sim p(\theta_2 | \theta_1^{(i)}, \theta_3^{(i-1)}, \dots, \theta_n^{(i-1)})$
 - \vdots
 - 5: Calculate $p(\theta_n | \theta_1^{(i)}, \theta_3^{(i)}, \dots, \theta_{n-1}^{(i)})$ and sample $\theta_n^{(i)} \sim p(\theta_n | \theta_1^{(i)}, \theta_3^{(i)}, \dots, \theta_{n-1}^{(i)})$
 - 6: **end for**
 - 7: The distribution estimate is the histogram of $\boldsymbol{\theta}^i$, $i = m, \dots, M$, where m is the pre-defined burning in data set, which will be discarded.
-

Starting with priors, Gibbs sampling estimates the posterior of one parameter while fixing others' values as samples from previous estimated posteriors. This process repeats for all parameters in one iteration.

Here is a very simple example that shows how to update parameters in a linear model with coefficients β_0 and β_1 in one iteration: Suppose there are n observations of data pairs $(x_i, y_i, i = 1, \dots, n)$, where $y_i = \beta_0 + \beta_1 x_i + \epsilon$, $\epsilon \sim \mathcal{N}(0, 1/\tau)$. Therefore, the likelihood of this model is the product over n i.i.d. observations, which can be written as:

$$L(y_1, \dots, y_n, x_1, \dots, x_n | \beta_0, \beta_1, \tau) = \prod_{i=1}^n \mathcal{N}(\beta_0 + \beta_1 x_i, 1/\tau)$$

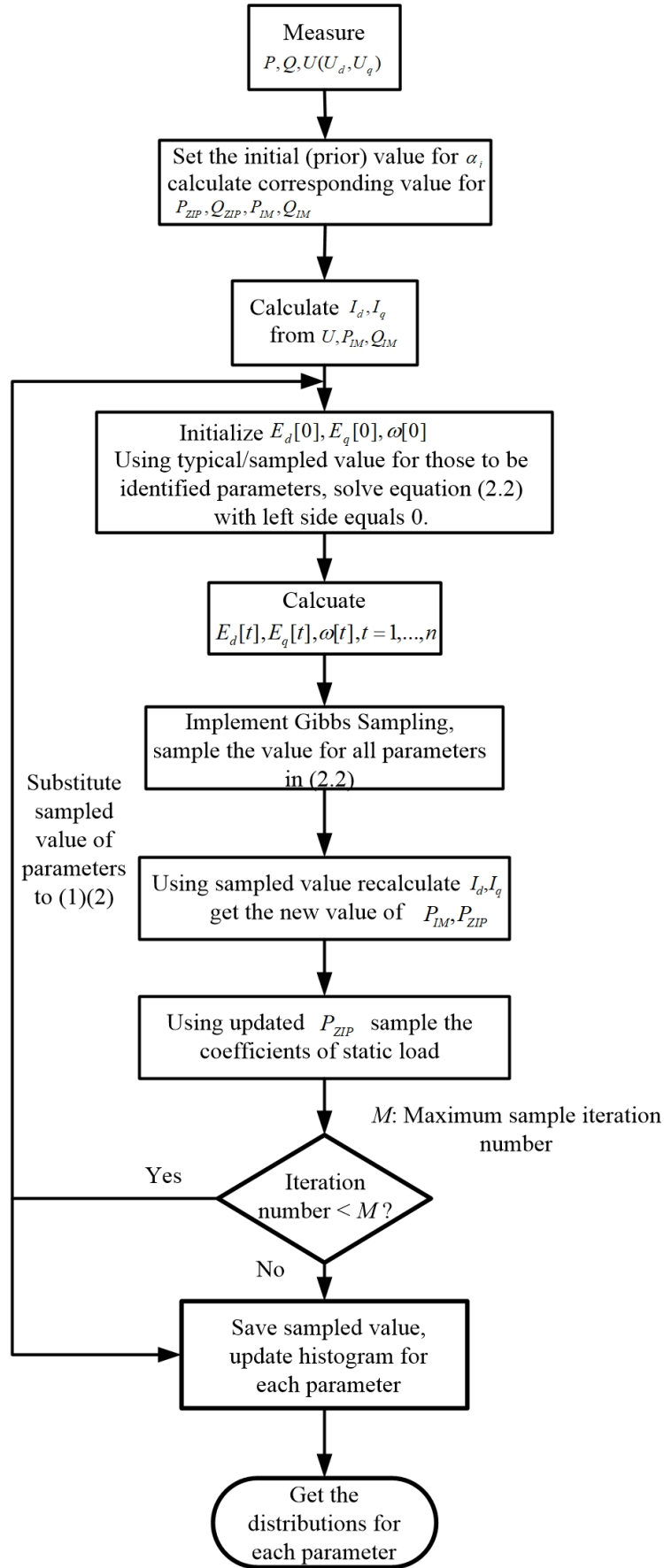


Figure 2.2: The flowchart of proposed algorithm.

The prior distributions of β_0 , β_1 are all normal distributions, which can be represented as $\beta_0 \sim \mathcal{N}(\mu_0, 1/\tau_0)$ and $\beta_1 \sim \mathcal{N}(\mu_1, 1/\tau_1)$, respectively. By using the GS method, β_0 will be updated first while β_1 is fixed. According to Baye's rule, it is of interest to find:

$$p(\beta_0|\beta_1, \tau, \mathbf{x}, \mathbf{y}) \propto p(\mathbf{x}, \mathbf{y}|\beta_0, \beta_1, \tau)p(\beta_0) \quad (2.7)$$

The log form of the right side of (2.7) yields:

$$-\frac{\tau_0}{2}(\beta_0 - \mu_0)^2 - \frac{\tau}{2} \sum_{i=1}^n (y_i - \beta_0 - \beta_1 x_i)^2 \quad (2.8)$$

Since the purpose is to find what the posterior distribution of β_0 is, all the terms in (2.8) not related to β_0 can be omitted, and yields:

$$\left(-\frac{\tau_0}{2} - \frac{\tau}{2}n\right)\beta_0^2 + (\tau_0\mu_0 + \tau \sum (y_i - \beta_1 x_i))\beta_0 \quad (2.9)$$

Recall that for a standard normal distribution that follows $\mathcal{N}(\mu, 1/\tau)$, the log-dependence on x is

$-\frac{\tau}{2}(x - \mu)^2 \propto -\frac{\tau}{2}x^2 + \tau\mu x$. Compared with 2.9, it is not difficult to find β_0 also follows normal distribution, and the updated distribution mean and variance are:

$$\beta_0|\beta_1, \tau, \tau_0, \mu_0, x, y \sim \mathcal{N}\left(\frac{\mu_0\tau_0 + \tau \sum (y_i - \beta_1 x_i)}{\tau_0 + \tau n}, \frac{1}{\tau_0 + \tau n}\right)$$

The updating of β_1 will follow the same procedure.

2.2.2: Gibbs in ZIP Model

The updating of each parameter in ZIP model can start with the prior guesses as follows:

$$\alpha_1 \sim \mathcal{N}(\mu_1^{(0)}, 1/\tau_1^{(0)}), \quad (2.10)$$

$$\alpha_2 \sim \mathcal{N}(\mu_2^{(0)}, 1/\tau_2^{(0)}), \quad (2.11)$$

$$\alpha_3 \sim \mathcal{N}(\mu_3^{(0)}, 1/\tau_3^{(0)}), \quad (2.12)$$

$$\tau \sim \mathcal{G}(a^{(0)}, b^{(0)}). \quad (2.13)$$

where the measurement noise $\epsilon \sim \mathcal{N}(0, 1/\tau)$, and the distribution of τ is a gamma distribution follows $\mathcal{G}(a, b)$. It can be shown that after each iteration of Gibbs sampling, the post distributions of these three parameters remain in the same form. Only the first iteration will be shown here as an example. First, samples are drawn from the prior and $\alpha_1^{(0)}, \alpha_2^{(0)}, \alpha_3^{(0)}, \tau^{(0)}$ are initialized. After some algebraic, yields:

$$p(\alpha_1 | \alpha_2^{(0)}, \alpha_3^{(0)}, \tau^{(0)}, \mathbf{x}, \mathbf{y}) \propto p(\mathbf{x}, \mathbf{y} | \alpha_1, \alpha_2^{(0)}, \alpha_3^{(0)}, \tau^{(0)}) p(\alpha_1) \quad (2.14)$$

where $p(\alpha_1 | \alpha_2^{(0)}, \alpha_3^{(0)}, \tau^{(0)}, \mathbf{x}, \mathbf{y})$ is the posterior probability given the samples of $\mathbf{x}, \mathbf{y}, \alpha_2$, and τ , $p(\mathbf{x}, \mathbf{y} | \alpha_1, \alpha_2^{(0)}, \tau^{(0)})$ is the probability in (2.3), and $p(\alpha_1)$ is the prior estimation following (2.10). Taking the log form on both sides of (2.14) yields

$$\begin{aligned} \log p(\alpha_1 | \alpha_2^{(0)}, \alpha_3^{(0)}, \tau^{(0)}, \mathbf{x}, \mathbf{y}) \propto \\ -\frac{\tau_1^{(0)}}{2} (\alpha_1 - \mu_1^{(0)})^2 - \\ \frac{\tau^{(0)}}{2} \sum_{t=1}^n (y[t] - (\alpha_1 x[t]^2 + \alpha_2^{(0)} x[t] + \alpha_3^{(0)}))^2 \end{aligned} \quad (2.15)$$

Taking log form helps convert the multiplications of the probabilities to summations, which can significantly simplify calculations when updating the distributions of the posteriors. For a normal distribution $y \sim \mathcal{N}(\mu, 1/\tau)$, the log dependence on y is $-\frac{\tau}{2}(y - \mu)^2 \propto -\frac{\tau}{2}y^2 + \tau\mu y$.

The right hand side of equation (2.15) can be further written as the following if the terms not related to α_1 are omitted.

$$\begin{aligned} -(\tau_1^{(0)} + \tau^{(0)} \sum_{t=1}^n x[t]^4) \alpha_1^2 / 2 + (\tau_1^{(0)} \mu_1^{(0)} \\ - \tau^{(0)} \sum_{t=1}^n (\alpha_3^{(0)} (y[t] - 1) x[t]^2 - \alpha_2^{(0)} x[t]^3)) \alpha_1 \end{aligned}$$

Define

$$\begin{aligned} \mu_1^{(1)} \triangleq \\ \frac{\tau_1^{(0)} \mu_1^{(0)} - \tau^{(0)} \sum_{t=1}^n ((\alpha_3^{(0)} (y[t] - 1) x[t]^2 - \alpha_2^{(0)} x[t]^3))}{\tau_1^{(0)} + \tau^{(0)} \sum_{t=1}^n x[t]^4}, \end{aligned}$$

$$\tau_1^{(1)} \triangleq \tau_1^{(0)} + \tau^{(0)} \sum_{t=1}^n x[t]^4,$$

yields

$$\alpha_1 | \alpha_2^{(0)}, \alpha_2^{(0)}, \tau^{(0)}, \tau_1^{(0)}, \mu_1^{(0)}, \mathbf{x}, \mathbf{y} \sim \mathcal{N}(\mu_1^{(1)}, 1/\tau_1^{(1)}).$$

Then sample a new α_1 from the estimated distribution $\mathcal{N}(\mu_1^{(1)}, \tau_1^{(1)})$ as $\alpha_1^{(1)}$. Following similar procedures, α_2 and α_3 can be derived. Define

$$\begin{aligned} \mu_2^{(1)} &\triangleq \\ &\frac{\tau_2^{(0)} \mu_2^{(0)} - \tau^{(0)} \sum_{t=1}^n ((\alpha_3^{(0)}(y[t] - 1)x[t] - \alpha_1^{(1)}x[t]^3))}{\tau_2^{(0)} + \tau^{(0)} \sum_{t=1}^n x[t]^2}, \\ \tau_2^{(1)} &\triangleq \tau_2^{(0)} + \tau^{(0)} \sum_{i=1}^n x[t]^2. \end{aligned}$$

Therefore, the following can be derived:

$$\alpha_2 | \alpha_1^{(1)}, \alpha_2^{(0)}, \tau^{(0)}, \tau_2^{(0)}, \mu_2^{(0)}, \mathbf{x}, \mathbf{y} \sim \mathcal{N}(\mu_2^{(1)}, 1/\tau_2^{(1)}).$$

Define

$$\begin{aligned} \mu_3^{(1)} &\triangleq \\ &\frac{\tau_3^{(0)} \mu_3^{(0)} - \tau^{(0)} \sum_{t=1}^n (y[t] - \alpha_1^{(1)}x[t]^2 - \alpha_2^{(1)}x[t])}{\tau_3^{(0)} + \tau^{(0)}n}, \\ \tau_3^{(1)} &\triangleq \tau_3^{(0)} + \tau^{(0)}n. \end{aligned}$$

Therefore, the following can be derived:

$$\alpha_3 | \alpha_1^{(1)}, \alpha_2^{(1)}, \tau^{(0)}, \tau_3^{(0)}, \mu_3^{(0)}, \mathbf{x}, \mathbf{y} \sim \mathcal{N}(\mu_3^{(1)}, 1/\tau_3^{(1)}).$$

For τ , the posterior given new samples of $\alpha_1^{(1)}$ and $\alpha_2^{(1)}$ can be written as

$p(\tau | \alpha_1^{(1)}, \alpha_2^{(1)}, \mathbf{x}, \mathbf{y}) \propto p(\mathbf{x}, \mathbf{y} | \alpha_1^{(1)}, \alpha_2^{(1)}, \tau) p(\tau)$. Taking the log form of both sides of the posterior yields

$$\begin{aligned} \log p(\tau | \alpha_1^{(1)}, \alpha_2^{(1)}, \mathbf{x}, \mathbf{y}) &\propto \\ &\frac{n}{2} \log \tau - \frac{\tau}{2} \sum_{t=1}^n (y[t] - \alpha_1^{(1)}x[t]^2 - \alpha_2^{(1)}x[t] - \\ &\alpha_3^{(1)} + (a^{(0)} - 1) \log \tau - b^{(0)}\tau). \end{aligned}$$

Define

$$\begin{aligned} a^{(1)} &= a^{(0)} + n/2, \\ b^{(1)} &= b^{(0)} + \\ &\sum_{t=1}^n (y[t] - \alpha_1^{(1)}x[t]^2 - \alpha_2^{(1)}x[t] - \alpha_3^{(1)})^2/2. \end{aligned}$$

and the posterior $\tau|\alpha_1^{(1)}, \alpha_2^{(1)}, \mathbf{x}, \mathbf{y} \sim \mathcal{G}(a^{(1)}, b^{(1)})$ can be obtained.

2.2.3: Gibbs in IM models

GS in the IM model will follow the same steps as that in the ZIP model. Start with the priors as follows.

$$\begin{aligned} \beta_1 &\sim \mathcal{N}(\mu_{\beta_1}^{(0)}, 1/\tau_{\beta_1}^{(0)}), \beta_2 \sim \mathcal{N}(\mu_{\beta_2}^{(0)}, 1/\tau_{\beta_2}^{(0)}) \\ \beta_3 &\sim \mathcal{N}(\mu_{\beta_3}^{(0)}, 1/\tau_{\beta_3}^{(0)}), \alpha_b \sim \mathcal{N}(\mu_{\alpha_b}^{(0)}, 1/\tau_{\alpha_b}^{(0)}) \\ \alpha_c &\sim \mathcal{N}(\mu_{\alpha_c}^{(0)}, 1/\tau_{\alpha_c}^{(0)}), \tau_E \sim \mathcal{G}(\alpha_E^{(0)}, \beta_E^{(0)}) \\ \tau_\omega &\sim \mathcal{G}(\alpha_\omega^{(0)}, \beta_\omega^{(0)}), \tau_I \sim \mathcal{G}(\alpha_I^{(0)}, \beta_I^{(0)}). \end{aligned}$$

Given the measurement of $y_{E_d}, y_{E_q}, y_\omega, E'_q, E'_d, I_d, I_q, U_d, U_q$, Gibbs sampling of the IM model is stated as follows.

Define

$$\begin{aligned} \mu_{\beta_1}^{(k+1)} &= \frac{\tau_{\beta_1}^{(k)}\mu_{\beta_1}^{(k)} + \tau_E^{(k)} \sum_{t=1}^n (E'_d[t]y_{E_d}[t] + E'_q[t]y_{E_q}[t] - \beta_2^{(k)}(E'_d[t]I_q[t] - E'_q[t]I_d[t]))}{\tau_{\beta_1}^{(k)} + \tau_E^{(k)} \sum_{t=1}^n (E'_d[t]^2 + E'_q[t]^2)}, \\ \tau_{\beta_1}^{(k+1)} &= \frac{1}{\tau_{\beta_1}^{(k)} + \tau_E^{(k)} \sum_{t=1}^n (E'_d[t]^2 + E'_q[t]^2)}, \\ \Rightarrow \beta_1 | \beta_2^{(k)}, y_{E_d}, y_{E_q}, E'_d, E'_q, U_d, U_q, I_q, I_d, \omega, \tau_E^{(k)}, \tau_{\beta_1}^{(k)}, \mu_{\beta_1}^{(k)} &\sim \mathcal{N}(\mu_{\beta_1}^{(k+1)}, \tau_{\beta_1}^{(k+1)}) \end{aligned}$$

Define

$$\begin{aligned}\mu_{\beta_2}^{(k+1)} &= \frac{\tau_{\beta_2}^{(k)} \mu_{\beta_2}^{(k)} + \tau_E^{(k)} \sum_{t=1}^n \left(y_{E_d}[t] I_q[t] - y_{E_q}[t] I_d[t] + \beta_1^{(k+1)} (E'_d[t] I_q[t] - E'_q[t] I_d[t]) + (\omega[t]-1) (E'_d[t] I_d[t] + E_q[t] I_q[t]) \right)}{\tau_{\beta_2}^{(k)} + \tau_E^{(k)} \sum_{t=1}^n (I_d[t]^2 + I_q[t]^2)}, \\ \tau_{\beta_2}^{(k+1)} &= \frac{1}{\tau_{\beta_2}^{(k)} + \tau_E^{(k)} \sum_{t=1}^n (I_d[t]^2 + I_q[t]^2)}, \\ \Rightarrow \beta_2 | \beta_1^{(k+1)}, y_{E_d}, y_{E_q}, E'_d, E'_q, U_d, U_q, I_d, I_q, \omega, \tau_E^{(k)}, \tau_{\beta_2}^{(k)}, \mu_{\beta_2}^{(k)} &\sim \mathcal{N}(\mu_{\beta_2}^{(k+1)}, \tau_{\beta_2}^{(k+1)})\end{aligned}$$

Define

$$\begin{aligned}\mu_{\beta_3}^{(k+1)} &= \frac{\tau_{\beta_3}^{(k)} \mu_{\beta_3}^{(k)} - \tau_\omega^{(k)} \sum_{t=1}^n \left(y_\omega[t] (-\omega[t]^2 T_0 + E'_d[t] I_d[t] + E_q[t] I_q[t]) \right)}{\tau_{\beta_3}^{(k)} + \tau_\omega^{(k)} \sum_{t=1}^n \left(\omega[t]^4 T_0^2 + (E'_d[t] I_d[t] + E_q[t] I_q[t])^2 - 2\omega[t]^2 T_0 (E'_d[t] I_d[t] + E_q[t] I_q[t]) \right)}, \\ \tau_{\beta_3}^{(k+1)} &= \frac{1}{\tau_{\beta_3}^{(k)} + \tau_\omega^{(k)} \sum_{t=1}^n \left(\omega[t]^4 T_0^2 + (E'_d[t] I_d[t] + E_q[t] I_q[t])^2 - 2\omega[t]^2 T_0 (E'_d[t] I_d[t] + E_q[t] I_q[t]) \right)}, \\ \Rightarrow \beta_3 | E'_d, E'_q, U_d, U_q, I_d, I_q, y_\omega, \omega, \tau_E^{(k)}, \tau_{\beta_3}^{(k)}, \mu_{\beta_3}^{(k)} &\sim \mathcal{N}(\mu_{\beta_3}^{(k+1)}, \tau_{\beta_3}^{(k+1)})\end{aligned}$$

Define

$$\begin{aligned}\mu_{\alpha_b}^{(k+1)} &= \frac{\tau_{\alpha_b}^{(k)} \mu_{\alpha_b}^{(k)} + \tau_I^{(k)} \sum_{t=1}^n \left(I_d[t] (U_d[t] - E'_d[t]) + I_q[t] (U_q[t] - E'_q[t]) \right)}{\tau_{\alpha_b}^{(k)} + \tau_I^{(k)} \sum_{t=1}^n \left((U_d[t] - E_d[t])^2 + (U_q[t] - E_q[t])^2 \right)}, \\ \tau_{\alpha_b}^{(k+1)} &= \frac{1}{\tau_{\alpha_b}^{(k)} + \tau_I^{(k)} \sum_{t=1}^n \left((U_d[t] - E_d[t])^2 + (U_q[t] - E_q[t])^2 \right)}, \\ \Rightarrow \alpha_b | E'_d, E'_q, U_d, U_q, I_d, I_q, \tau_I^{(k)}, \tau_{\alpha_b}^{(k)}, \mu_{\alpha_b}^{(k)} &\sim \mathcal{N}(\mu_{\alpha_b}^{(k+1)}, \tau_{\alpha_b}^{(k+1)})\end{aligned}$$

Define

$$\begin{aligned}\mu_{\alpha_c}^{(k+1)} &= \frac{\tau_{\alpha_c}^{(k)} \mu_{\alpha_c}^{(k)} + \tau_I^{(k)} \sum_{t=1}^n \left(I_d[t] (U_d[t] - E'_d[t]) - I_q[t] (U_q[t] - E'_q[t]) \right)}{\tau_{\alpha_c}^{(k)} + \tau_I^{(k)} \sum_{t=1}^n \left((U_d[t] - E_d[t])^2 + (U_q[t] - E_q[t])^2 \right)}, \\ \tau_{\alpha_c}^{(k+1)} &= \frac{1}{\tau_{\alpha_c}^{(k)} + \tau_I^{(k)} \sum_{t=1}^n \left((U_d[t] - E_d[t])^2 + (U_q[t] - E_q[t])^2 \right)}, \\ \Rightarrow \alpha_c | E'_d, E'_q, U_d, U_q, I_d, I_q, \tau_I^{(k)}, \tau_{\alpha_c}^{(k)}, \mu_{\alpha_c}^{(k)} &\sim \mathcal{N}(\mu_{\alpha_c}^{(k+1)}, \tau_{\alpha_c}^{(k+1)})\end{aligned}$$

Define

$$\begin{aligned}\alpha_E^{(k+1)} &= \alpha_E^{(k)} + n/2, \\ \beta_E^{(k+1)} &= \beta_E^{(k)} + \\ &\frac{\sum_{t=1}^n \left[\left(y_{E_d}[t] - \beta_1^{(k+1)} E'_q[t] - \beta_2^{(k+1)} I_d[t] + (\omega[t]-1) E'_q[t] \right)^2 + \left(y_{E_q}[t] - \beta_1^{(k+1)} E'_d[t] + \beta_2^{(k+1)} I_q[t] - (\omega[t]-1) E'_d[t] \right)^2 \right]}{2}, \\ \Rightarrow \tau_E^{(k+1)} | I_d, I_q, y_{E_d}, y_{E_q}, E'_d, E'_q, \omega, \beta_1^{(k+1)}, \beta_2^{(k+1)} &\sim \mathcal{G}(\alpha_E^{(k+1)}, \beta_E^{(k+1)})\end{aligned}$$

Define

$$\begin{aligned}\alpha_\omega^{(k+1)} &= \alpha_\omega^{(k)} + n/2, \\ \beta_\omega^{(k+1)} &= \beta_\omega^{(k)} + \frac{1}{2} \sum_{t=1}^n [y_\omega[t] - \beta_3^{(k+1)}(\omega[t]^2 T_0 - E'_d[t]I_d[t] - E'_q[t]I_q[t])]^2, \\ \Rightarrow \tau_\omega^{(k+1)} | I_d, I_q, E'_d, E'_q, y_\omega, \omega, U_d, U_q, \beta_3^{(k+1)} &\sim \mathcal{G}(\alpha_\omega^{(k+1)}, \beta_\omega^{(k+1)})\end{aligned}$$

Define

$$\begin{aligned}\alpha_I^{(k+1)} &= \alpha_I^{(k)} + n/2, \\ \beta_I^{(k+1)} &= \beta_I^{(k)} + \\ &\frac{\sum_{t=1}^n \left[\left(I_d[t] - \alpha_b^{(k+1)}(U_d[t] - E'_d[t]) - \alpha_c^{(k+1)}(U_q[t] - E'_q[t]) \right)^2 + \left(I_q[t] - \alpha_b^{(k+1)}(U_q[t] - E'_q[t]) + \alpha_c^{(k+1)}(U_d[t] - E'_d[t]) \right)^2 \right]}{2}, \\ \Rightarrow \tau_I^{(k+1)} | E'_d, E'_q, U_d, U_q, I_d, I_q, \alpha_b^{(k+1)}, \alpha_c^{(k+1)} &\sim \mathcal{G}(\alpha_I^{(k+1)}, \beta_I^{(k+1)})\end{aligned}$$

2.3: Case Study

Simulation studies have been carried out in this section for the composite models with ZIP+IM considering measurement errors and outliers. Benchmark test using least square and genetic algorithm methods are also proposed. Only active power is shown as an example, the reactive power will follow the same steps. In GS, the length m of the burn-in process is chosen as 5000 [111].

2.3.1: Composite Model Parameters Identification

The 33-bus test feeder [15], as shown in Fig. 3.19, is simulated to generate the testing data. A detailed description of the test system can be found in [29]. The load at bus 17 is connected with a ZIP+IM load as an example. The ZIP factors of the load at node 17 were assigned as $\alpha_1 = 0.25$, $\alpha_2 = 0.25$, $\alpha_3 = 0.5$ with $\lambda_p = 0.5$. Therefore, the expected value of each parameters are all scaled by λ_p . By implementing the proposed GS method, the estimation of coefficients for the ZIP model and IM model are estimated as shown in Fig. 2.4 . The discrete distributions for each parameter can be derived by implementing

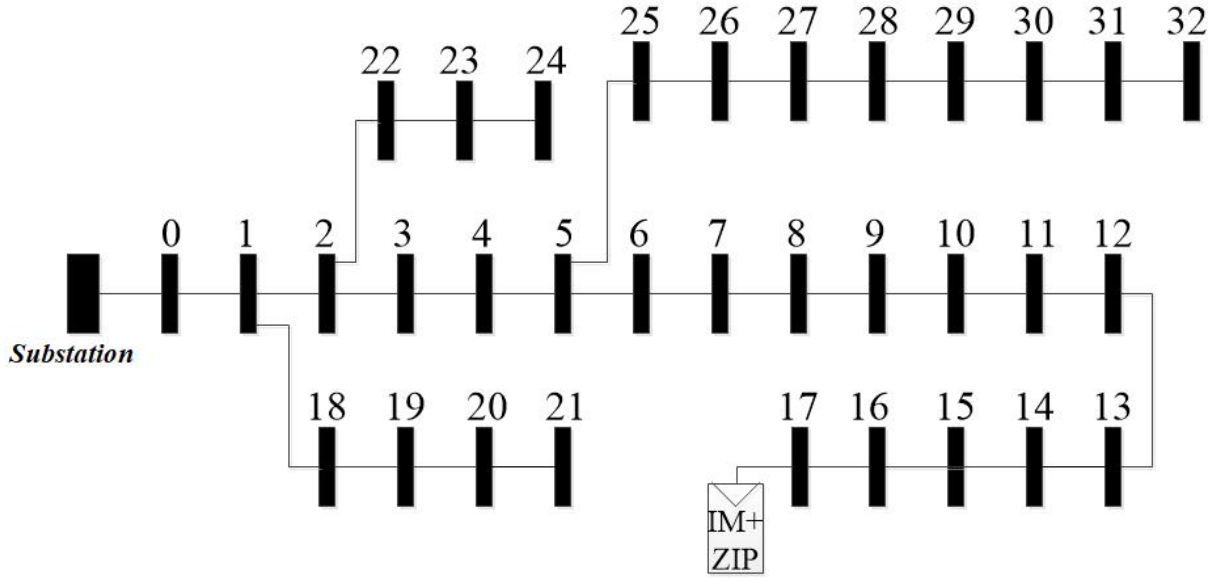


Figure 2.3: The 33bus test system for synthetic data.

the proposed method. The identified distributions describe the probabilities of different values falling into different ranges. In this study, the mean value is selected as the estimated value of each parameter, and is listed in Table 2.1. The estimation error of each parameter compared with the real value is also included in Table 2.1. According to Table 2.1, the estimation errors are less than 6% with 0 measurement error. In most cases, the errors are even smaller than 6%. The active power response by using the identified parameters is shown in Fig. 2.5. Comparing with the true active response, only tiny differences are observed. It is worth mentioning that the estimation of parameters highly relies on the prior distributions. A good prior can significantly increase the estimation accuracy and shorten the burn-in period [112].

As it was mentioned in Chapter 1, the GS method is able to handle certain measurement errors and anomalies. In Table 2.2, the estimated values are presented by considering 10% measurement error and measurement anomalies by using the proposed method. The measurement anomalies is simulated by replacing the results of 2500 random measurements by 0 (both active power and voltage) among total 250,000 readings,

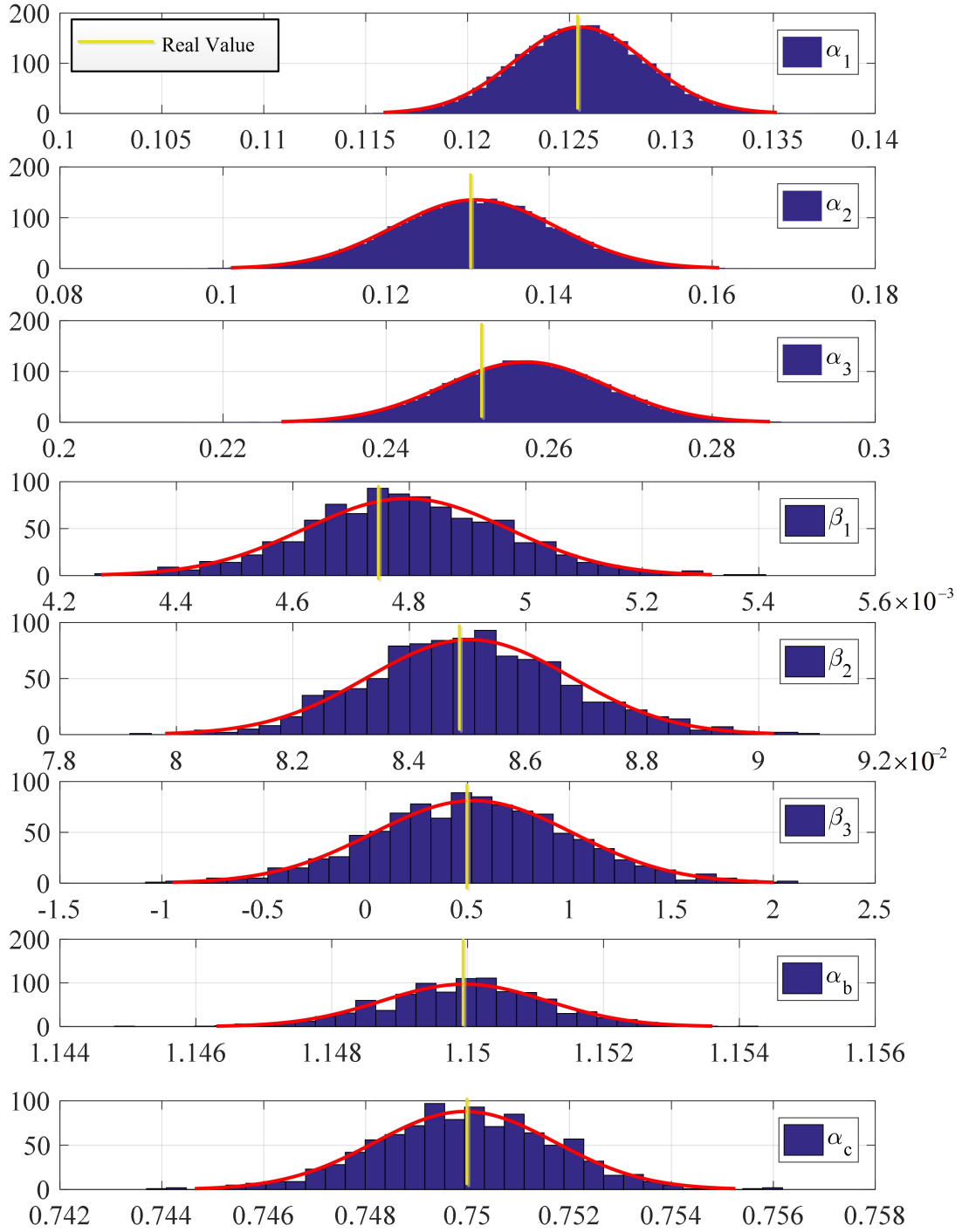


Figure 2.4: The estimated parameters of the ZIP model.

which can be considered as 1% measurement anomaly. The results shown in Table 2.2 indicate the identifications are influenced by the errors and anomalies, but the accuracy is still within an acceptable range.

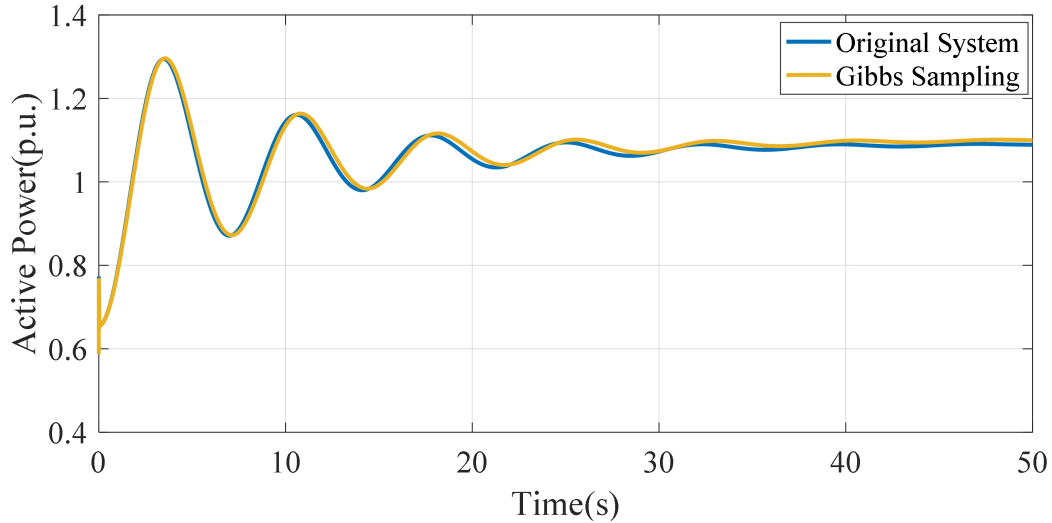


Figure 2.5: Comparison of system active response between the original system and the estimated system.

2.3.2: Benchmarks & Comparison

The ZIP and IM model parameters derived by the proposed GS method are compared by using least square (LS) [28] and Genetic Algorithm (GA) methods [16]. The "lsqcurvefit" and "ga" function in Matlab was used to derive the coefficients in LS and GA, respectively. Parameters identified by the three different approaches are listed in Table 2.3. Comparisons of the active power responses using the parameters identified by LS, and GA techniques are presented in Fig 2.6 as well. According to Figs 2.2 and 2.6, it is obvious that the GS approach has the best performance, while the GA and LS methods produce larger error than the GS method. The scenarios with measurement errors and anomalies are also considered in LS and GA approaches. The same measurement error and anomaly are used, and the comparisons are shown in Tables 2.4 and 2.5, respectively. The system responses using the aforementioned parameters by the GS, LS, GA approaches with 10% measurement error and 1% measurement anomaly are shown in Figs. 2.9 and 2.8, respectively. It can be shown that under the same circumstance,

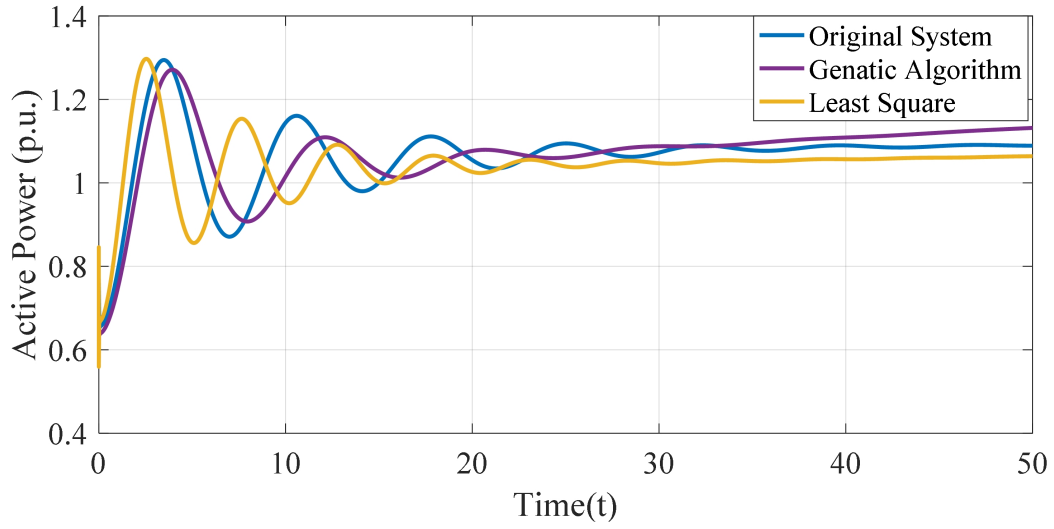


Figure 2.6: The active power response comparison by using LS and GA.

Table 2.1: Estimated and Real Value of the Parameters for ZIP+IM Model with 0 Measurement error.

Para.	Real Value	Est. Value (mean)	Error(%)
α_1	0.125	0.1248	0.16
α_2	0.125	0.128	6.7
α_3	0.25	0.256	2.4
β_1	0.0048	0.00475	1.04
β_2	0.0085	0.0083	2.33
β_3	0.5	0.497	0.6
α_b	1.15	1.152	0.13
α_c	0.75	0.757	0.93

Table 2.2: Estimated and Real Value of the Parameters for ZIP+IM Model with 10% Measurement Errors and Anomalies. (The value in the parenthesis is the estimation error in percentage.)

Para.	Est. Value with 10% Meas. Error	Est. Value with Anomalies	True Value
α_1	0.1264(1.12)	0.1267(1.36)	0.125
α_2	0.1276(2.08)	0.1268(1.44)	0.125
α_3	0.254(1.60)	0.2561(2.44)	0.25
β_1	0.0048(0.00)	0.0046(4.20)	0.0048
β_2	0.0081(4.71)	0.00832(2.12)	0.0085
β_3	0.52(4.00)	0.46(8.00)	0.5
α_b	1.3(13.04)	1.24(7.82)	1.15
α_c	0.78(4.00)	0.734(2.13)	0.75

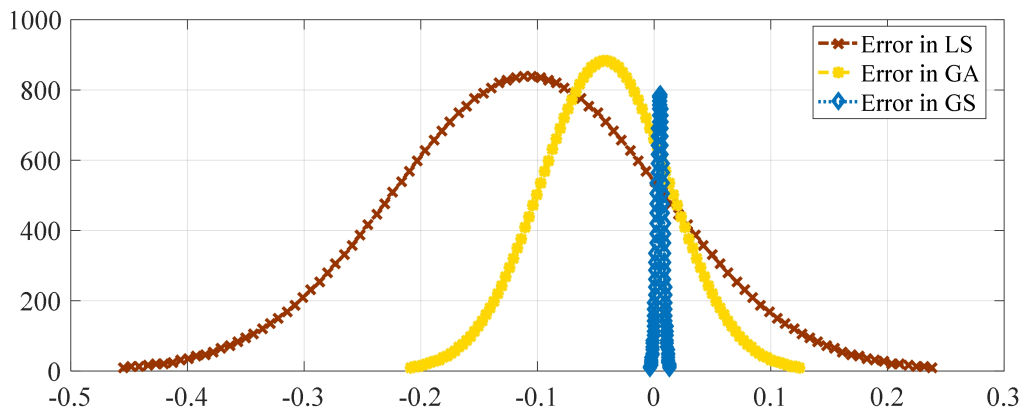


Figure 2.7: Error of active power using GS, GA, LS with 10% measurement error.

Table 2.3: Composite Model Parameter Estimations without Measurement Error by Different Methods. (The value in the parenthesis is the estimation error in percentage.)

Para.	GS	LS	GA
α_1	0.1248(0.16)	0.15(20)	0.16(28)
α_2	0.128(2.4)	0.137(8)	0.104(16.8)
α_3	0.256(2.4)	0.284(11.97)	0.39(39)
β_1	0.00475(1.04)	0.007(45.8)	0.0072(50)
β_2	0.0083(2.3)	0.0092(8.2)	0.0102(20)
β_3	0.497(0.6)	0.4(20)	0.411(17.8)
α_b	1.152(0.17)	0.99(14.08)	0.87(24.3)
α_c	0.757(1.03)	0.227(69)	0.204(72.8)

Table 2.4: Composite Model Parameter Estimation with Different Methods Considering 10% Measurement Errors. (The value in the parenthesis is the estimation error in percentage.)

Para.	GS	LS	GA
α_1	0.1264(1.12)	0.105(16)	0.184(47.2)
α_2	0.1276(2.08)	0.123(1.6)	0.114(8.8)
α_3	0.254(1.60)	0.194(22.4)	0.284(13.6)
β_1	0.0048(0.00)	0.0047(2.08)	0.0052(8.3)
β_2	0.0081(4.71)	0.00154(4.7)	0.008(1.18)
β_3	0.52(4.00)	0.4009(20)	0.45(10)
α_b	1.3(13.04)	0.9975(13.2)	1.043(9.3)
α_c	0.78(4.00)	0.2043(71.5)	0.442(41.67)

Table 2.5: Composite Model Parameter Estimations with Different Methods Considering Anomalies. (The value in the parenthesis is the estimation error in percentage.)

Para.	GS	LS	GA
α_1	0.1267(1.36)	0.122(2.4)	0.199(59.2)
α_2	0.1268(1.44)	0.117(6.4)	0.107(14.4)
α_3	0.2561(2.44)	0.228(8.8)	0.297(18.8)
β_1	0.0046(4.20)	0.0043(10.4)	0.004(16.7)
β_2	0.00832(2.12)	0.0084(1.17)	0.006(29.4)
β_3	0.46(8.00)	0.403(19.4)	0.408(19.2)
α_b	1.24(7.82)	0.815(29.1)	1.05(8.7)
α_c	0.734(2.13)	0.65(13.3)	0.803(7.07)

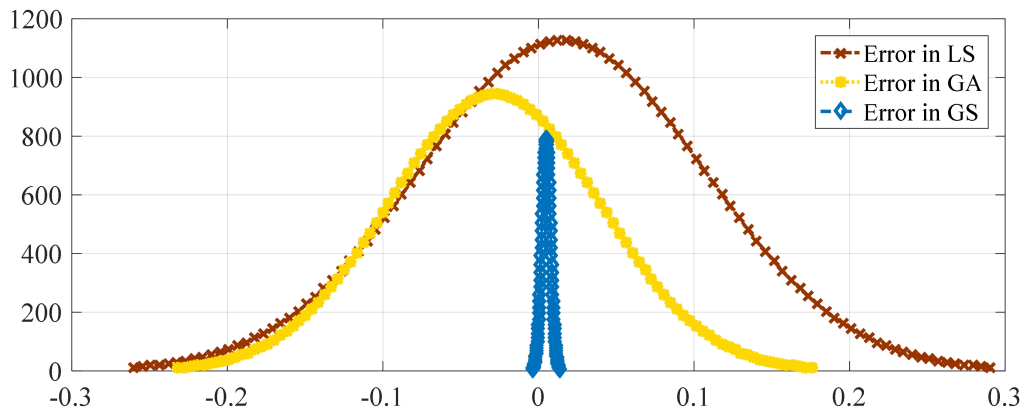


Figure 2.8: Error of active power using GS, GA, LS with measurement anomalies.

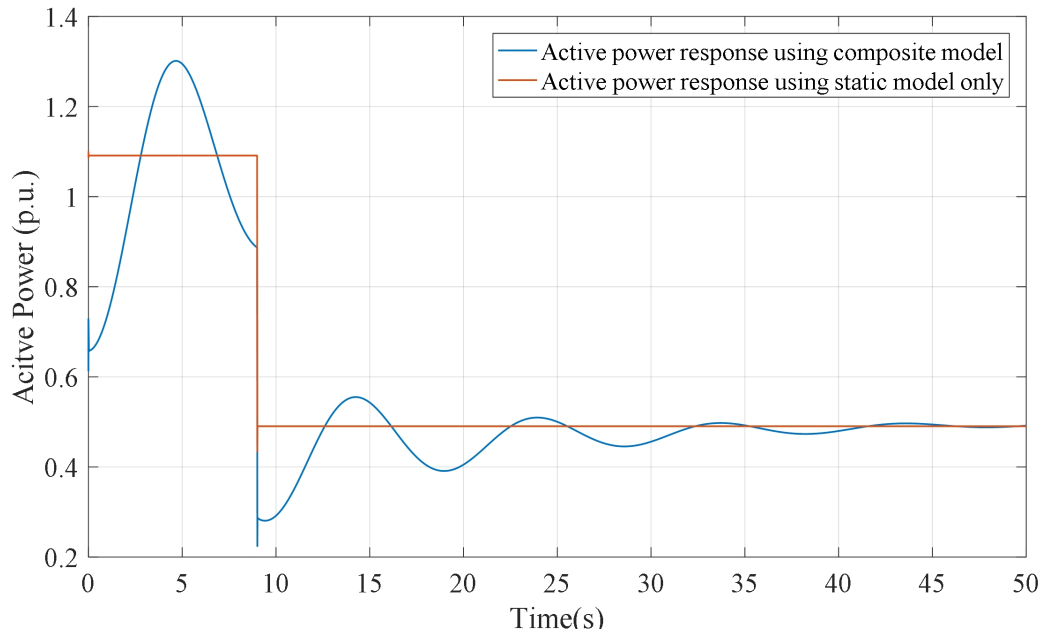


Figure 2.9: The active power response at the same bus using composite and static load models.

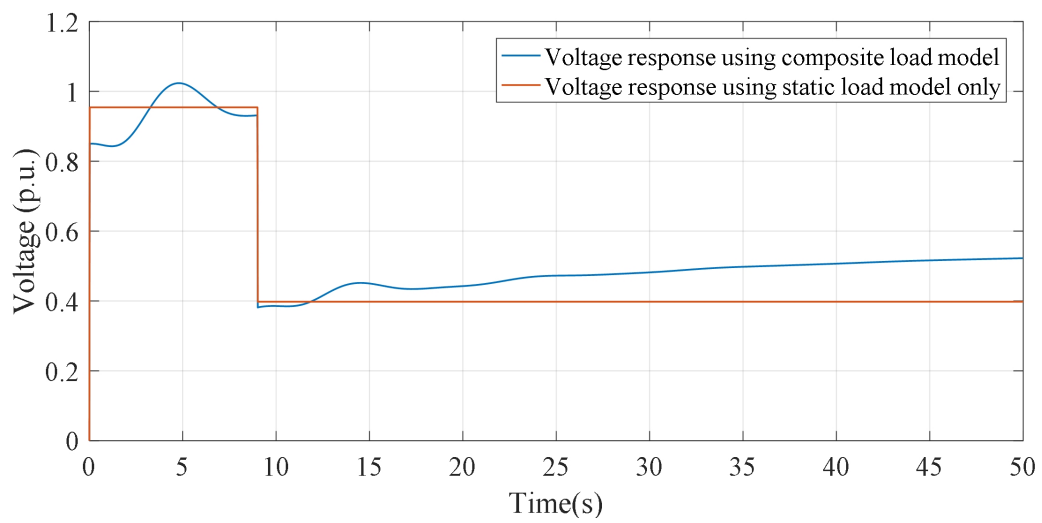


Figure 2.10: The voltage response at the same bus using composite and static load models.

the GS method is able to provide the best estimation, while the LS and GA methods are significantly impacted by measurement errors and anomalies.

The comparisons of the active power and voltage responses in the same system when there is a fault happened at bus 17 by using different load models in the Simulink are shown in Figs. 2.9 and 2.10, respectively. The system response using the composite load models can clearly represent the dynamic behaviors of the system, while by using the built-in load model in the Simulink, only the static part of the responses can be presented. Therefore, it is important to use an accurate model when doing studies such as stability analysis, reliability analysis, as well as other related dynamic analyses.

CHAPTER 3: PV ACTIVE POWER CONTROL WITH COMMUNICATION DELAYS

3.1: Model of a grid-tied PV system with power control capability

In this chapter, the model of a grid-tied PV system with real power control capability will be proposed, following with the control design of such model with communication delays been considered.

The schematic diagram of a grid-tied PV system with real power control capability for voltage regulation is shown in Fig. 3.1. The system has three major parts: the plant model, the inverter controller and the grid voltage controller. The plant model is the main power circuit of the system. There is no DC/DC converter in the circuit and the DC/AC inverter is used to not only convert DC power into AC, but also achieve real power control via the inverter controller. The inverter controller regulates the PV output current (i_{pv}) to follow the PV current reference ($i_{pv.ref}$) by generating a dc bus voltage reference ($V_{dc.ref}$). Since there is no DC/DC converter, the dc bus voltage V_{dc} is also the PV output voltage. The dc bus voltage error signal ($V_{dc} - V_{dc.ref}$) is then used to regulate the inverter output real power represented by the d-axis current i_d . The inverter controller can also achieve maximum power point tracking (MPPT), which is shown in Fig. 3.1, by regulating the dc bus voltage (V_{dc}). The grid voltage controller takes the grid voltage control error ($V_{ref} - V$) as input and generates the reference current ($i_{pv.ref}$) for controlling the inverter. For the purpose of analysis, four PI controllers (represented by PI_i in Fig. 3.1) are used in this model though some other types of controller can be used as well. PI_1 is used to produce the reference dc voltage of the PV panel $V_{dc.ref}$ from ($i_{pv} - i_{pv.ref}$). PI_2 and PI_3 are traditional controllers usually used in the DC/AC inverter control. PI_4 generates the reference current $i_{pv.ref}$ of the PV panel from ($V_{ref} - V$). The

state variables of the system are chosen as follows:

- x_1 : the integrator output of PI_1
- x_2 : the integrator output of PI_2
- x_3 : the first order response of $i_{d.ref}$
- x_4 : the integrator output of PI_3
- x_5 : the d-axis component of the output current i_d
- x_6 : the input current of the inverter $i_{dc.inv}$
- x_7 : the voltage of the dc side of the inverter V_{dc} , $V_{dc} = V_{pv}$
- x_8 : the integrator output of PI_4

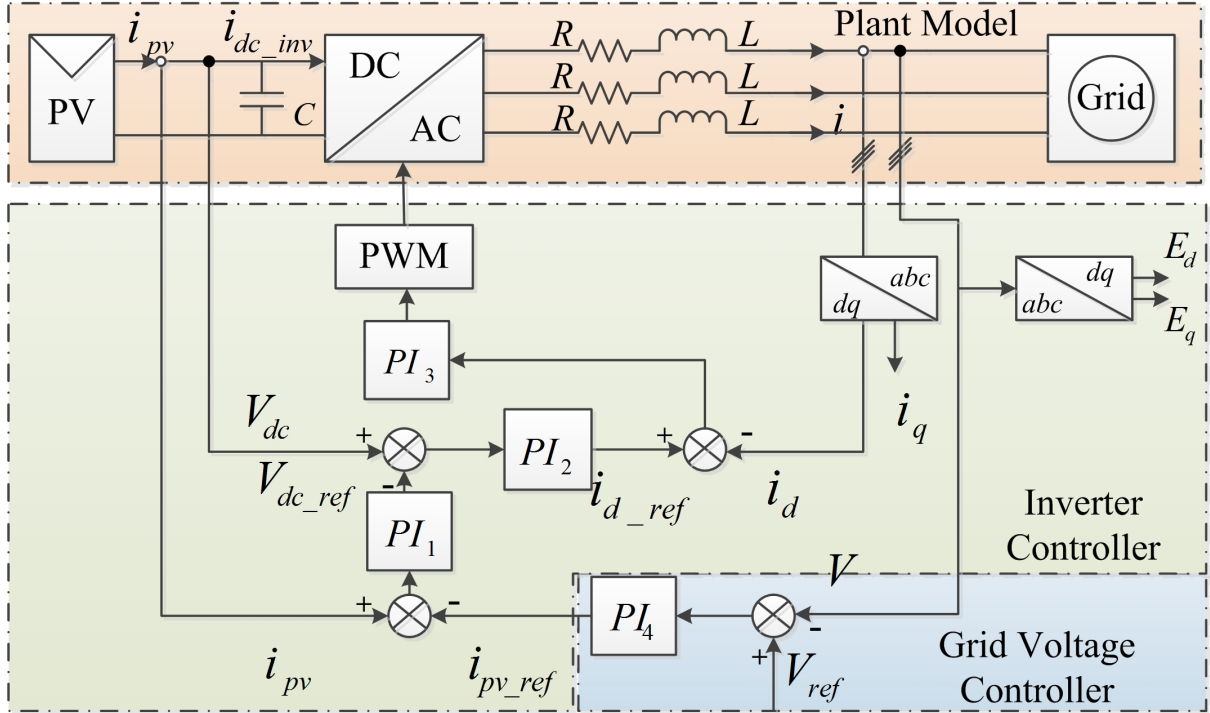


Figure 3.1: Schematic diagram of a grid-connected PV system.

The detailed dynamic model of the PV system is shown in Fig. 3.2. For analysis, the system is a linearized model. It should be noted that the model is for the j th PV system. The subscript j is omitted for the cases where the omission will not cause confusion. In the figure, the four PI controllers are represented by $(K_{Pc} + K_{Ic}/s)$, $c = 1, \dots, 4$. T_2 is a

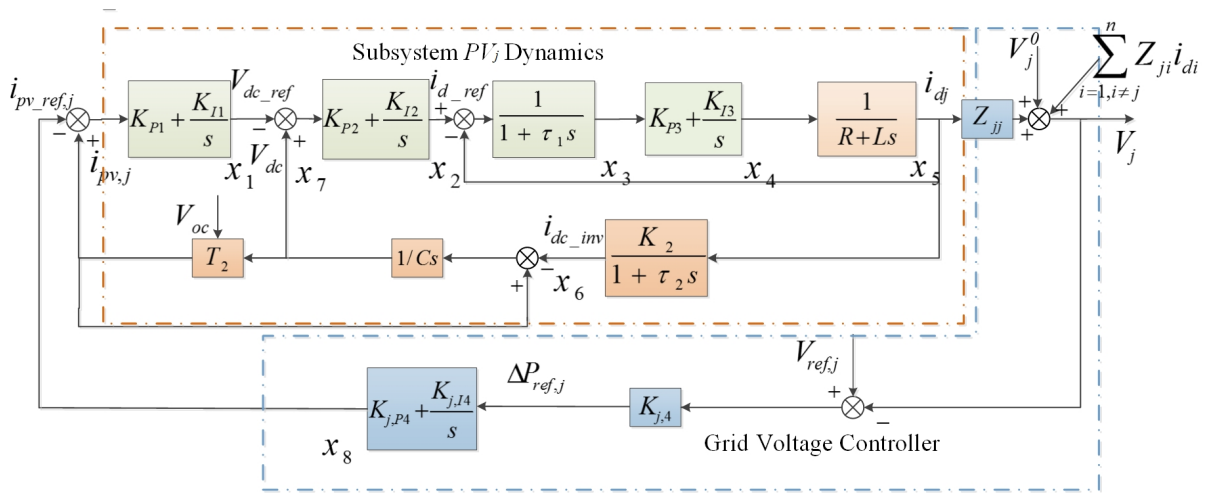


Figure 3.2: Detailed model of the grid-connected PV system at bus j .

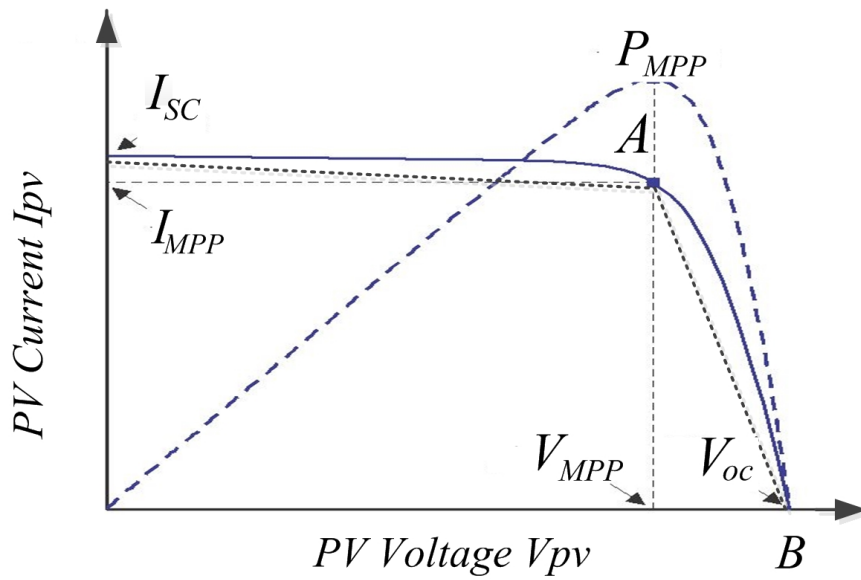


Figure 3.3: PV I-V curve and the linearization of R_{pv} .

linearized model for describing the $V - I$ characteristic of the PV panel. The PV system normally works between V_{MPP} and V_{oc} , as shown in Fig. 3.3. V_{oc} is the open circuit voltage of the PV panel and V_{MPP} is the voltage at the maximum power point. V_{oc} is a function of solar irradiance, temperature, the material of the panel, the number of PVs connected in series, etc. For a fixed PV panel, if the solar irradiance and the temperature are constant, then V_{oc} is also a constant. The $V - I$ relationship of the PV panel can be represented as:

$$i_{pv} = (V_{oc} - V_{pv})/R_{pv} \quad (3.1)$$

where $V_{pv} = V_{dc}$. R_{pv} is the equivalent resistance of the panel and changes with PV voltages. For the purpose of simplification without introducing a large error, a linearized equivalent resistance R_{pv} is used in this model. In other words, a straight line AB is considered in calculating R_{pv} , shown in Figs. 3.2 and 3.3.

$$R_{pv} = \frac{V_{oc} - V_{MPP}}{I_{MPP}} \quad (3.2)$$

where I_{MPP} is the corresponding PV current when the PV works at its maximum power point.

The dc input current to the inverter is determined by the inverter output current, and ultimately by the inverter output power. The relationship between the input and output currents of the inverter is modeled by a first order system in this study.

$$i_{dc-inv} = i_d \frac{K_2}{1 + \tau_2 s} \quad (3.3)$$

where i_d is the d-axis component of the inverter output current, i_{dc-inv} is the dc input current of the inverter, and τ_2 is the time constant of the first order system. K_2 is a constant, which can be calculated based on power balancing between the input and

output powers of the inverter. Assuming there is no power loss in the inverter and the d-axis is aligned with phase A, the following power balance equation can be established when there is no reactive power (i.e., $i_q = 0$, $E_q = 0$):

$$V = \sqrt{E_d^2 + E_q^2} = E_d$$

$$V_{dc} \cdot i_{dc_inv} = \frac{3}{2} E_d i_d \implies V_{dc_ref} \cdot i_{dc_inv} = \frac{3}{2} E_d i_d \quad (3.4)$$

where E_d is the d-axis component of the grid voltage, and E_q is the q-axis component of the grid voltage.

In this case, K_2 can be obtained as:

$$K_2 = \frac{3E_d}{2V_{dc_ref}} \quad (3.5)$$

The block of $f(\mathbf{i}_d)$, $\mathbf{i}_d = [i_{d1}, \dots, i_{dn}]^T$, in Fig. 3.2 is used to represent the power network algebraic equations that link the injected currents and the system bus voltages. The system bus voltages (\mathbf{V}_{bus}) can be obtained based on the system impedance matrix (\mathbf{Z}_{bus}) and the injected current sources (\mathbf{I}_{bus}) as [96]:

$$\mathbf{V}_{bus} = \mathbf{Z}_{bus} \mathbf{I}_{bus} \quad (3.6)$$

For instance, the voltage of bus j in the power network can be obtained as:

$$V_j = Z_{jj} i_{dj} + \sum_{i=1, i \neq j}^n Z_{ij} i_{di} + V_j^0 \quad (3.7)$$

where i_{di} ($i = 1, \dots, n$) are the injected currents from the *PV* sources and n is the total number of *PVs* in the distribution grid. V_j^0 is the voltage contribution to bus j from other generation sources and loads, which is a constant in this study.

$K_{j,4}$ is a constant coefficient that converts the voltage control error ($V_{ref,j} - V_j$) into a power change signal to control the *PV* system. From the control viewpoint, $K_{j,4}$ can

be any positive value as long as the whole system is stable and meets the performance requirements. In practice, $K_{j,4}$ can be obtained from the Jacobian matrix of the network. Therefore, based on the above assumptions, linearizations and simplifications, the state space model of the proposed system can be developed, which is composed by the PV subsystem dynamics and the grid voltage controller.

Subsystem Dynamics

The subsystem dynamics describe the transient characteristics of the PV systems and the inverter controller. As shown in Fig. 3.2, the state space representation of the subsystem dynamics of PV_j can be written as:

$$\begin{cases} \dot{x}_j(t) = A_j x_j(t) + B_j u_j(t) + H_j \sigma_j(t) \\ y_j(t) = C_j x_j(t) + D_j u_j(t) \end{cases} \quad (3.8)$$

where A_j, B_j, C_j, D_j and H_j can be found in (3.12). The u_j is the input to the subsystem, and $i_{pv.ref,j}$ is the output of the grid voltage controller. The output y_j is the d-axis component of the PV output current i_{dj} , and σ_j is the disturbance. The disturbance is represented as the open circuit voltage (V_{oc} in Fig. 3.2) of the PV panel in this study. V_{oc} will change as the solar irradiance varies.

Grid Voltage Controller

The state space representation of the grid voltage controller is shown in (3.9):

$$\begin{cases} \dot{\rho}_j(t) = A_j^F \rho_j(t) + B_j^F \omega_j(t) \\ u_j(t) = C_j^F \rho_j(t) + D_j^F \omega_j(t) \end{cases} \quad (3.9)$$

where ω_j is the input to the local controller, it is the delayed τ s signal of $(V_{ref,j} - V_j)$. u_j is the output of the controller, which is $i_{pv.ref,j}$, and it is used as the input in (3.8).

$$\begin{aligned}
A_j &= \begin{bmatrix} 0 & 0 & 0 & 0 & 0 & 0 & -K_{I1}/R_{pv} \\ -K_{I2} & 0 & 0 & 0 & 0 & 0 & K_{I2} \\ -K_{P2}/\tau_1 & 1/\tau_1 & -1/\tau_1 & 0 & -1/\tau_1 & 0 & K_{P2}/\tau_1 \\ 0 & 0 & K_{I3} & 0 & 0 & 0 & 0 \\ 0 & 0 & K_{P4}/L & 1/L & -R/L & 0 & 0 \\ 0 & 0 & 0 & 0 & K_2/\tau_2 & -1/\tau_2 & 0 \\ 0 & 0 & 0 & 0 & 0 & -1/C & -1/(R_{pv}C) \end{bmatrix} \\
B_j &= \begin{bmatrix} -K_{I1} \\ 0 \\ 0 \\ 0 \\ 0 \\ 0 \\ 0 \end{bmatrix} \quad H_j = \begin{bmatrix} K_{I1}/R_{pv} \\ 0 \\ K_{P2}/\tau_1 \\ 0 \\ 0 \\ 0 \\ -1/CR_{pv} \end{bmatrix} \\
C_j &= \begin{bmatrix} 0 & 0 & 0 & 0 & 1 & 0 & 0 \end{bmatrix} \quad D_j = \begin{bmatrix} 0 \end{bmatrix}
\end{aligned} \tag{3.12}$$

A_j^F , B_j^F , C_j^F and D_j^F can be found in (3.10):

$$A_j^F = \begin{bmatrix} 0 \end{bmatrix} \quad B_j^F = \begin{bmatrix} K_{j,4}K_{j,I4} \end{bmatrix} \quad C_j^F = \begin{bmatrix} 1 \end{bmatrix} \quad D_j^F = \begin{bmatrix} K_{j,4}K_{j,P4} \end{bmatrix} \tag{3.10}$$

The schematic of the model is shown in Fig. 3.4. In the figure, the transfer functions of P_j and F_j are:

$$P_j = C_j(sI - A_j)^{-1}B_j + D_j \tag{3.11}$$

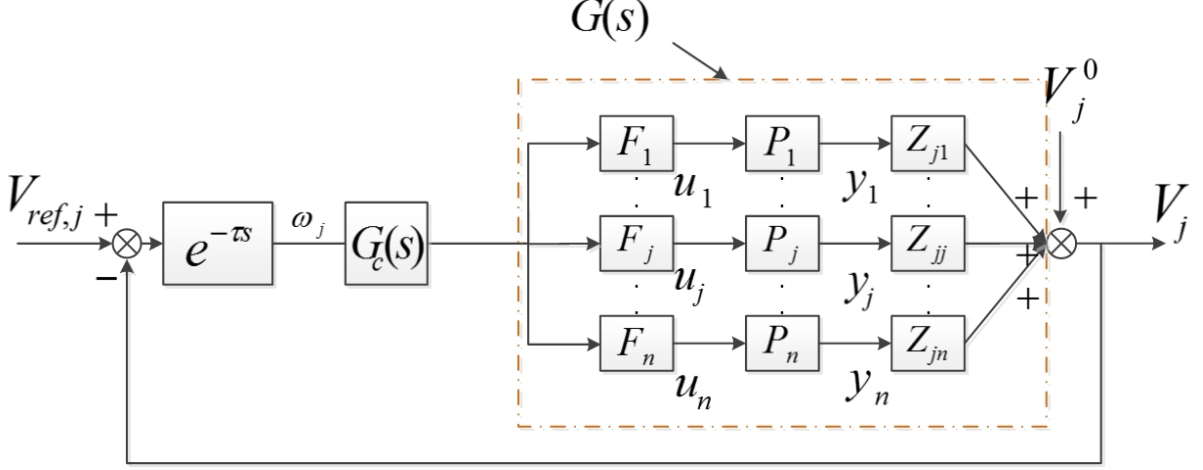


Figure 3.4: The control loop with delay and compensator for bus j in the system.

$$F_j = C_j^F (sI - A_j^F)^{-1} B_j^F + D_j^F$$

In a distribution network with a central controller, the other PVs within the network may be subject to similar communication delays when there is a control signal sent from the same controller. A single delay $T(s) = e^{-\tau s}$ is used in this study to approximate such scenarios. As shown in Fig. 3.4, $G_c(s)$ is the controller to compensate the delay and will be considered and discussed later in Section 3.3. With a slight abuse of notation of variables in time domain and s-domain, u_j can be written as:

$$u_j = F_j \omega_j \quad (3.13)$$

n is the number of PV systems connected into the distribution grid. Z_{ij} is the corresponding \mathbf{Z}_{bus} matrix elements. $G(s)$ can be obtained in (3.14).

$$\begin{aligned} V_j(s) &= (Z_{j1}y_1 + \dots + Z_{jn}y_n)G_c(s)\omega_j \\ &= (Z_{j1}P_1u_1 + \dots + Z_{jn}P_nu_n)G_c(s) = G(s)\omega_j G_c(s) \end{aligned} \quad (3.14)$$

where $G(s) = Z_{j1}P_1F_1 + \dots + Z_{jn}P_nF_n$. The output V_j is now fed back to compare with $V_{ref,j}$ and forms a SISO system that will be used for delay impact analysis and compensator design.

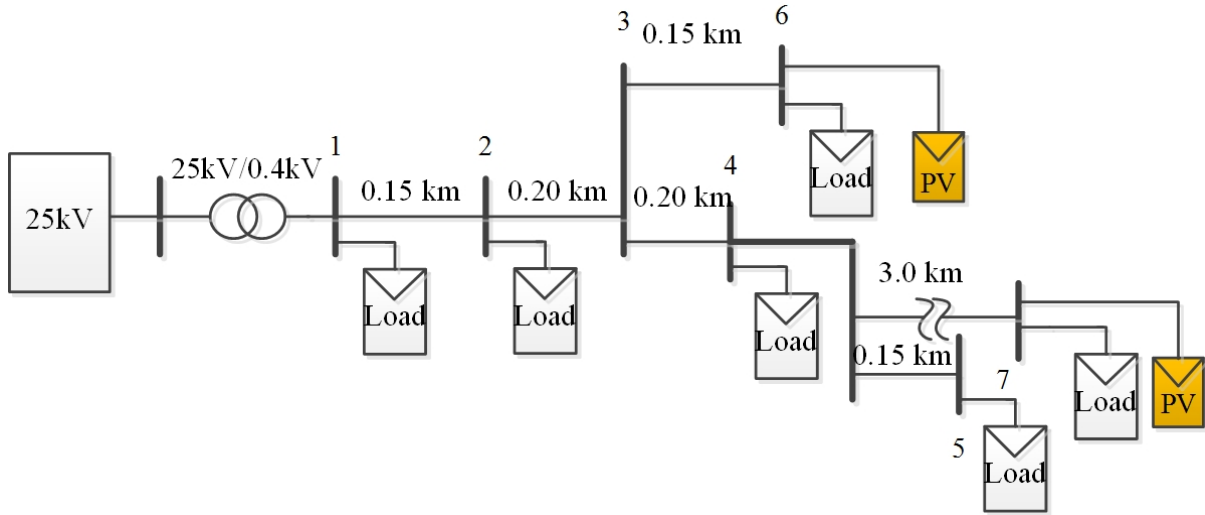


Figure 3.5: Tested distribution network with six sub-communities.

3.2: PV Real power Control for Voltage Regulation

To show how the proposed method helps regulate the voltage based on the PV real power control, a small network as shown in Fig. 3.12 is used to test the method first.

The test network is a residential suburban feeder with 6 sub-communities. The LV feeder is connected to the grid through a 25kV/0.4kV transformer. Each load in Fig. 3.12 represents an individual sub-community with a different power consumption. The PV systems are connected to Nodes 6 and 7 to provide additional power to the grid. Nodes 1 to 6 are relatively close to each other while Node 7 is connected to the network via a 3.0 km power line. The solar irradiance is set to $1000W/m^2$ at $25^\circ C$ to simulate a condition that may generate an undesired voltage profile. The load profiles are given in Table 3.1.

Residential feeders with PVs connected usually have overvoltage issues when the loads of the residential feeders are low during the daytime, especially in a work day. Consequently, the likelihood of overvoltage can be high during that period of time. Moreover, the probability of overvoltage is also increased with higher solar irradiance when the PVs produce more energy than the total load demand. With respect to the control approach

Table 3.1: Resident load profile

Node No.	Load Profile (kW)
1	100
2	13
4	150
5	29
6	120
7	40

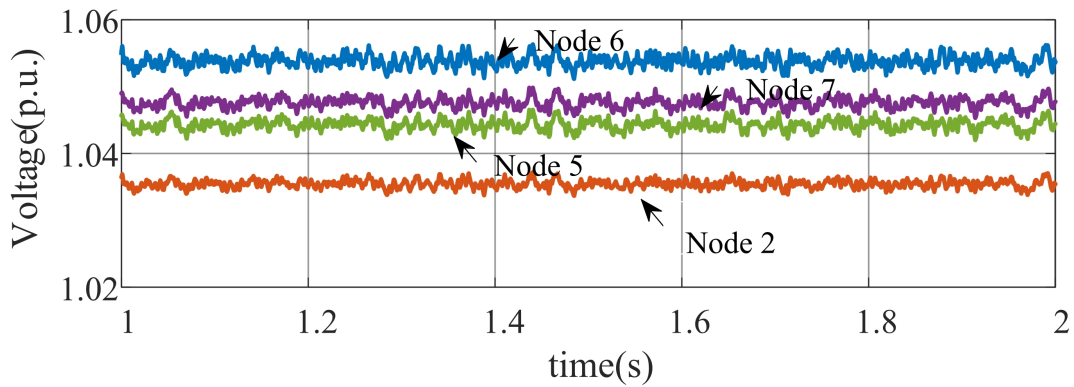


Figure 3.6: Voltages at some nodes & comparison.

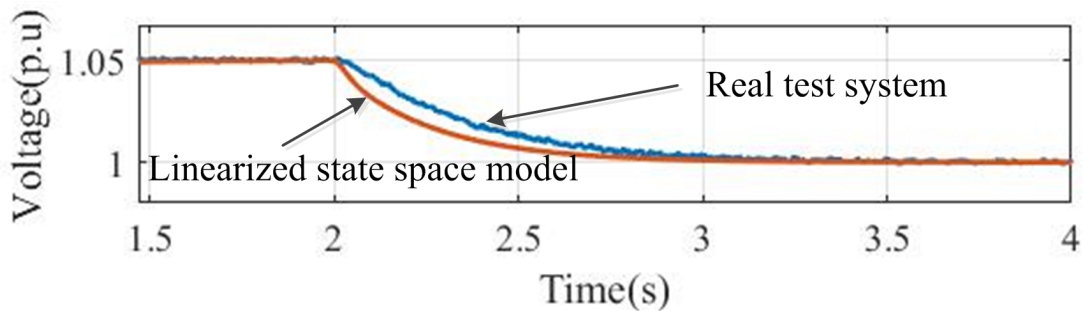


Figure 3.7: Control strategy implementation and comparison.

described in the previous sections, we want to find out the performance of the method when it is applied to the test system when there is no communication delay.

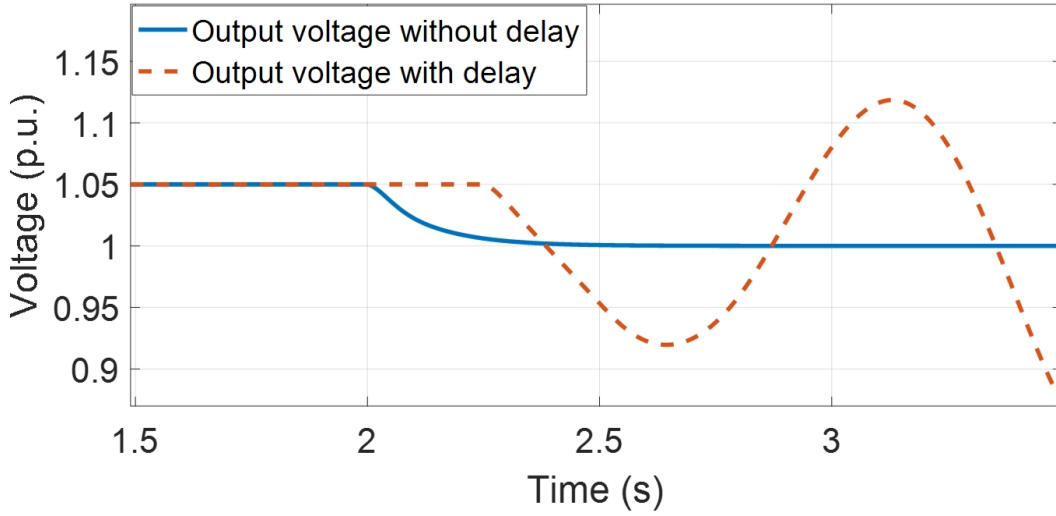


Figure 3.8: Voltage output at Node 6 with control strategy implemented to the small test system (communication delay $\tau = 0.3s$, $K_{I4} = 1$).

It can be seen from the Fig. 3.6 that the voltage of Node 6 (a PV node) has already exceeded the acceptable upper limit (i.e., 1.05 p.u.) when the PV works at maximum power point (MPP). The voltage of another PV node (Node 7) is very close to the limit. Hence, the voltages need to be regulated to provide a safe operation voltage for the devices connected to the feeder. By applying the control strategy discussed in Section II, the voltage of Node 6 can be regulated back to a desired value (i.e., 1.0 p.u.) via real power control, as shown in Fig. 3.7. The result indicates the PV real power control strategy can effectively regulate node voltage when there is no communication delay. The simulation results obtained based on the linearized model in (3.8) and (3.9) are also given in Fig. 3.7. It is noted that the result obtained from the linearized model matches well with the original nonlinear system model. However, when there is a communication delay, the system has a deteriorated performance and can even go unstable, as shown in Fig. 3.8.

Thus, several observations can be obtained from the results shown in Figs. 3.7 and

3.8:

(1) The PV real power control is effective in regulating grid bus voltage when there is no communication delay.

(2) Communication delays deteriorate the system performance and can even cause system instability. Therefore, it is necessary and urgent to find out the maximum delay the system can handle. It is also necessary to design a controller that can compensate the influences of delay to meet the system performance requirements, which will be discussed in the following section.

(3) The developed state space model represents the original system very well. This state space model will be used in designing the controller to compensate communication delays.

3.3: Controller Design to Compensate Communication Delays

As demonstrated in the previous section, delays can cause significant impacts on the overall system performance. It is necessary to accurately identify the system delay margin and to design an effective controller to mitigate the detrimental impacts due to time delays. For the developed SISO system in Fig. 3.4, a classic analysis can be done to obtain the system delay margin and design a controller to mitigate the impacts. Moreover, as it introduced in Chapter 1, LMI approach can provide a sufficient condition of stability in controller design, a control design method by using LMI approach is also studied in this section as well.

3.3.1: Delay Margin

Delay margin (τ_d) is the maximum delay that the system can tolerate. For a delay within the delay margin, the system can stay stable. A delay affects the Bode phase plot of a system while it does not affect the magnitude plot [113]. The delay margin can be

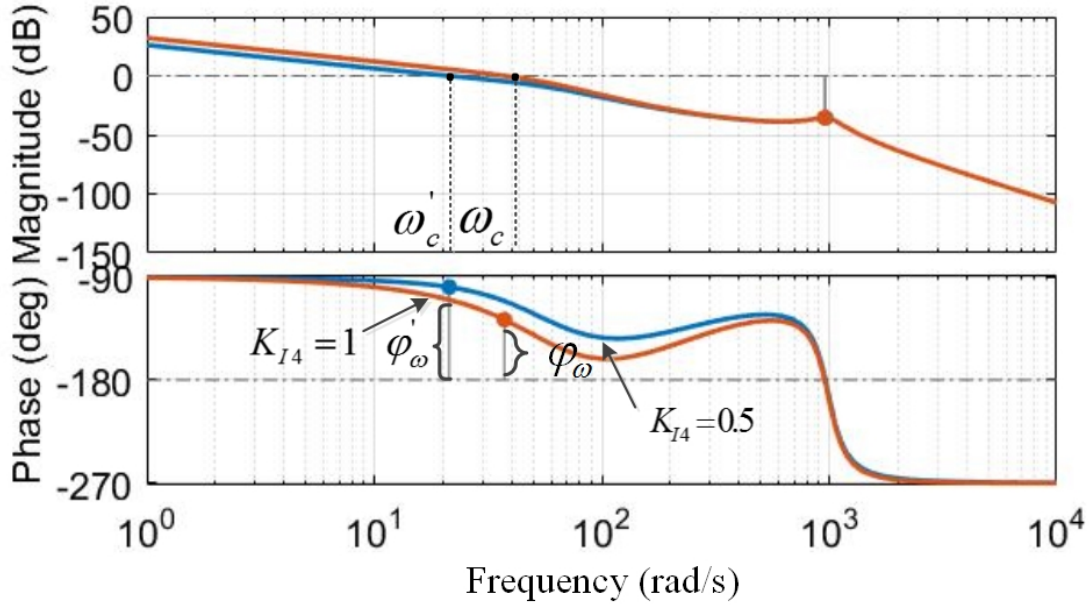


Figure 3.9: Bode plot for different K_{I4} .

obtained from the Bode plot as follows:

$$\tau_d = \frac{\varphi_\omega}{\omega_c} \quad (3.15)$$

where ω_c is the gain crossover frequency, and φ_ω is the original phase margin without the delay, as shown in Fig. 3.9. The closed-loop system is stable if and only if $\tau < \varphi_\omega/\omega_c$.

3.3.2: Controller Design with Single Communication Delays

As indicated in (16), the time delay margin can be increased if the phase margin is improved. Various methods can be used to design a compensator to mitigate the time delay's impacts. Decreasing the parameter of I in the grid voltage controller (K_{I4}) can increase the phase margin. However, the output voltage will response slowly due to a small K_{I4} . The corresponding simulation will be shown and discussed in Section 3.4. Phase lead compensators are effective and widely used for phase margin compensation. The design of a phase lead compensator is given in the following as an illustrative example. The diagram shown in Fig. 3.4 is for the system with multiple PVs that have the same

delays and $G_c(s)$ is the controller to be designed to compensate the delay $e^{-\tau s}$. This can be the case that there is a zone/feeder controller that controls all the PVs in the zone (or along the feeder). The processing time in the zone controller is the main reason for time delay and it is reasonable to assume the multiple PVs have the same time delay.

For the proposed system, the structure of the compensator is shown in (3.16).

$$G_c(s) = K_c \alpha \frac{s + 1/\alpha T}{s + 1/T} \quad (3.16)$$

In a phase lead compensator design, $\alpha > 1$. Select $K_c = 1$ for instance, the phase margin and gain crossover frequency of the delay free system can be readily obtained as about 52° and 37.8 rad/s , respectively.

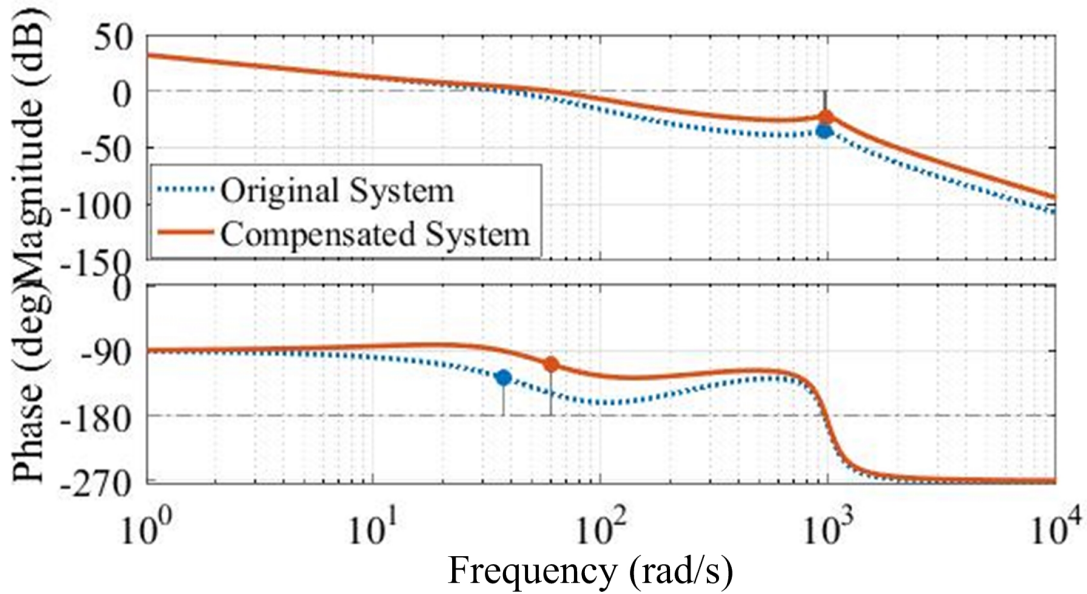


Figure 3.10: Bode plot of the original system & compensated system using G_c .

In order to increase the delay margin, the design goal is to achieve a phase margin of 84° . Therefore, the additional phase provided by the controller near the gain crossover frequency should be $\varphi_c = 84^\circ + 9^\circ - 52^\circ = 41^\circ$, where 9° is the safety factor that can compensate the extra phase shifted at the required frequency due to the increase of the phase

margin. The coefficient a can be calculated as:

$$\alpha = \frac{1 + \sin\varphi_c}{1 - \sin\varphi_c} = \frac{1 + \sin 41^\circ}{1 - \sin 41^\circ} = 4.6 \quad (3.17)$$

The compensator will lift the magnitude upwards by $10\log_{10}(K_c\alpha)$ dB at ω_m ($K_c = 1$), which is the frequency where the phase-lead controller can provide the maximum phase compensation. Thus we choose the compensated gain crossover frequency to be the frequency where

$$|G(j\omega_m)|_{dB} = -10\log_{10}(\alpha) = -6.63dB \quad (3.18)$$

The corresponding frequency is found to be $\omega_m = 60.5$ rad/s at -6.63 dB, $\frac{1}{T} = \sqrt{a}\omega_m = 130$ rad/s. Then $1/aT = 28.2$ rad/s. The transfer function of the phase-lead controller is

$$G_c(s) = K_c\alpha \frac{s + 1/\alpha T}{s + 1/T} = 4.6 \frac{(s + 28.2)}{(s + 130)} \quad (3.19)$$

Fig. 3.10 shows the Bode plot comparison of the original system and the compensated system in the small test system. The phase margin of the system now is 84° and the delay margin is increased to 0.386 s, according to (3.15). The dynamic simulation results will be given in the following section.

3.3.3: Delay-Dependent Time-Invariant Stability Criterion

Consider a system as follows:

$$\dot{x}(t) = Ax(t) + A_d x(t - \tau), \tau \geq 0 \quad (3.12)$$

where τ is the time delay. The system stability holds for $\tau < \tau_d$, where τ_d is the stability margin, and for $\tau > \tau_d$, the system is unstable. Many methods can be used to calculate τ_d . A delay-dependent time-invariant stability criterion proposed in [63] can be used to determine the delay margin of a distribution network with PVs installed:

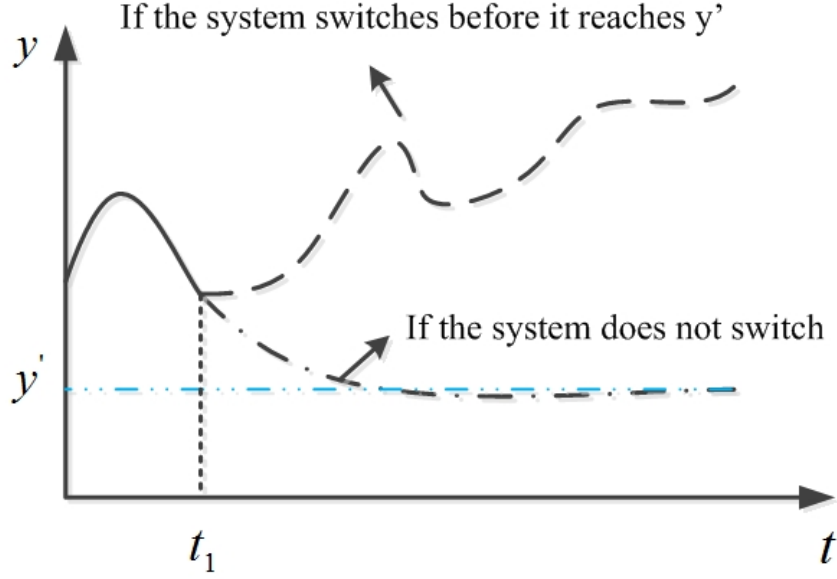


Figure 3.11: Control performance when system switched before it is settled down.

Theorem 1: Assume that an uncertain time-invariant time delay in $[0, \tau_d]$, i.e., $\tau \in [0, \tau_d]$. Then if there exists $P > 0$, $Q > 0$, $V > 0$ and W such that

$$\begin{bmatrix} (1,1) & -W^T A_d & A^T A_d^T V & (1,4) \\ -A_d^T W & -Q & A_d^T A_d^T V & 0 \\ V A_d A & V A_d A_d & -V & 0 \\ (1,4)^T & 0 & 0 & -V \end{bmatrix} < 0 \quad (3.13)$$

where

$$(1,1) \triangleq (A + A_d)^T P + P(A + A_d) + W^T A_d + A_d^T W + Q$$

$$(1,4) \triangleq \tau_d [W^T + P]$$

then the system is asymptotically stable. The proof of this theorem can be found in [114].

3.3.4: Time-varying Communication Delays

The communication delays in the system may not be a constant value, it can change to different values in different time intervals. In this scenario, if a compensator is designed

based on a large delay, one of the issues is the clearing time may violate the required value (less than 1s), according to IEEE 1547 standard [66]. The simulation will be shown in Section 3.4.4. A solution is to design different compensators with respect to different delays. Considering there are two different communication delays τ_1 and τ_2 , the possibilities of those two delays are p_1 and p_2 , respectively. As aforementioned, the performance of the compensator designed for the larger delay τ_1 may not satisfied the IEEE 1547 standard, and it need to be switched to another compensator when delay changed to τ_2 to ensure the clearing time is less than 1s. However, it is possible that the stability of the switching system will not be guaranteed [64, 65].

Considering the system transfer functions with respect to the two different compensators are M_1 and M_2 , respectively, and they are both stable. The following equation can be obtained:

$$y = (qM_1 + (1 - q)M_2)u \quad (3.14)$$

when $q = 1$, τ_1 effects the system; $q = 0$, τ_2 effects the system. When the system switches fast, the nonlinear hybrid system could be unstable due to the fast change of the value of the state. For instance, y is sattling to its desired value y' via the proposed control approach, shown as dot-dash line in Fig. 3.11. At time t_1 , the system is switched to M_2 before y reaches y' . If the impact of M_2 will not continue deceasing the value of y to y' , but instead, y has to be increased due to the new system M_2 (dash line). In this scenario, it is possible that y will rise to some large value and the system may consequently lost its stability. Using a low pass filter can average the change when the system switches and thus can improve the system performance. The simulation example will be shown in Section 3.4.4.

3.4: Simulation Study

In this section, simulation studies are carried out based on the proposed active power control method. The LMI based stability criterion is also studied to calculate the delay margin of the PV connected distributed system. The effectiveness of the voltage regulation method is verified in a delay free system, and the delay margins are calculated according to (3.13), by using different system parameters. After showing the LMI approaches, two different categories of communication delays by using phase lead compensator are studied. For a time invariant communication delay, the proposed method can mitigate the delay impact well according to the simulation. For multiple communication delays' scenario, multiple compensators are designed based on different delays, respectively.

3.4.1: Active Power Voltage Regulation using LMI

The simulation study is carried out in a small test network in Fig. 3.12. The test network is a residential suburban feeder with 6 sub-communities. The LV feeder is connected to the grid through a 25kV/0.4kV transformer. Each load in Fig. 3.12 represents an individual sub-community with a different level of power consumption. The PV systems are connected to Nodes 6 and 7 to provide additional power to the grid. Nodes 1 to 6 are relatively close to each other while Node 7 is connected to the network via a 3.0 km power line. The solar irradiance is set to $1000W/m^2$ at $25^\circ C$ to simulate a condition that may generate an undesired voltage profile. The sizes of the loads are also shown in Fig. 3.12.

The performance of the PV active power curtailment method is shown in Fig. 3.13, where the voltage profile of Node 6 is 1.06 p.u. (solid line), which already exceeds the critical value (1.05 p.u.) set for this study. Overvoltage may cause damage to the electrical

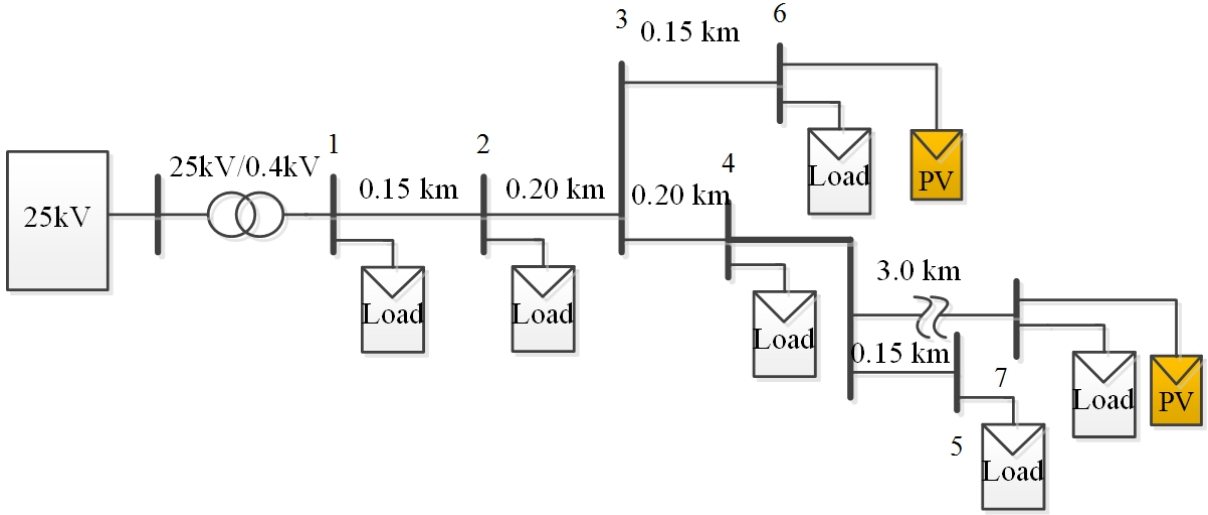


Figure 3.12: Tested distribution network with six sub-communities.

components and the proposed active power control method is applied to control the PV inverter to regulate the voltage back under the critical value. At $t=2$ s, a reference voltage $V_{ref}=1.00$ p.u. is sent from the center controller. The PV at Node 6 curtails its output active power from 287 kW to 130 kW, and the voltage at Node 6 successfully reaches the reference value at $t=2.6$ s. At $t=3.5$ s, a new reference value of $V_{ref}=1.04$ p.u. is set. The PV output then raises to 230 kW, and the voltage of Node 6 shown in Fig. 3.13 is also increased to 1.04 p.u..

3.4.2: Delay-dependent Stability Criterion

The delay-dependent time-invariant stability criterion can be obtained by solving the LMI in (3.13) with different sets of gains of the PI controllers. Table 3.2 shows the different delay margins with respect to different K_{P4} and K_{I4} . The results indicate that for a constant communication delay, the delay margin τ_d increases with the decreasing of K_{P4} and K_{I4} , especially when K_{P4} and K_{I4} are small (e.g., $K_{P4}=0.01$, $K_{I4} = 0.5$). As shown in Fig. 3.14, a very sharp increase can be found when the corresponding parameters are relatively small.

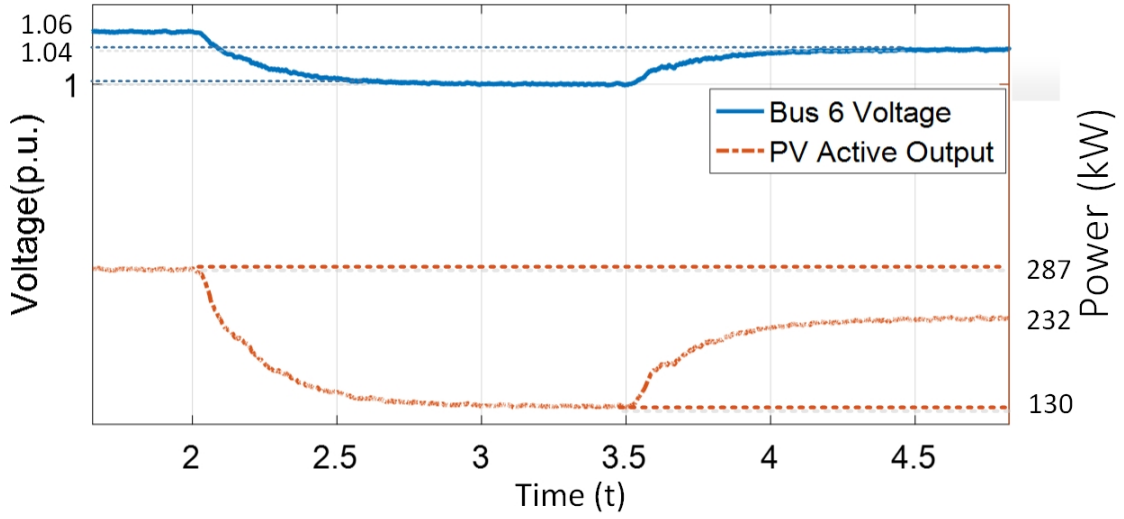


Figure 3.13: Voltage and PV active power output at Node 6.

Table 3.2: Different Delay Margins with respect to K_{P4} & K_{I4}

K_{P4} \ K_{I4}	K_{I4}	0.5	0.75	1.00	1.25	2
	0.100		0.121	0.106	0.101	0.099
0.050		0.334	0.315	0.305	0.287	0.156
0.025		0.681	0.670	0.652	0.447	0.374
0.010		1.200	0.931	0.673	0.491	0.423

The simulation study has also been carried out to verify the accuracy of the calculated delay margin according to the linearized model. Due to the linearization, there is a small error between the calculated value τ_d and the real value obtained from the simulation study. For instance, the delay margin is calculated as 0.156s when $K_{P4}=0.05$, $K_{I4}=2$ (shown in Table 3.2). According to the simulation results given in Fig. 3.15, the real delay margin is found to be 0.144s. When the delays exceed the critical value (e.g., $\tau=0.15$ s), the voltage profile shown in Fig. 3.15 (dash-dot) indicates the system becomes

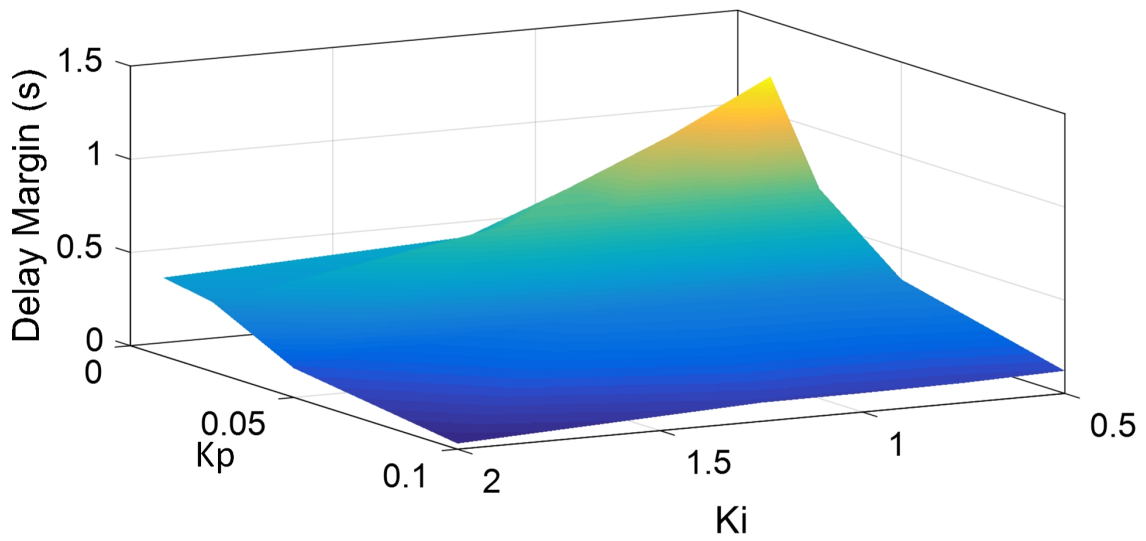


Figure 3.14: Relationships among τ_d , K_{P4} & K_{I4} .

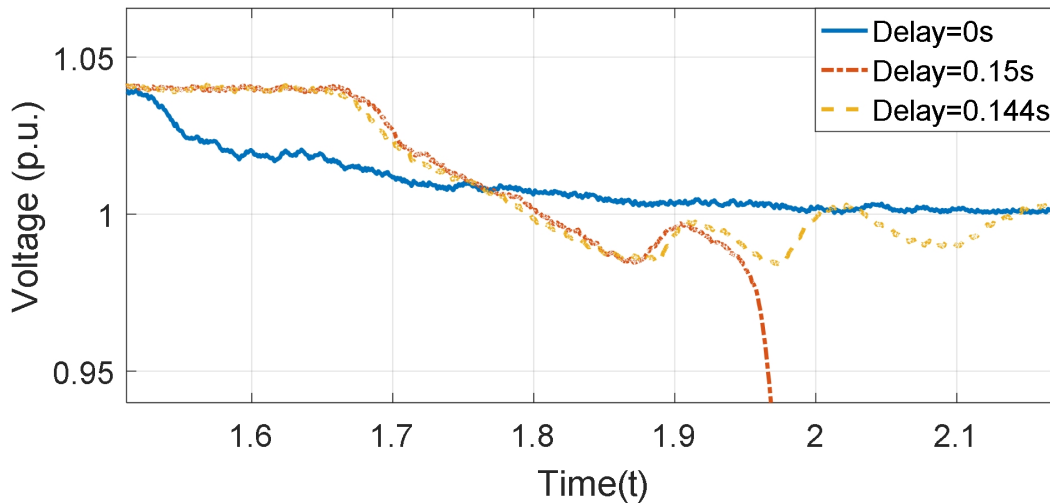


Figure 3.15: Voltage profile at Node 6 with different communication delays.

unstable. The delay margin obtained can help set the upper bound of the communication fault counter [99] to extend the service time. The obtained delay margin can also be used in designing a delay compensator to improve system performance and stability. However, this method only provides a sufficient condition, which can not always guarantee a valid controller to be found. Therefore, the phase lead compensator design will be carried out in order to guarantee a valid controller can always be found with certain delays.

3.4.3: Phase Lead Compensator Small Test System

The Bode plot of the small test system without considering the communication delay is shown in Fig. 3.9 to illustrate how the delay margin is impacted by different parameters of grid voltage controller K_{I4} .

Decreasing K_{I4} can increase the phase margin of $G(s)$ and thus the delay margin will also be increased, according to (3.15). In Fig. 3.9, the Bode plot shows the delay margin of $K_{I4} = 1$ is increased when K_{I4} is changed from 1 to 0.5. A comparison is made in Fig. 3.16 to show how the output voltage responds regarding to different system parameters K_{I4} when the communication delay is set to 0.4s. When K_{I4} is decreased, the influence of the same delay becomes smaller. When $K_{I4} = 0.75$, the oscillation is more obvious than the other two curves. When K_{I4} is decreased to 0.5 and then to 0.25, as shown in Fig. 3.16, the system has a better response. However, decreasing K_{I4} to a smaller value will also slow down the response of the system.

Fig. 3.17 shows the influences of different delays in the proposed small system. The waveforms of the output voltage with 0s, 0.4s and 0.5s delays are compared. It is obvious that the voltage can quickly settle down from the previous value to a desired value without any fluctuation when there is no delay. But with the increasing of the delay τ_d , both the settling time and rise time increased. The growing amplitude of the fluctuation also indicates that the system is losing its stability due to the increase of the delay.

Fig. 3.18 indicates the output voltage at Node 6 after the application of the proposed compensator to the test system. In contrast to the uncompensated system, the compensated system has significant oscillations. The compensated system can successfully follow the reference value and regulate the voltage from 1.05 p.u to 1.00 p.u with decreased oscillation and settling time. The phase-lead compensator can mitigate the impact of

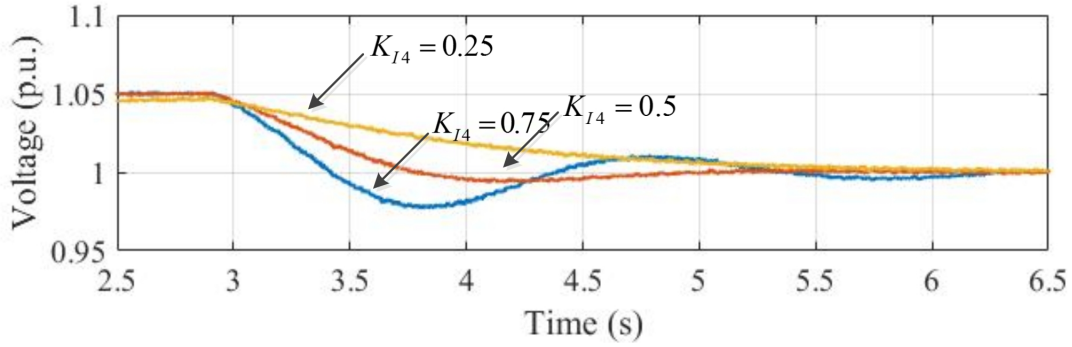


Figure 3.16: Voltage output with different K_{I4} (time delay $\tau = 0.4s$).

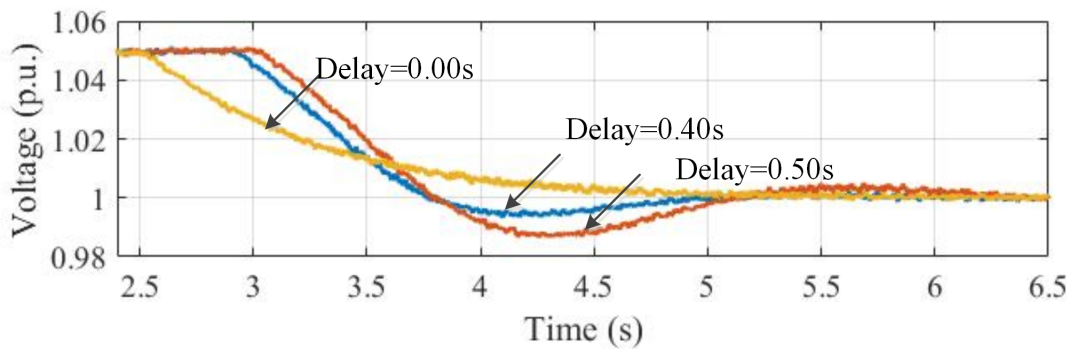


Figure 3.17: Voltage output with different delays ($K_{I4} = 0.5$).

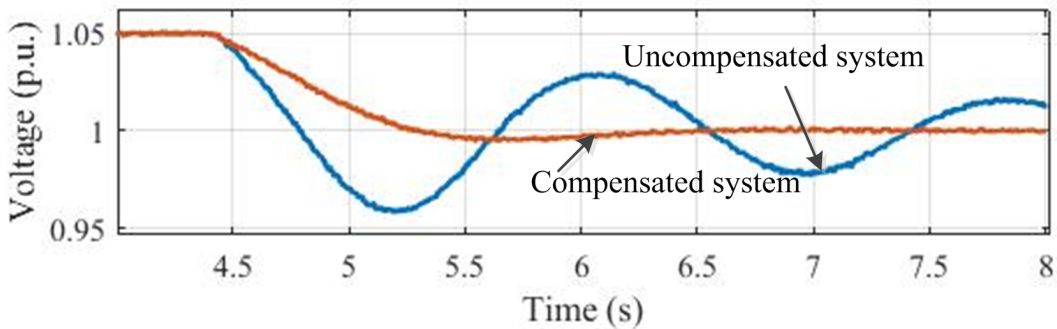


Figure 3.18: Output Voltage with $\tau = 0.4s$ with and without G_c .

communication delays in the system and thus significantly improves its performance.

33-bus Test Feeder

The proposed method is also validated on the 33-bus test feeder system [61], which is shown in Fig. 3.19. Detailed system parameters can be found in [61]. The load connected at bus 19, 21, 32 are composite loads with 50% static part and 50%dynamic part. The

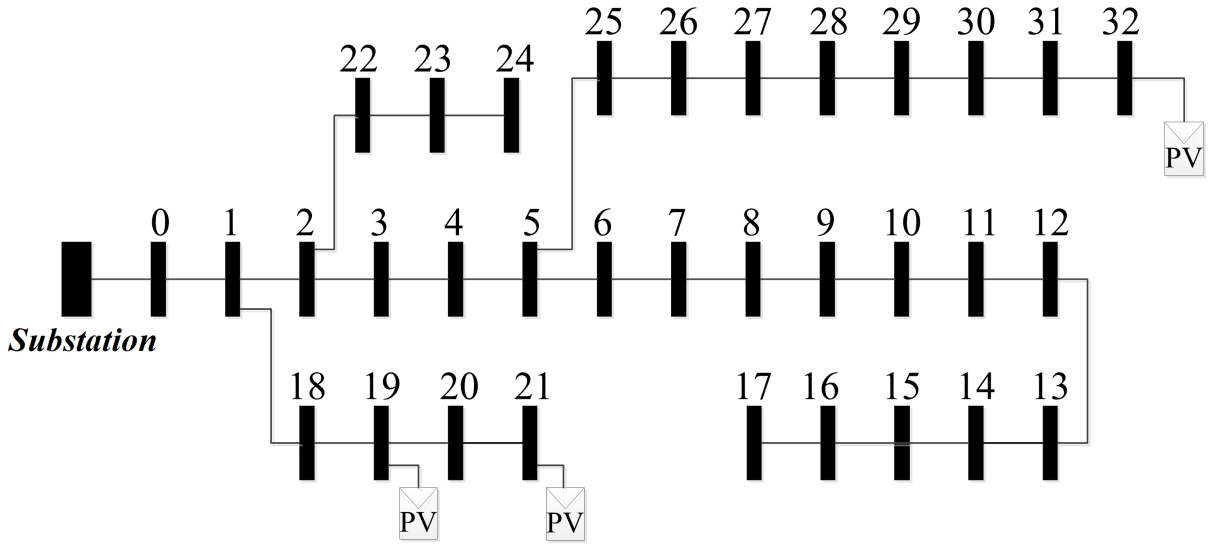


Figure 3.19: PV-connected 33-bus test feeder.

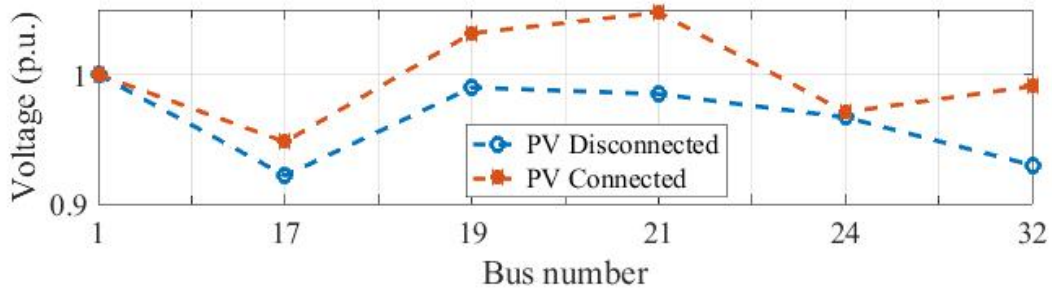


Figure 3.20: Voltage magnitude profile at selected buses.

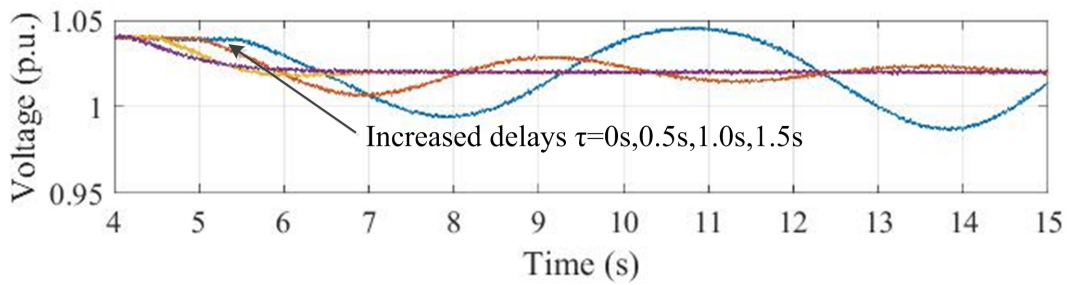


Figure 3.21: Output voltage at bus 21 with different delays in 33-bus test system.

solar irradiance is set to $1000W/m^2$ at $25^\circ C$ as in the test system.

Three PVs are connected to the 33-bus test system, and the voltages at buses 17, 19, 21, 24, 32 in the 33-bus test system are plotted in Fig. 3.20. The five buses are relatively farther from the feeder transformer, and thus the probability of voltage issues

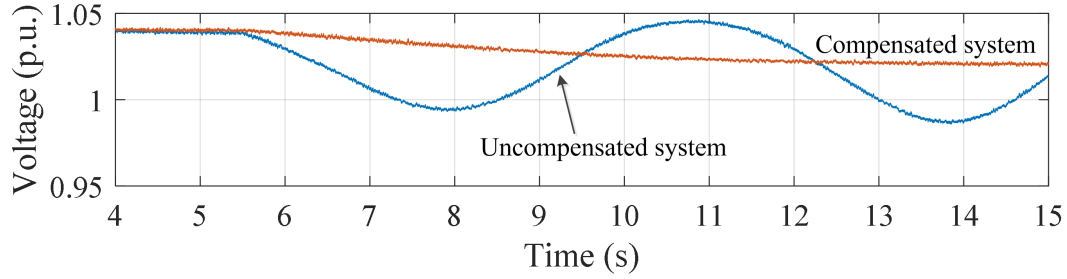


Figure 3.22: Output voltage at bus 21 with/without the compensator ($\tau = 1.5s$).

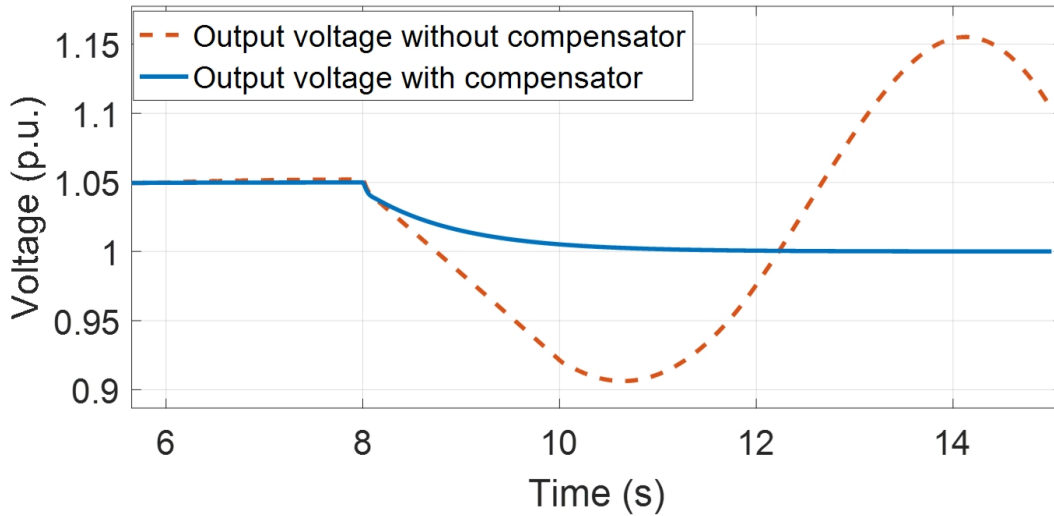


Figure 3.23: Output voltage at bus 21 with/without the compensator ($\tau = 2s$).

occurrence is higher. Among all the plotted data, the voltage at bus 21 has the most significant increasing from 0.99 p.u. to 1.04 p.u. when the PVs are connected. Therefore, it is chosen to illustrate the influences of delay in this system with the designed controller applied.

The voltage at bus 21 is first shown in Fig. 3.21 with respect to five different delays without the proposed compensator. It clearly indicates that although the output voltage still follows the reference value (from 1.04 to 1.02 p.u.), with the increasing of delay, the reference voltage becomes more difficult to follow. Both the settling time and oscillation increase significantly. In contrast, in Fig. 3.22, when using a designed compensator, it not only follows the reference value at 1.04 p.u. within the first few seconds, but it also

can reach 1.02 p.u. from 1.04 p.u. without oscillation.

In addition, as shown in Figs. 3.23, when the delay is increased to 2s, the oscillation of the output voltage changes dramatically, and is not able to follow the reference value any longer because the PV system fails to work.

In contrast, by implementing the proposed compensator, the voltage successfully follows the reference value, shown in Fig. 3.23, which also indicates the phase lead compensator has a good performance in mitigating the impact of delay and consequently stabilize the system.

3.4.4: Switching System with Time-varying Delays

There might be different communication delays in the system. For instance, the delay can change from one value to another at a specific time. One of the solutions is to design a conservative compensator according to the maximum communication delay (τ_m) that may occur in the system. However, according to the interconnection system response to abnormal voltages in IEEE 1547 standard, the clearing time for voltage range between 110% to 120% of base voltage should be less than 1s. As shown in Fig. 3.24, due to the comparatively conservative compensator, for a communication delay $\tau \ll \tau_m$, the system response is so slow that violates the aforementioned clearing time (solid line) requirement. It takes more than 1.7s (t_1) to regulate the voltage at bus 6 to back to under 1.1 p.u.. In contrast, if a compensator is designed based on τ , shown as dash -line in Fig. 3.24, it only uses 0.35s (t_2) to clear the abnormal voltage above 1.1 p.u.. Hence, using only one conservative compensator may not be a good choice for this scenario.

Fig. 3.25 shows the scenario discussed in Section 3.3.4. In the test system, three different communication delays (0.3s, 0.8s, 1s) are studied, and the corresponding compensators are designed. If the delays are switched among those values, the voltage profile

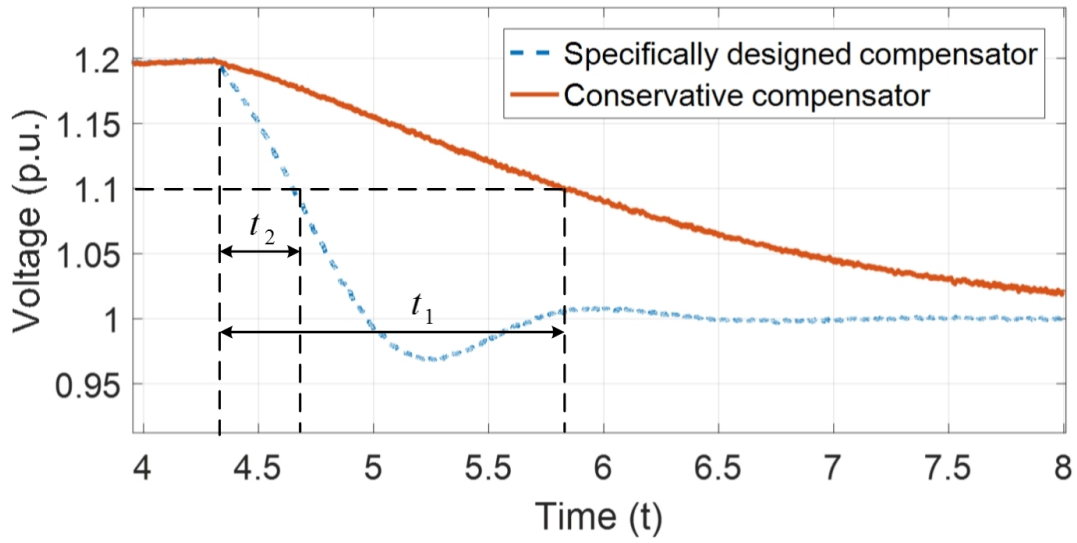


Figure 3.24: Output voltage at bus 6 with different compensators (τ varies with respect to time).

at bus 6 is shown in Fig. 3.25 (dot-line). As we can see, though the compensators works well individually, however, when there are abrupt changes, the system stability is not guaranteed. To overcome this issue, a low-pass filter is designed and connected to the output of ΔP_{ref} . The solid line shown in Fig. 3.25 indicates the system stability is guaranteed and the system can quickly settle to the desired value quickly.

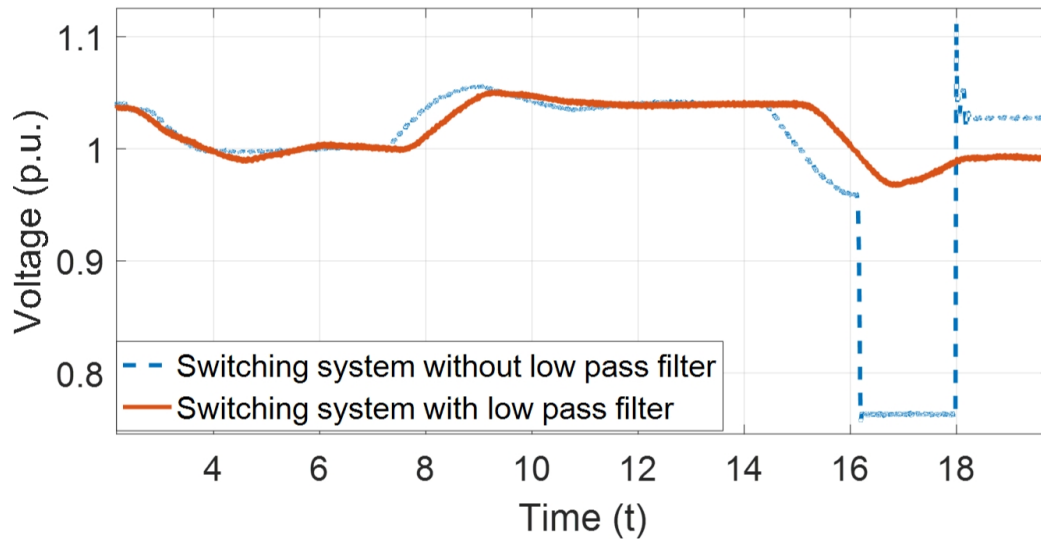


Figure 3.25: Output voltage at bus 6 with/without the low pass filter (τ varies with respect to time).

CHAPTER 4: LOAD FREQUENCY CONTROL WITH COMMUNICATION DELAYS

Nomenclature

τ	Communication delay (s).
τ_m	Communication delay margin (s).
τ_{min}	Minimum communication delay (s).
τ_{max}	Maximum communication delay (s).
G_c	Phase-lead compensator.
ACE	Area control error (p.u.).
ω_0	Synchronous radian frequency (p.u.).
ω_c	Gain-crossover frequency (rad/s).
$\Delta\omega$	Frequency deviation (p.u.).
ΔP_L	Load change, independent of ω (p.u.).
D	Ratio of the percent change in load over ω (%).
H	Inertia constant (s).
M	$M = 2H$ (s).
ΔP_m	Mechanical power output change (p.u.).
ΔP_v	Valve position change (p.u.).
R	Governor speed regulation droop coefficient (p.u.).
T_g	Governor constant (s).
T_{ch}	Turbine time constant (s).
β	Frequency bias factor.

T_{ij}	Synchronizing power coefficient of tie-line ij (p.u./rad).
V_i, V_j	Per unit voltage at bus i and j .
δ_{ij}	Phase angle difference between buses i and j at the equilibrium point.
φ_ω	Phase margin at ω_c .
H_{ii}	Transfer function from input of area i to the output of area i .
H_{ij}	Transfer function from input of area i to the output of area j .
$D_{i,o}$	Value of D with the original base in Area i .
$D_{ik,o}$	Value of D with the k th generator in Area i .
n_i	Number of generators in Area i .
I_n	Coupling index for an n -area LFC schem.

4.1: LFC Schemes with Communication Delays

Dynamic models of one-area LFC and multi-area LFC schemes with communication delays are reviewed in this section. Communication delays usually arise when signals are transmitted between the control center and individual units, such as when telemetered signals are exchanged between RTUs and the control center for signal processing and control law updating, etc. [90]. For the purpose of analysis, in this chapter, all delays are considered as an overall equivalent delay τ in both one-area and multi-area LFC schemes [87].

4.1.1: One-area LFC Model

The dynamic model of a typical one-area LFC scheme is shown in Fig. 4.1. Detailed model of a typical LFC scheme can be found in [96]. Without considering the delay $e^{-\tau s}$

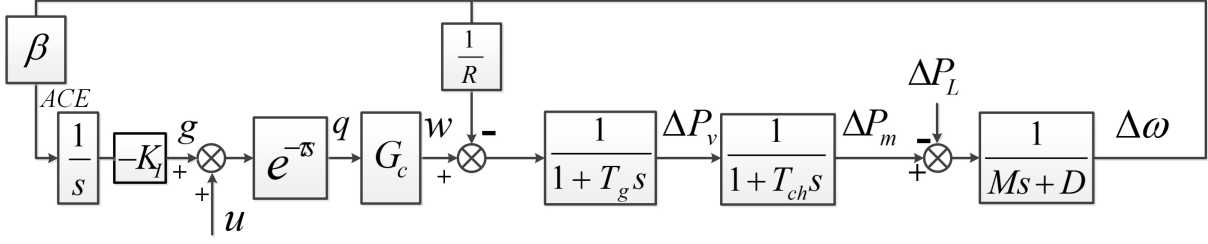


Figure 4.1: One-area LFC scheme with communication delay.

and the delay compensator G_c , the system state-space model can be written as [89]:

$$\begin{cases} \dot{x}(t) = Ax(t) + Bu(t) + F\Delta P_L(t) \\ y(t) = Cx(t) \end{cases} \quad (4.1)$$

where

$$\begin{aligned} x(t) &= \begin{bmatrix} \Delta\omega & \Delta P_v & \Delta P_m & \int ACE \end{bmatrix}^T \\ y(t) &= \begin{bmatrix} \Delta\omega \end{bmatrix} \\ A &= \begin{bmatrix} -D/M & 0 & 1/M & 0 \\ -1/T_g R & -1/T_g & 0 & -K_I/T_g \\ 0 & 1/T_{ch} & -1/T_{ch} & 0 \\ \beta & 0 & 0 & 0 \end{bmatrix} \\ B &= \begin{bmatrix} 0 & 1/T_g & 0 & 0 \end{bmatrix}^T \\ F &= \begin{bmatrix} 0 & -1/M & 0 & 0 \end{bmatrix}^T \\ C &= \begin{bmatrix} 1 & 0 & 0 & 0 \end{bmatrix} \end{aligned}$$

where $u(t)$ is the control signal sent from the control center. Due to no tie-line power exchanges in the one-area LFC scheme, the ACE signal is described as:

$$ACE = \beta\Delta\omega \quad (4.2)$$

where $\beta = 1/R + D$. The total equivalent communication delay is represented as $e^{-\tau s}$ in Fig. 4.1. By defining a new virtual state q , as shown in Fig. 4.1, the following equations can be obtained:

$$\begin{aligned} q(t) &= \begin{bmatrix} 1 & 1 \end{bmatrix} \begin{bmatrix} g(t - \tau) \\ u(t - \tau) \end{bmatrix} \\ &= \begin{bmatrix} 1 & 1 \end{bmatrix} \begin{bmatrix} C''x(t - \tau) \\ u(t - \tau) \end{bmatrix} \\ C'' &= \begin{bmatrix} 0 & 0 & 0 & -K_I \end{bmatrix} \end{aligned} \quad (4.3)$$

In addition, the state-space representation of the controller G_c , which is to be designed in Section 4.3.1, can be written as:

$$\begin{cases} \dot{z}(t) = A_c z(t) + B_c q(t) \\ w(t) = C_c z(t) + D_c q(t) \end{cases} \quad (4.4)$$

where A_c , B_c , C_c , D_c vary according to different G_c controllers. Substituting (4.3) and (4.4) into (4.1), the delayed system including the compensator can be written as:

$$\begin{cases} \dot{f}(t) = A'f(t) + A_d f(t - \tau) + B'u(t - \tau) + F'\Delta P_L(t) \\ y(t) = C'x(t) \end{cases} \quad (4.5)$$

where

$$\begin{aligned}
 f(t) &= \begin{bmatrix} x(t) \\ z(t) \end{bmatrix} \quad A' = \begin{bmatrix} A & BC_c \\ 0 & A_c \end{bmatrix} \\
 A_d &= \begin{bmatrix} BD_c C'' & 0 \\ B_c C'' & 0 \end{bmatrix} \\
 B' &= \begin{bmatrix} BD_c \\ B_c \end{bmatrix} \\
 F' &= \begin{bmatrix} F \\ 0 \end{bmatrix} \\
 C' &= \begin{bmatrix} C'' & 0 \end{bmatrix}
 \end{aligned} \tag{4.6}$$

The one-area LFC can be represented as a single-input-single-output (SISO) system and thus the transfer function can be readily obtained. The frequency domain analysis will be carried out later for the controller design to mitigate the impact of delay.

As shown in Fig. 4.1, the delay compensator is designed for the entire system that includes an integral controller (i.e., I controller) used in the LFC to help regulate frequency. Actually, for the delay compensator design, it does not matter if some other type of controller such as a PI or PID controller is used in the original system.

4.1.2: Multi-area LFC Model

The dynamic model of a multi-area LFC scheme with n control areas is shown in Fig. 4.2. The system state space model without considering the delay can be obtained as [91]:

$$\begin{cases} \dot{x}(t) = Ax(t) + Bu(t) + F\Delta P_L(t) \\ y(t) = Cx(t) \end{cases} \tag{4.7}$$

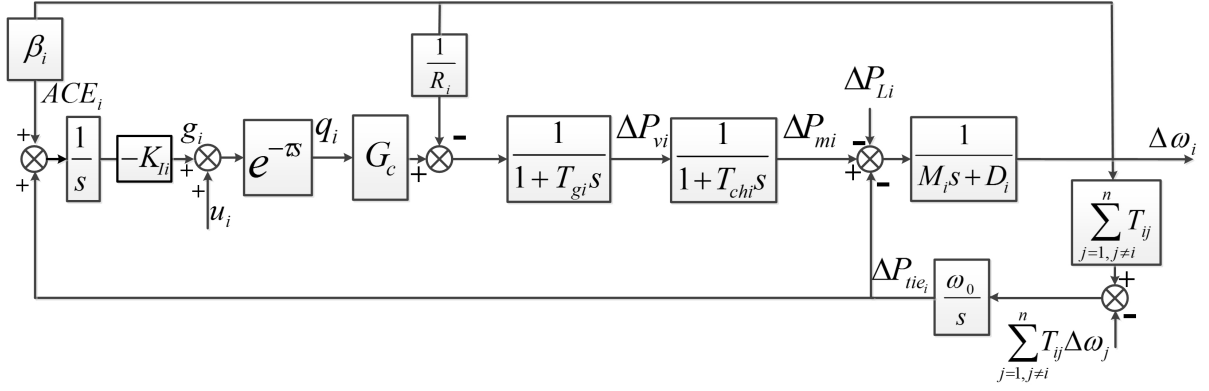


Figure 4.2: Area i in a multi-area LFC scheme with communication delay.

where

$$\begin{aligned}
 x(t) &= \begin{bmatrix} x_1 & \cdots & x_i & \cdots & x_n \end{bmatrix}^T \\
 y(t) &= \begin{bmatrix} y_1 & \cdots & y_i & \cdots & y_n \end{bmatrix}^T \\
 u(t) &= \begin{bmatrix} u_1 & \cdots & u_i & \cdots & u_n \end{bmatrix}^T \\
 x_i(t) &= \begin{bmatrix} \Delta \omega_i & \Delta P_{vi} & \Delta P_{mi} & \int ACE & \Delta P_{tie_i} \end{bmatrix}^T \\
 y_i(t) &= \begin{bmatrix} \Delta \omega_i \end{bmatrix} \\
 \Delta P_L(t) &= \begin{bmatrix} \Delta P_{L1}(t) & \cdots & \Delta P_{Li}(t) & \cdots & \Delta P_{Ln}(t) \end{bmatrix}^T
 \end{aligned}$$

$$A = \begin{bmatrix} A_{11} & \cdots & A_{1i} & \cdots & A_{1n} \\ \vdots & \ddots & \vdots & \ddots & \vdots \\ A_{i1} & \cdots & A_{ii} & \cdots & A_{in} \\ \vdots & \ddots & \vdots & \ddots & \vdots \\ A_{n1} & \cdots & A_{ni} & \cdots & A_{nn} \end{bmatrix}$$

$$B = \text{diag} \left[B_i \right], C = \text{diag} \left[C_i \right]$$

$$F = \text{diag} \left[F_i \right], B_i = \begin{bmatrix} 0 & 1/T_{gi} & 0 & 0 & 0 \end{bmatrix}^T \quad (4.8)$$

$$\begin{aligned}
A_{ii} &= \begin{bmatrix} -D_i/M_i & 0 & 1/M_i & 0 & -1/M_i \\ 1/T_{gi}R_i & 1/T_{gi} & 0 & -K_{Ii}/T_{gi} & 0 \\ 0 & 1/T_{chi} & -1/T_{chi} & 0 & 0 \\ \beta_i & 0 & 0 & 0 & 1 \\ E_i & 0 & 0 & 0 & 0 \end{bmatrix} \\
A_{ij} &= \begin{bmatrix} 0 & 0 & 0 & 0 & 0 \\ 0 & 0 & 0 & 0 & 0 \\ 0 & 0 & 0 & 0 & 0 \\ 0 & 0 & 0 & 0 & 0 \\ -\omega_0 T_{ij} & 0 & 0 & 0 & 0 \end{bmatrix} \\
F_i &= \begin{bmatrix} 0 & 1/M_i & 0 & 0 & 0 \end{bmatrix}^T \\
C_i &= \begin{bmatrix} 1 & 0 & 0 & 0 & 0 \end{bmatrix}, E_i = \omega_0 \sum_{j=1, j \neq i}^n T_{ij}
\end{aligned}$$

Notations are similar to those used in one-area LFC but with subscript i for Area i in a multi-area system. The ACE signal can be represented as:

$$ACE_i = \Delta P_{tiei} + \beta_i \Delta \omega_i$$

The delayed system with n sub-areas can be represented as:

$$\begin{cases} \dot{f}(t) = A'f(t) + \sum_{i=1}^n A_{di}f(t - \tau_i) + B'u(t - \tau_i) + F'\Delta P_L(t) \\ y(t) = C'x(t) \end{cases} \quad (4.9)$$

where

$$\begin{aligned}
 A_{di} &= \text{diag}[0 \cdots \begin{bmatrix} B_i D_{ci} C_i'' & 0 \\ B_{ci} C_i'' & 0 \end{bmatrix} \cdots 0] \\
 u(t) &= \begin{bmatrix} u_1 & \cdots & u_i & \cdots & u_n \end{bmatrix}^T, C' = \text{diag}[C_i'] \\
 C_i' &= \begin{bmatrix} C_i'' & 0 \end{bmatrix}, C_i'' = \begin{bmatrix} 0 & 0 & 0 & -K_{Ii} & 0 \end{bmatrix} \\
 B' &= \text{diag} \begin{bmatrix} B_1' & \cdots & B_i' & \cdots & B_n' \end{bmatrix}
 \end{aligned}$$

Other notations are the same as those in (4.6) with subscript i indicating area i .

4.2: Load Frequency Control Design with Communication Delay

Systems shown in Figs. 4.1 and 4.2 are linear time invariant (LTI) systems when delays do not present. Hence, the impact of delay can be analyzed via a classic approach. For SISO system shown in Fig. 4.1, a necessary and sufficient condition can be obtained for designing a controller to guarantee the stability of the system. It is, however, challenging to analyze a large power system with coupled control areas, which is in general a multi-input-multi-output (MIMO) system as shown in Fig. 4.2. The interactions among different control areas in a multi-area LFC are discussed in this section. The small gain theorem [115] is used to demonstrate and verify that the delay compensator for each control area can be designed independently in the way as in a single one-area system if the coupling index among different areas is below the threshold value (more discussions given later in this section).

4.2.1: Delay Margin

For a SISO LTI and open-loop stable system, delay margin (τ_m) is the maximum time delay that the system can tolerate. The time delay affects the Bode phase plot of the system while it does not affect the magnitude plot [113]. The delay margin can be

obtained according to the following equation:

$$\tau_m = \frac{\varphi_\omega}{\omega_c} \quad (4.10)$$

It is a necessary and sufficient condition that the closed system with time delay is stable when the delay $\tau \leq \tau_m$.

4.2.2: Compensator Design for One-area LFC with Communication Delay

The one-area LFC scheme shown in Fig. 4.1 is a SISO system. The communication delay exists in the system can be treated as one equivalent delay in the transmission of ACE [89]. Let $G(s)$ be the open-loop system transfer function without delay and the delay compensator. $G(s)$ can be derived from its state space model in (4.1). Let $e^{-\tau s}$ be the communication delay, and $G_c(s)$ be the compensator to be designed.

The design of a phase lead compensator is given below as an illustrative example. For system $G(s)$, the structure of the phase lead compensator can be written as [93]:

$$G_c(s) = \alpha \frac{s + 1/\alpha T}{s + 1/T} \quad (4.11)$$

Denoting $\varphi_{\omega d}$ as the desired phase margin, $\varphi_{\omega u}$ as the uncompensated phase margin, and $\varphi_{\omega s}$ as the safety factor, α can be calculated based on [93]:

$$\alpha = \frac{1 + \sin\varphi}{1 - \sin\varphi} \quad (4.12)$$

where $\varphi = \varphi_{\omega d} - \varphi_{\omega u} + \varphi_{\omega s}$. The compensator will lift the magnitude upwards by $10 \cdot \log_{10}(\alpha)$ dB at ω_m , where ω_m is the corner frequency of (4.11). Choose ω_m as the new gain-crossover frequency of the compensated system to maximize the phase margin compensation. That is $|G_c(j\omega_m)G(j\omega_m)| = 0$ dB. In other words, $|G(j\omega_m)|_{dB} = -10 \cdot \log_{10}(\alpha)$. Once the frequency ω_m is identified, the compensator $G_c(s)$ can be calculated based on $\frac{1}{T} = \sqrt{\alpha}\omega_m$.

4.2.3: Multi-area LFC with Communication Delays

In a multi-area LFC scheme, due to different load changes in different areas, and tie-line power interactions, the controller design becomes an MIMO system based design and the couplings among individual areas need to be studied carefully. On the one hand, since different control areas are linked via tie-lines, load change in one area will also impact the other areas. Moreover, each area has its own ACE based control and one of the control objectives is to maintain the power flows at a given level along the tie-lines. In other words, under a certain equilibrium point, each control area is controlled to take care of its own load changes unless a new set of tie-line power references are issued. Therefore, if different areas are not strongly coupled, the delay compensator design procedure for a MIMO system can still follow the one developed for the one-area LFC scheme. That is, the delay compensator for each control area can still be designed independently if the area is not strongly coupled with the rest of the system. This is a decentralized delay compensation scheme. We will use the small gain theorem [115] to analyze the couplings among different sub-systems in an MIMO system.

The equivalent diagram of a multi-area LFC scheme is shown in Fig. 4.3. For a single area in the figure, e.g., Area 1, the area topology can be represented by a feedback transfer function H_{11} and a forward transfer function G_1 . H_{11} and G_1 are derived according to Fig. 4.2 without considering the impact from other areas. The impacts from the i th area to Area 1 are, however, represented by two parts: H_{i1} and C_{i1} . The C_{i1} is the transfer function indicating signal from $\Delta\omega_i$ to $\Delta\omega_1$, which can be derived by Mason's Rule. The feedback from area i to this area (Area 1), shown as H_{i1} in the lower part of Fig. 4.3, is presented as $H_{i1} = K_{Ii}T_{i1}\omega_0/s^2$. The overall impact from all other areas to Area 1 can thus be represented as $\sum_{j=2}^n H_{j1}\Delta\omega_j$ (the feedback to the input) and $\sum_{j=2}^n C_{i1}\Delta\omega_j$ (to

the output), shown in Fig. 4.3.

Taking a two-area LFC scheme for instance, a more generic diagram representation is shown in Fig. 4.4. H_{12} and H_{21} are the feedback transfer functions from $\Delta\omega_1$ to Area 2 and $\Delta\omega_2$ to Area 1, respectively. The relationship between the inputs \mathbf{u} and outputs \mathbf{y} can be found in (4.13).

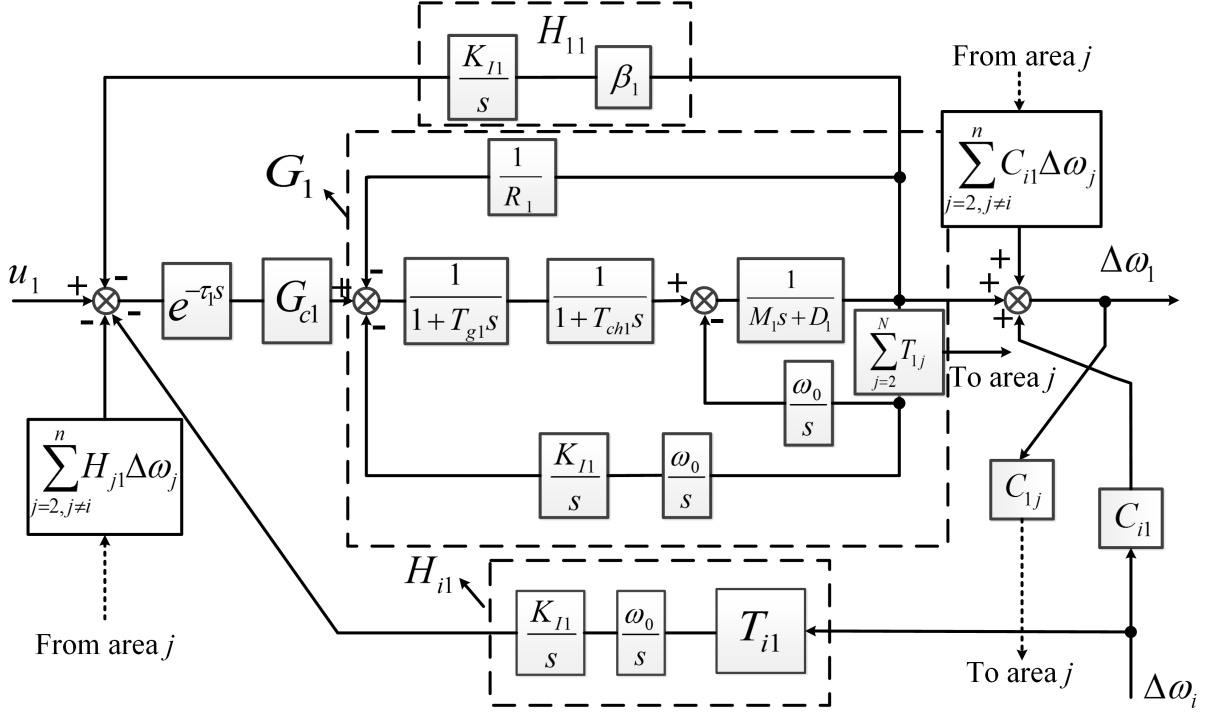


Figure 4.3: Area 1 to the i th area of a multi-area LFC scheme.

$$\begin{bmatrix} y_1 \\ y_2 \end{bmatrix} = \mathbf{P}_2 \begin{bmatrix} u_1 \\ u_2 \end{bmatrix} - \mathbf{M}_2 \begin{bmatrix} y_1 \\ y_2 \end{bmatrix} \quad (4.13)$$

where

$$\mathbf{M}_2 = \begin{bmatrix} G_1 G_{c1} e^{-\tau_1 s} H_{11} & G_1 G_{c1} e^{-\tau_1 s} H_{21} - C_{21} \\ G_2 G_{c2} e^{-\tau_2 s} H_{12} - C_{12} & G_2 G_{c2} e^{-\tau_2 s} H_{22} \end{bmatrix}$$

$$\mathbf{P}_2 = \begin{bmatrix} G_1 G_{c1} e^{-\tau_1 s} & 0 \\ 0 & G_2 G_{c2} e^{-\tau_2 s} \end{bmatrix}$$

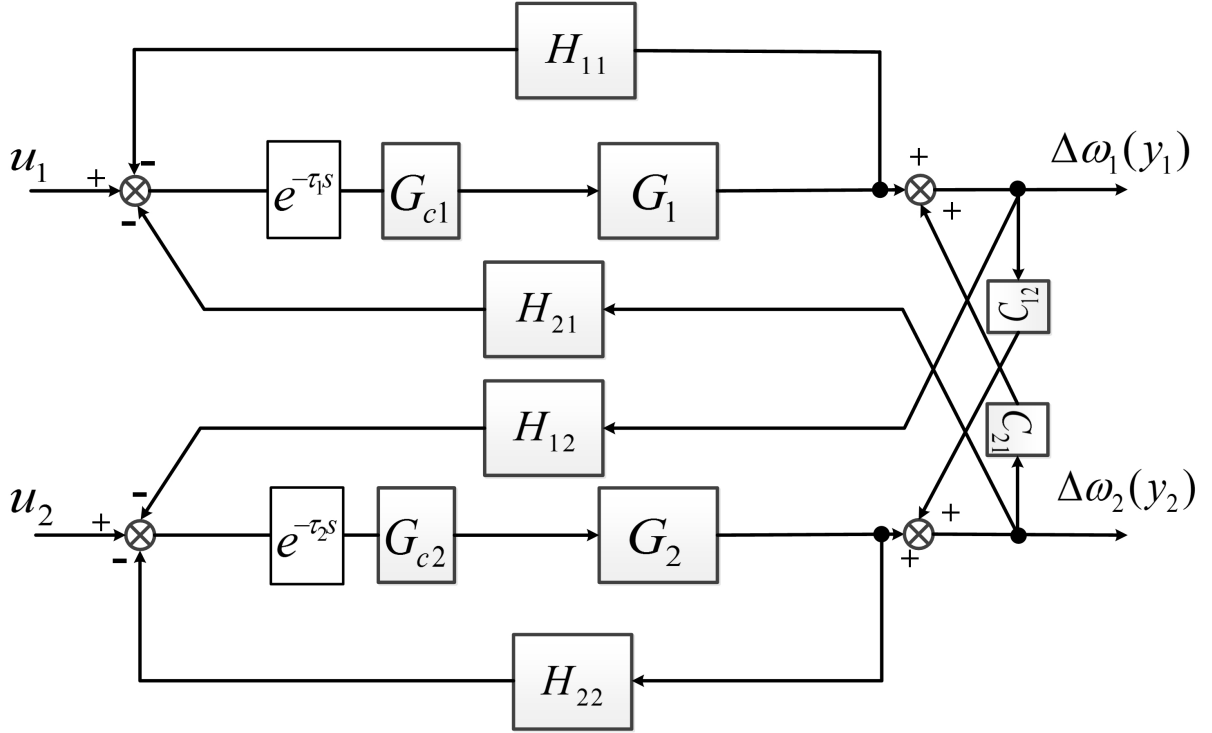


Figure 4.4: A generic two-area LFC scheme.

The closed-loop transfer function of the two-area LFC scheme can be obtained as:

$$\mathbf{y} = (\mathbf{I} + \mathbf{M}_2)^{-1} \mathbf{P}_2 \cdot \mathbf{u} \quad (4.14)$$

The stability criteria of system in (4.14) is that $[\mathbf{I} + \mathbf{M}_2]^{-1}$ is stable, since \mathbf{P}_2 is stable.

$$\begin{aligned}
 (\mathbf{I} + \mathbf{M}_2)^{-1} = & \\
 & \left(\begin{bmatrix} 1 + G_1 G_{c1} e^{-\tau_1 s} H_{11} & 0 \\ 0 & 1 + G_2 G_{c2} e^{-\tau_2 s} H_{22} \end{bmatrix} \right. \\
 & \left. + \begin{bmatrix} 0 & G_1 G_{c1} e^{-\tau_1 s} H_{21} - C_{21} \\ G_2 G_{c2} e^{-\tau_2 s} H_{12} - C_{12} & 0 \end{bmatrix} \right)^{-1}
 \end{aligned}$$

Let

$$\mathbf{N}_2 = \begin{bmatrix} 1 + G_1 G_{c1} e^{-\tau_1 s} H_{11} & 0 \\ 0 & 1 + G_2 G_{c2} e^{-\tau_2 s} H_{22} \end{bmatrix}$$

$$\mathbf{\Delta}_2 = \begin{bmatrix} 0 & G_1 G_{c1} e^{-\tau_1 s} H_{21} - C_{21} \\ G_2 G_{c2} e^{-\tau_2 s} H_{12} - C_{12} & 0 \end{bmatrix}$$

$(\mathbf{I} + \mathbf{M}_2)^{-1}$ can thus be written as $[\mathbf{N}_2 + \mathbf{\Delta}_2]^{-1}$. This can be further written as $[\mathbf{I} + \mathbf{N}_2^{-1} \mathbf{\Delta}_2]^{-1} \mathbf{N}_2^{-1}$. \mathbf{N}_2^{-1} is stable due to the local stability: the diagonal elements in \mathbf{N}_2^{-1} are the denominators of the closed loop transfer function of each subsystem, and all the subsystems are assumed to be stable. Define the coupling index I_2 of this two-area LFC scheme as $\|\mathbf{N}_2^{-1} \mathbf{\Delta}_2\|_\infty$. In order to determine the stability of (4.14),

$$I_2 = \|\mathbf{N}_2^{-1} \mathbf{\Delta}_2\|_\infty < 1 \quad (4.15)$$

should be satisfied [80].

Equation (4.15) can be further written as:

$$\|\mathbf{N}_2^{-1} \mathbf{\Delta}_2\|_\infty \leq \|\mathbf{N}_2^{-1}\|_\infty \cdot \|\mathbf{\Delta}_2\|_\infty < 1 \quad (4.16)$$

Thus, the stability criteria of system in (4.14) is:

$$\|\mathbf{\Delta}_2\|_\infty < \frac{1}{\|\mathbf{N}_2^{-1}\|_\infty} \quad (4.17)$$

The discussion on the two-subsystem system can be extended to a multi-area system (e.g., an n -area LFC scheme). The coupling index I_n is defined as $\|\mathbf{N}_n^{-1} \mathbf{\Delta}_n\|_\infty$, and the stability is determined by (4.18):

$$I_n = \|\mathbf{N}_n^{-1} \mathbf{\Delta}_n\|_\infty < 1 \quad (4.18)$$

or equivalently

$$\|\mathbf{\Delta}_n\|_\infty < \frac{1}{\|\mathbf{N}_n^{-1}\|_\infty} \quad (4.19)$$

where

$$\mathbf{N}_n = \text{diag}[1 + G_i G_{ci} e^{-\tau_i s} H_{ii}]$$

$$\mathbf{\Delta}_n = \begin{bmatrix} 0 & \cdots & G_n G_{cn} e^{-\tau_1 s} H_{n1} - C_{n1} \\ \vdots & \ddots & \vdots \\ G_i G_{ci} e^{-\tau_i s} H_{1i} - C_{1i} & \cdots & G_i G_{ci} e^{-\tau_i s} H_{ni} - C_{ni} \\ \vdots & \ddots & \vdots \\ G_n G_{cn} e^{-\tau_n s} H_{1n} - C_{1n} & \cdots & 0 \end{bmatrix}$$

4.3: Simulation Study

Simulation studies are carried out for both one-area and multi-area LFC schemes to verify the proposed method. A one-area LFC based phase lead compensator design considering communication delay is first discussed to illustrate the proposed procedure. The design is then extended to the multi-area LFC scheme with multiple time-varying communication delays in different sub-areas.

4.3.1: One-area LFC

Parameters for the one-area LFC are shown in Table 4.1 [96].

Table 4.1: Parameters of One-area LFC Scheme

Parameters	M	D	β	R	K_I	T_g	T_{ch}	ΔP_L
Area ₁	10	0.8	20.8	0.05	7	0.2	0.5	0.2

Bode plots show that the phase margin ω_m and crossover frequency can be readily obtained according to Fig. 4.5 (dotted line). Using the design procedure described in Section 4.2.2, choose $K_c = 1$ and $\varphi = 30^\circ$ for instance, it is easy to get $\alpha = 3$ and

$|G(j\omega_m)|_{dB} = -10 \cdot \log_{10}(\alpha) = -4.7\text{dB}$. The frequency is found to be $\omega_c = 4.1 \text{ rad/s}$ at that amplitude. Therefore, $1/T$ and $1/\alpha T$ in (4.11) can be calculated as 7.1 rad/s and 2.37 rad/s , respectively. Therefore, the transfer function of the phase lead controller is shown in (4.20).

$$G_c(s) = 3 \frac{s + 2.37}{s + 7.1} \quad (4.20)$$

Bode plot of the compensated system and the simulation results are shown in Figs. 4.5 (solid line) and 4.6, respectively. For a 0.2 p.u. load change ($\Delta P_L = 0.2 \text{ p.u.}$), with a communication delay of 0.5s , both the ACE signal and $\Delta\omega$ show increasing in the amplitude of the oscillation (dash line), which means the system is unstable. By using the proposed compensator (shown as solid line in Fig. 4.6), $\Delta\omega$ can quickly settle to the desired value 0 with negligible oscillations. The ACE signal also has a good performance with an overshoot less than 0.01 p.u. and a short settling period as well.

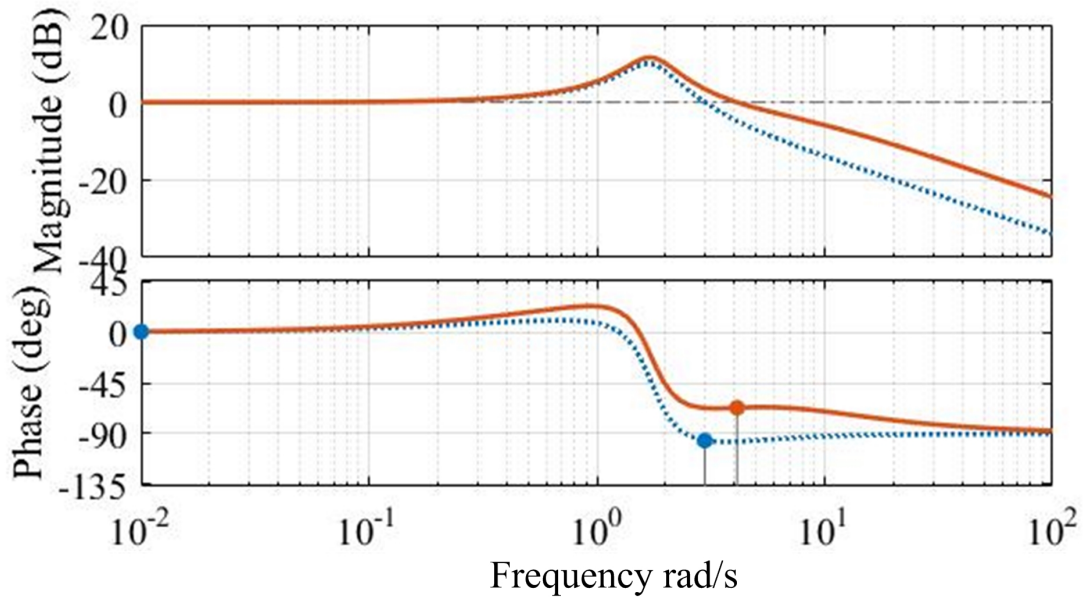


Figure 4.5: Bode plot of the original system (Dash) and the compensated system (Solid).

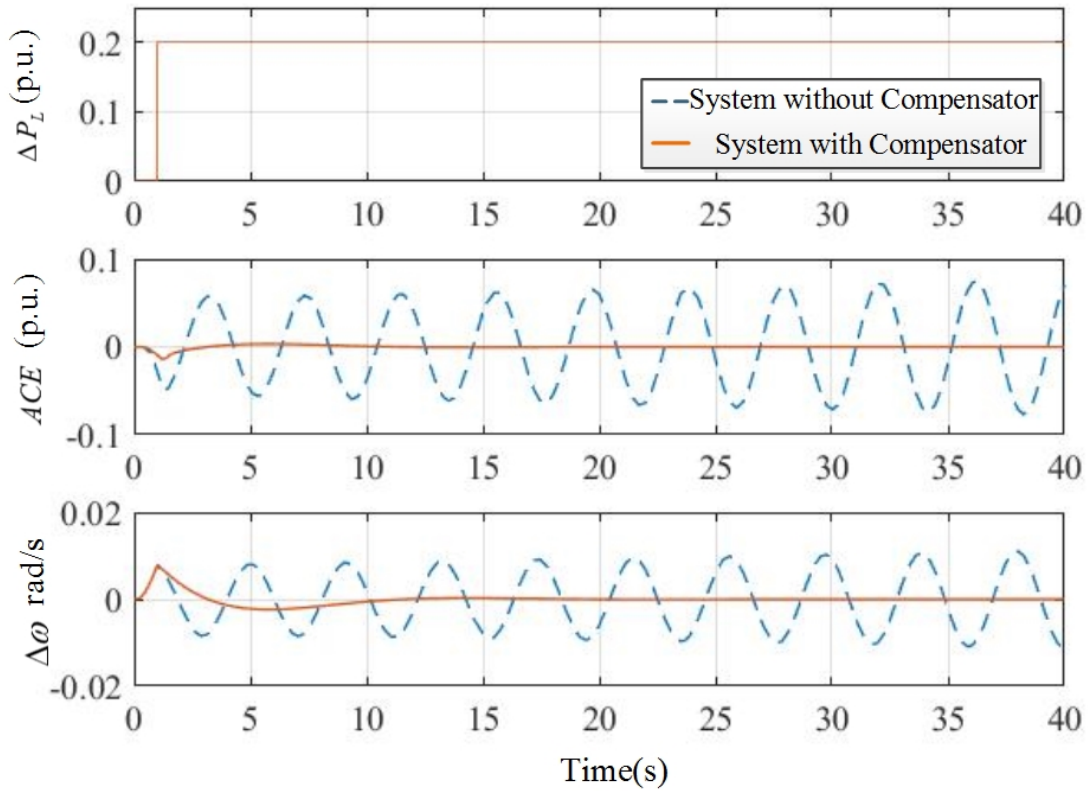


Figure 4.6: One-area system response of 0.5s delay following a 0.2 p.u. load change using proposed compensator (Solid) and without compensator (Dash).

4.3.2: Multi-area LFC

For a multi-area LFC scheme, as described in Section 4.2.3, the equivalent design can be achieved if (4.18) is satisfied. Two simulations are carried out and discussed: a five-area system based on data from a 68-bus system [77], and a ten-area LFC system extended from the aforementioned five-area system. The five-area system simulation study illustrates the effectiveness of the proposed method in multi-area LFC schemes. Simulation results on the ten-area system show that the proposed method can be applied to large systems in practice even if the coupling among each area becomes stronger as the size of the system increases, i.e., the number of control areas gets larger.

Five-area LFC using 68-bus system data

Simulation is carried out based on the IEEE 68-bus system with a total 16 generators in 5 different areas. In this 5-area, 68-bus system, the New York power system (NYPS) has four generators and the New England test system (NETS) has nine generators while the other three areas are represented by their corresponding equivalent single-generator models. The following procedures can be taken to obtain the parameters of the equivalent single-generator models for the NYPS and the NETS [94]:

$$D_{i,o} = \sum_{k=1}^{n_i} D_{ik,o}; M_{i,o} = \sum_{k=1}^{n_i} M_{ik,o}; \beta_{i,o} = \sum_{k=1}^{n_i} \left(D_{ik,o} + \frac{1}{R_{ik,o}} \right)$$

Notations of D , M , R , and β are the same as those used in Section 4.1.1.

To convert the parameters to a new base $S_{base} = 1000$ MVA, the following equations can be used:

$$D_i = \frac{S_{base,o}}{S_{base}} D_{i,o}; M_i = \frac{S_{base,o}}{S_{base}} M_{i,o}; R_i = \frac{S_{base}}{S_{base,o}} R_{i,o}$$

Therefore, equivalent single-generator models of NYPS and NETS can be obtained and parameters of the five-area system are given in Table 4.2.

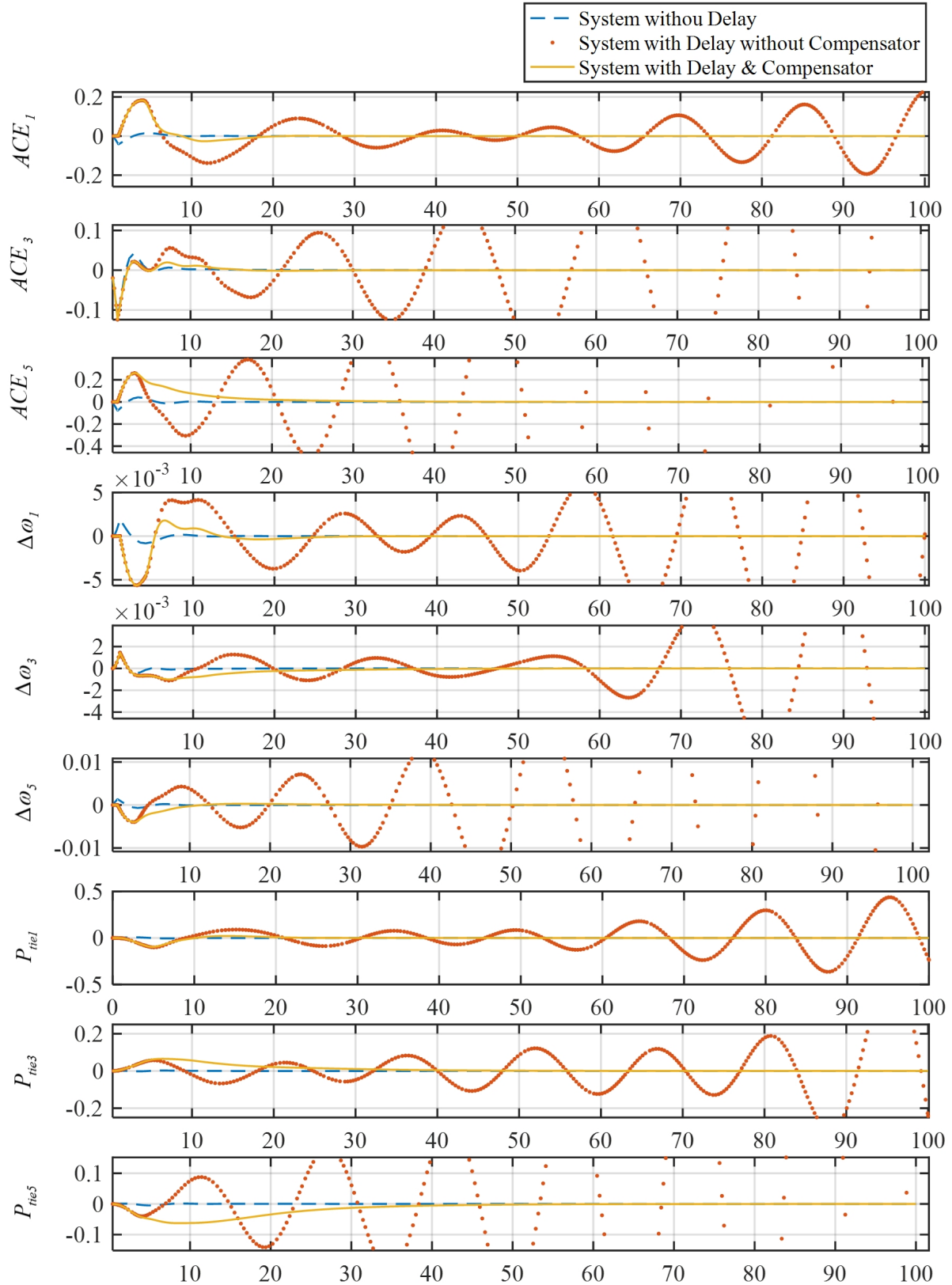


Figure 4.7: Proposed method in a 5-area system: a) Only a 4s communication delay is applied to Area 3, the delay in other areas are 0s. b) Each area has a communication delay: 4s, 5s, 4s, 6s, 3s, respectively.

Table 4.2: Parameters of Five-area LFC Scheme

Para.	M_i	D_i	β_i	R_i	K_{Ii}	T_{gi}	T_{chi}	ΔP_{Li}
Area ₁	30	0.8	20.8	0.05	0.3	0.2	0.5	0.20
Area ₂	30	1.0	19	0.0556	0.3	0.3	0.6	0.10
Area ₃	65	3	84	0.0125	0.1	0.2	0.5	0.25
Area ₄	45	1.2	17.2	0.0625	0.3	0.4	0.6	0.15
Area ₅	56.52	0.72	58	0.02	0.2	0.2	0.5	0.20

Based on parameters given in Table 4.2, values of $\|\Delta_{\mathbf{5}}\|_{\infty}$ and $\frac{1}{\|\mathbf{N}_5^{-1}\|_{\infty}}$ are calculated to be 0.173 and 0.917, respectively, which satisfy (4.19). Simulation results of the five-area system are shown in Fig. 4.7. Due to space limit, only Areas 1, 3, and 5 are shown. Fig. 4.7 indicates the scenario that the communication delays exist in all five areas. Increasing oscillations in ACE , $\Delta\omega$ and P_{tie} in all three areas imply communication delays do negatively impact the system performance and stability. The system responses without compensators show that the system loses its stability in all five areas. With the compensators that are designed for each area separately, as shown by the solid line, the impacts of delays are mitigated, and the whole system remains stable. All the responses shown in Fig. 4.7 can be quickly settled down in a short period of time with negligible oscillations.

Ten-area LFC with Time-varying Delay

Since delays can happen in a random way [81], time-varying random delays which changes every 0.1s within the range $[\tau_{max}/3, \tau_{max}]$ are used in this simulation study. The delay compensator can be designed for the worst-case scenario so that, theoretically, the impact of any delay smaller than τ_{max} can be mitigated [93]. In the ten-area LFC system,

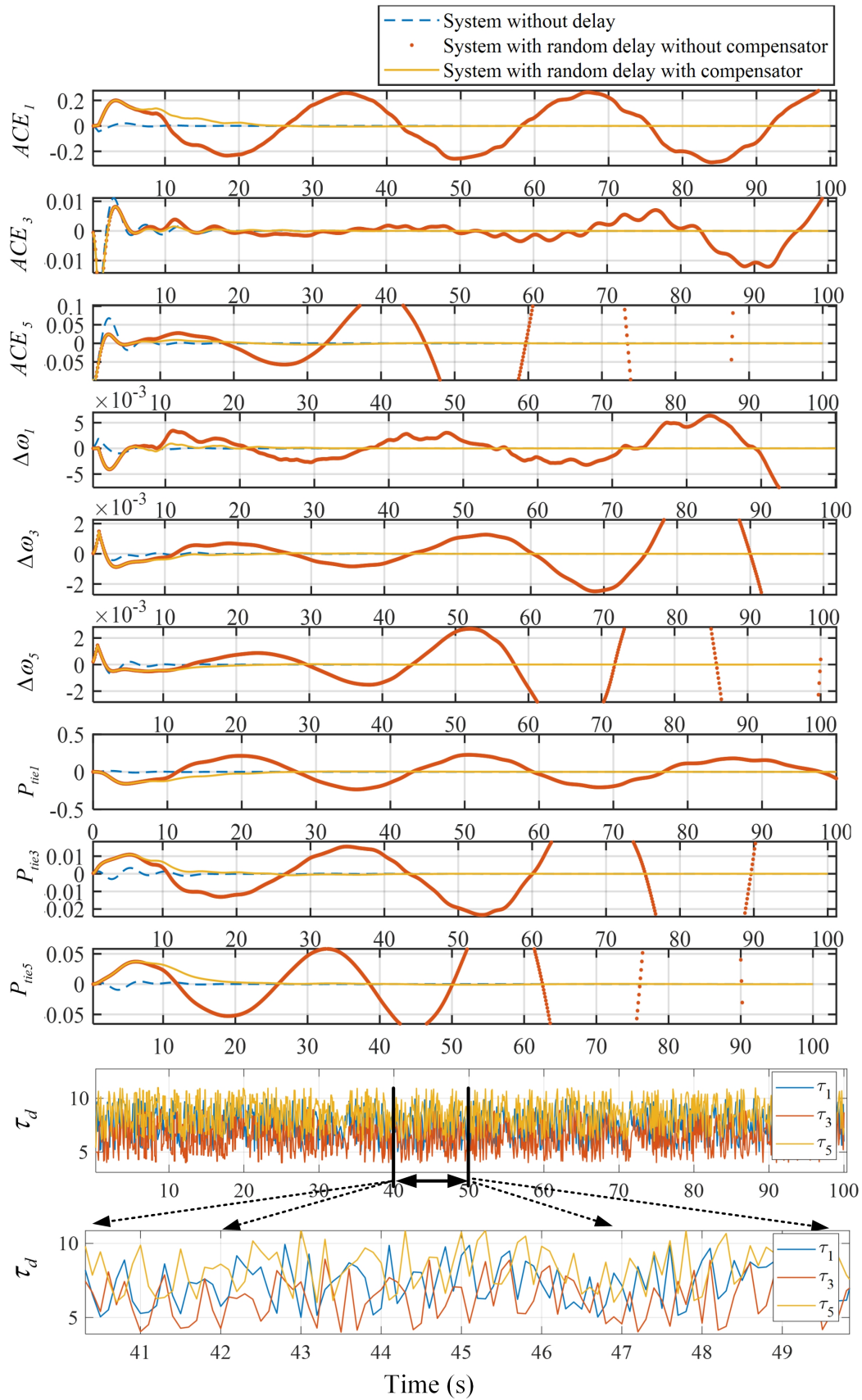


Figure 4.8: 10 area system LFC with random delay (Only three areas are shown. The time-varying random delays in these three areas are shown at the bottom of this figure).

different time-varying random delay was added to each area. As previously discussed, when the condition of (4.18) is met, the design process is much simplified for the ten-area system and the delay compensator for each area can be quickly designed based on the procedure give in Section 4.3.

By checking $\|\Delta_{10}\|_\infty$ and $1/\|N_{10}^{-1}\|_\infty$ of this ten-area system, we can find that the condition in (4.18) also holds. Hence, we can design the delay compensator for each control area separately. Only three areas' responses are shown in Fig. 4.8 with the τ_{max} in these three areas being 10s, 8s, 11s, respectively. The solid line indicates the proposed method can still mitigate the impact of time-varying random delay with a fast settling time and small oscillations. Nevertheless, it should be noted that the system can become more closely coupled when more control areas are connected together. More discussions on this are given in the following section.

4.4: Discussion

4.4.1: Comparison with LMI Method

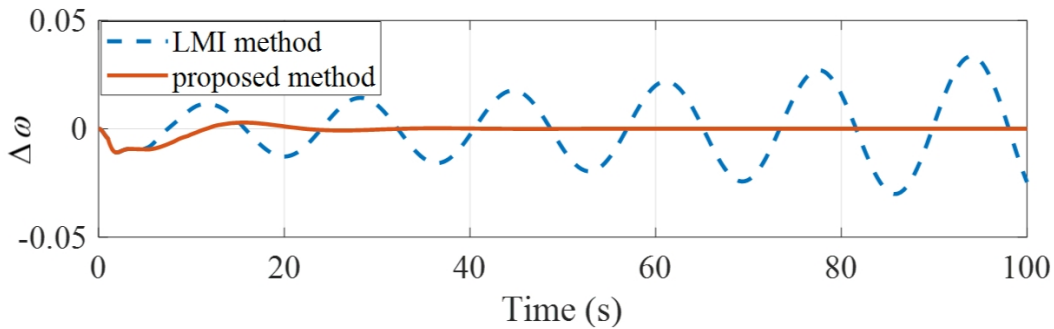


Figure 4.9: The comparison of the proposed method and LMI method when the delay $\tau=4.0s$.

As discussed in Section 4.2, a controller is guaranteed to be found by using the proposed approach since it provides the necessary and sufficient stability condition. In contrast, the widely-used LMI approaches proposed in [85, 89] only provide a sufficient

condition, which does not tell how to design a controller and can not guarantee its existence. The following example shows the advantages of our approach compared with the LMI method used in the LFC control in [89]. It was claimed in the paper that the LMI is feasible when $K_P = 0, K_I = 0.4$ for τ between [3.1s, 3.4s] by implementing Theorem 1 in [89]. In other words, if the delay keeps increasing and goes beyond its upper bound of 3.4s, e.g., $\tau = 4.0s$, the LMI approach will become infeasible. In that case, no controller can be found or designed by using the LMI approach. However, by applying the proposed method in this paper, a compensator can be identified for the same system when $\tau = 4.0s$. Simulation results shown in Fig. 4.9 clearly indicate the scenario mentioned above.

4.4.2: Couplings in Multi-area LFC Scheme

Couplings among different areas can significantly impact performance of the load frequency control for the entire system. Coupling are typically determined by the system topology (e.g., whether there is a tie-line and the corresponding line parameters), system operating condition (e.g., the synchronizing power coefficients), and system control parameters (e.g., the integral gains K_I). In this paper, (4.15) or (4.18) can be used to determine if the proposed method can still be used to design delay compensator for each area separately. An example is given in Fig. 4.10a to illustrate how the coupling index $I_n (\|\mathbf{N}_n^{-1}\mathbf{\Delta}_n\|_\infty)$ changes based on the number of areas increased. The example value of $\|\mathbf{N}_n^{-1}\mathbf{\Delta}_n\|_\infty$ has been calculated based on the following two assumptions:

1) For simplicity of analysis, each area is assumed to have the same set of parameters and the couplings between any two areas are the same.

2) In an n-area system, each area is connected with the other n-1 areas. In other words, every two areas are connected, which is the scenario with the strongest possible

coupling among different areas. Considering the H-infinity norm of a matrix is determined by its maximum sum of the elements in each row, interconnections between every two areas guarantee scenarios simulated representing the extreme condition of the coupling index I_n ($\|\mathbf{N}_n^{-1}\mathbf{\Delta}_n\|_\infty$) in a multi-area LFC scheme.

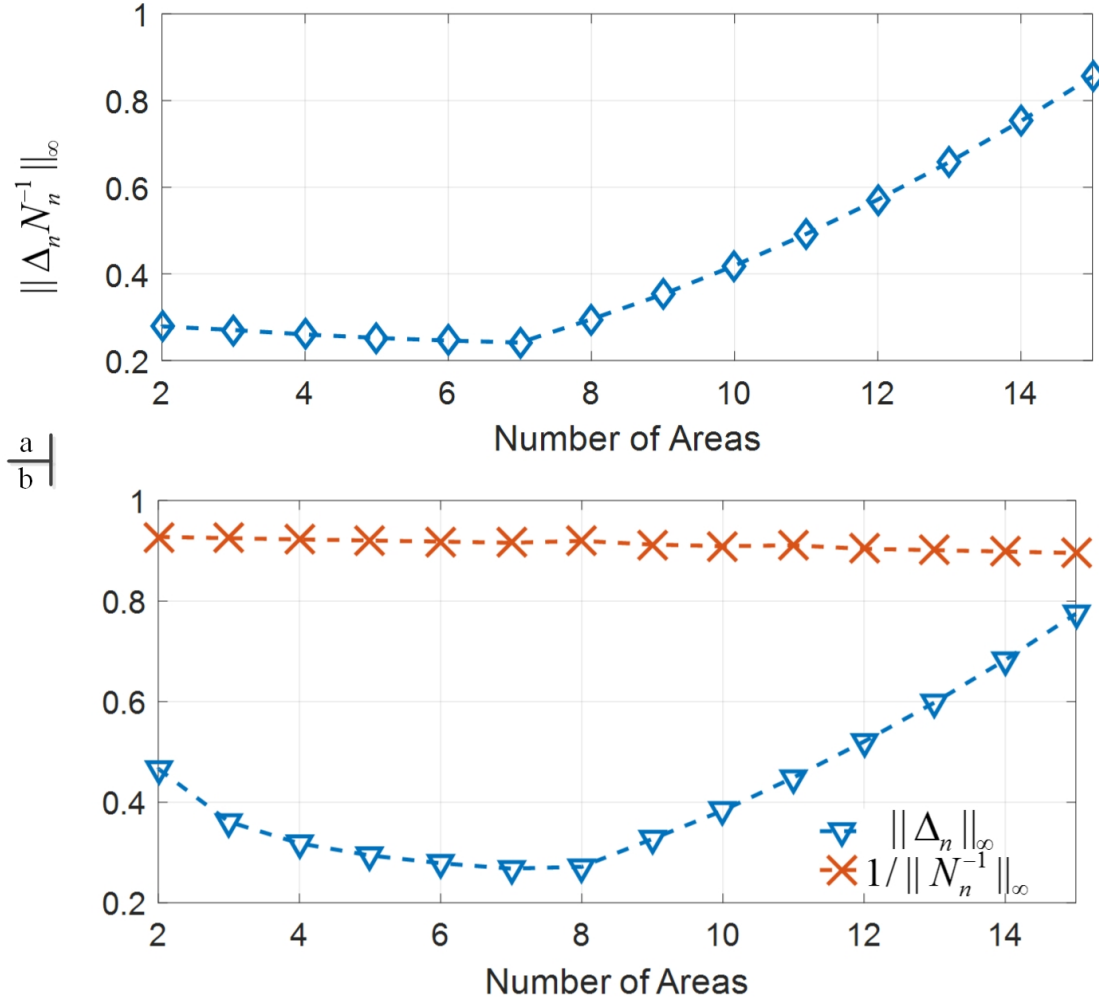


Figure 4.10: Calculated $\|\mathbf{N}_n^{-1}\mathbf{\Delta}_n\|_\infty$ value and comparison, up to 15-area LFC.

Fig. 4.10 shows that for the example multi-area systems, a delay compensator can be designed for each area independently without considering the coupling among areas since (4.18) is satisfied. Fig. 4.10 shows that as the number of areas increases, the value of $\|\mathbf{\Delta}_n\|_\infty$ is getting closer to $1/\|\mathbf{N}_n^{-1}\|_\infty$. Moreover, it is reasonable to assume that not all the sub areas are connected in a practical LFC scheme and this may also help

further decrease the value of $\|\mathbf{N}_n^{-1}\mathbf{\Delta}_n\|_\infty$. Nevertheless, a power system that has 15 control areas is sufficiently large. Thus, it is reasonable to conclude the proposed method is suitable for practical power systems.

CHAPTER 5: CONCLUSION

In this thesis, a novel Bayesian estimation based load modeling method is proposed. This method can accurately identify the distributions of each parameter in the composite load model composed by ZIP and IM sub-models. Compared with other measurement based algorithms, the proposed method can provide distribution estimations and is robust to measurement errors and outliers. The accuracy and robustness of the proposed method compared with some typical conventional load modeling method are also demonstrated by numerical experiments. The identified distributions can be further used in load prediction, stability and reliability analysis, as well as other related areas.

Then, the impact of communication delays in a distribution network with PV connected is also investigated. A detailed system model has been developed for a distribution network with distributed PVs to systematically analyze the impacts due to communication delays upon the voltage control of the distribution network. Based on the developed SISO system model, the maximum tolerable delay (i.e., delay margin) has been rigorously obtained for the system. Different from LMI based techniques, the proposed method establishes the necessary and sufficient condition for obtaining a controller based on the current system parameters to compensate the delay: the closed-loop system is stable if and only if $\tau_d < \varphi_\omega / \omega_c$. Simulation studies have been carried out first on a small radial feeder and then on a 33-bus system under different communication delays. The simulation results have verified the effectiveness of the proposed method in improving the system performance with both constant communication delays and time-varying delays in a switching system. The improved voltage regulation capability will ultimately help accommodate more PVs in distribution networks.

According to the method proposed in Chapter 3, the frequency control in large power

system considering delays has also been also studied. An alternative approach has been proposed for designing delay compensators for LFC schemes of large power systems with communication delays. The proposed method also gives a sufficient and necessary condition (i.e., $\tau < \varphi_\omega/\omega_c$) for designing delay compensator for a one-area LFC scheme. The study has also been extended to multi-area LFC schemes that covers a wide area. The criterion has been established based on the small gain theorem for designing controllers independently for individual areas/subsystems in a multi-area system while the overall system stability is guaranteed. If the criterion is met, the delay compensator design procedure can be much simplified since each area can just deal with its own time delay without using the information from other areas. The effectiveness of the proposed method has been verified by simulation studies under different scenarios for both one-area and multi-area LFC systems subject to random delays. Discussions have been given on the comparison of this method and typical LMI approaches. The couplings among different control areas have been further discussed for application of the proposed approach to bulk power systems.

The future work can be extended to include different renewable resources into the power grid in addition to solar power. Different renewable generators, such as wind farms, may bring in new challenges in the control design when delays involved. Moreover, artificial intelligence related technologies such as Reinforcement Learning (RL) and dynamic programming, can be studied for further improving the performance and capability of a power system in handling various delays. The future power system can be a measurement-driven, self-evolving, open platform, and machine learning based technologies can be a very good assistant to grid operators. For example, by implementing RL in voltage or frequency controls for power system, it is possible to generate the action-

rewards table for a trained system with/without considering impacts of delays, and thus significantly increasing the automation level of the power grid.

BIBLIOGRAPHY

- [1] “Renewable capacity statistics 2018,” accessed: 2019. [Online]. Available: <https://www.irena.org/publications/2018/Mar/Renewable-Capacity-Statistics-2018>
- [2] “A survey of wireless communications for the electric power system,” https://www.pnnl.gov/main/publications/external/technical_reports/PNNL-19084.pdf, accessed: 2017.
- [3] S. Xu, J. Lam, and X. Mao, “Delay-dependent h_∞ ; control and filtering for uncertain markovian jump systems with time-varying delays,” *IEEE Transactions on Circuits and Systems I: Regular Papers*, vol. 54, no. 9, pp. 2070–2077, Sept 2007.
- [4] B. A. Akyol, H. Kirkham, S. L. Clements, and M. D. Hadley, “A survey of wireless communications for the electric power system,” Pacific Northwest National Lab.(PNNL), Richland, WA (United States), Tech. Rep., 2010.
- [5] “Renewables 2018 global status report,” http://www.ren21.net/wp-content/uploads/2018/06/17-8652_GSR2018_FullReport_web_final_.pdf, accessed: 2019.
- [6] “Electric power monthly,” <https://www.eia.gov/electricity/monthly/>, accessed: 2017.
- [7] Electric power monthly. [Online]. Available: https://www.eia.gov/electricity/monthly/epm.table_grapher.php?t=epmt_1_01_a
- [8] T. Mai, D. Sandor, R. Wiser, and T. Schneider, “Renewable electricity futures study. executive summary,” National Renewable Energy Lab.(NREL), Golden, CO (United States), Tech. Rep., 2012.
- [9] G. Yuan, “Smart pv inverters—doe sunshot segis-ac program review,” in *2014 IEEE PES T&D Conference and Exposition*. IEEE, 2014, pp. 1–4.

- [10] A. Arif, Z. Wang, J. Wang, B. Mather, H. Bashualdo, and D. Zhao, “Load modeling – a review,” *IEEE Transactions on Smart Grid*, pp. 1–1, 2017.
- [11] X. Zhang, S. Grijalva, and M. J. Reno, “A time-variant load model based on smart meter data mining,” in *2014 IEEE PES General Meeting — Conference Exposition*, July 2014, pp. 1–5.
- [12] P. Kundur, N. J. Balu, and M. G. Lauby, *Power system stability and control*. McGraw-hill New York, 1994, vol. 7.
- [13] J.-K. Kim, K. An, J. Ma, J. Shin, K.-B. Song, J.-D. Park, J.-W. Park, and K. Hur, “Fast and reliable estimation of composite load model parameters using analytical similarity of parameter sensitivity,” *IEEE Transactions on Power Systems*, vol. 31, no. 1, pp. 663–671, 2016.
- [14] S. Alyami, C. Wang, and C. Fu, “Development of autonomous schedules of controllable loads for cost reduction and pv accommodation in residential distribution networks,” in *Electrical Power and Energy Conference (EPEC), 2015 IEEE*. IEEE, 2015, pp. 81–86.
- [15] J. Zhao, Y. Wang, C. Wang, F. Lin, and L. Y. Wang, “Maximizing the penetration of plug-in electric vehicles in distribution network,” in *Transportation Electrification Conference and Expo (ITEC), 2013 IEEE*. IEEE, 2013, pp. 1–6.
- [16] A. Arabali, M. Ghofrani, M. Etezadi-Amoli, M. S. Fadali, and Y. Baghzouz, “Genetic-algorithm-based optimization approach for energy management,” *IEEE Transactions on Power Delivery*, vol. 28, no. 1, pp. 162–170, 2013.
- [17] J. V. Milanovic, K. Yamashita, S. M. Villanueva, S. Djokic, and L. M. Korunović,

- “International industry practice on power system load modeling,” *IEEE Transactions on Power Systems*, vol. 28, no. 3, pp. 3038–3046, Aug 2013.
- [18] H. Renmu, M. Jin, and D. J. Hill, “Composite load modeling via measurement approach,” *IEEE Transactions on Power Systems*, vol. 21, no. 2, pp. 663–672, May 2006.
- [19] Z. Yu, L. McLaughlin, L. Jia, M. C. Murphy-Hoye, A. Pratt, and L. Tong, “Modeling and stochastic control for home energy management,” *IEEE Transactions on Smart Grid*, vol. 4, no. 4, pp. 2244–2255, 2012.
- [20] J. V. Milanović and S. M. Zali, “Validation of equivalent dynamic model of active distribution network cell,” *IEEE Transactions on Power Systems*, vol. 28, no. 3, pp. 2101–2110, Aug 2013.
- [21] Y. Ge, A. J. Flueck, D. K. Kim, J. B. Ahn, J. D. Lee, and D. Y. Kwon, “An event-oriented method for online load modeling based on synchrophasor data,” *IEEE Transactions on Smart Grid*, vol. 6, no. 4, pp. 2060–2068, July 2015.
- [22] J. K. Kim, K. An, J. Ma, J. Shin, K. B. Song, J. D. Park, J. W. Park, and K. Hur, “Fast and reliable estimation of composite load model parameters using analytical similarity of parameter sensitivity,” *IEEE Transactions on Power Systems*, vol. 31, no. 1, pp. 663–671, Jan 2016.
- [23] D. Shi, X. Chen, Z. Wang, X. Zhang, Z. Yu, X. Wang, and D. Bian, “A distributed cooperative control framework for synchronized reconnection of a multi-bus microgrid,” *IEEE Transactions on Smart Grid*, 2017.
- [24] D. Bian, M. Pipattanasomporn, and S. Rahman, “A human expert-based approach

- to electrical peak demand management,” *IEEE Transactions on Power Delivery*, vol. 30, no. 3, pp. 1119–1127, 2015.
- [25] D. Chen and R. R. Mohler, “Neural-network-based load modeling and its use in voltage stability analysis,” *IEEE Transactions on Control Systems Technology*, vol. 11, no. 4, pp. 460–470, 2003.
- [26] Y. Tang, S. Zhao, C.-W. Ten, and K. Zhang, “Enhancement of distribution load modeling using statistical hybrid regression,” in *Power & Energy Society Innovative Smart Grid Technologies Conference (ISGT), 2017 IEEE*. IEEE, 2017, pp. 1–5.
- [27] S.-H. Lee, S.-E. Son, S.-M. Lee, J.-M. Cho, K.-B. Song, and J.-W. Park, “Kalman-filter based static load modeling of real power system using k-ems data,” *Journal of Electrical Engineering and Technology*, vol. 7, no. 3, pp. 304–311, 2012.
- [28] Q. Liu, Y. Chen, and D. Duan, “The load modeling and parameters identification for voltage stability analysis,” in *Power System Technology, 2002. Proceedings. PowerCon 2002. International Conference on*, vol. 4. IEEE, 2002, pp. 2030–2033.
- [29] C. Fu, Z. Yu, and D. Shi, “Bayesian estimation based load modeling report,” <https://arxiv.org/abs/1810.07675>, 2018.
- [30] C. Wang, Z. Wang, J. Wang, and D. Zhao, “Robust time-varying parameter identification for composite load modeling,” *IEEE Transactions on Smart Grid*, pp. 1–1, 2017.
- [31] A. Patel, K. Wedeward, and M. Smith, “Parameter estimation for inventory of load models in electric power systems,” in *Proceedings of the World Congress on Engineering and Computer Science*, vol. 1, 2014, pp. 22–24.
- [32] Z. Yi, W. Dong, and A. H. Etemadi, “A unified control and power management

- scheme for pv-battery-based hybrid microgrids for both grid-connected and islanded modes,” *IEEE Transactions on Smart Grid*, vol. 9, no. 6, pp. 5975–5985, Nov 2018.
- [33] L. Meng, E. R. Sanseverino, A. Luna, T. Dragicevic, J. C. Vasquez, and J. M. Guerrero, “Microgrid supervisory controllers and energy management systems: A literature review,” *Renewable and Sustainable Energy Reviews*, vol. 60, pp. 1263 – 1273, 2016.
- [34] A. Karimi, M. Nayeripour, and M. Hassanzadeh, “Novel distributed active and reactive power management approach for renewable energy resource and loads in distribution network,” *Iranian Journal of Science and Technology, Transactions of Electrical Engineering*, pp. 1–21, 2018.
- [35] H. R. Baghaee, M. Mirsalim, G. B. Gharehpetian, and H. A. Talebi, “A decentralized power management and sliding mode control strategy for hybrid ac/dc microgrids including renewable energy resources,” *IEEE Transactions on Industrial Informatics*, 2017.
- [36] B. Rani, G. Saravana Ilango, and C. Nagamani, “Control strategy for power flow management in a pv system supplying dc loads,” *IEEE Transactions on Industrial Electronics*, vol. 60, no. 8, pp. 3185–3194, 2013, cited By 63. [Online]. Available: <https://www.scopus.com/inward/record.uri?eid=2-s2.0-84876246772&doi=10.1109/2fTIE.2012.2203772&partnerID=40&md5=34c41b13e9509091557d2416222555b4>
- [37] U. B. Tayab, M. A. B. Roslan, L. J. Hwai, and M. Kashif, “A review of droop control techniques for microgrid,” *Renewable and Sustainable Energy Reviews*, vol. 76, pp. 717 – 727, 2017. [Online]. Available: <http://www.sciencedirect.com/science/article/pii/S1364032117303453>

- [38] J. Duan, Z. Yi, D. Shi, C. Lin, X. Lu, and Z. Wang, “Reinforcement-learning-based optimal control for hybrid energy storage systems in hybrid ac/dc microgrids,” *IEEE Transactions on Industrial Informatics*, pp. 1–1, 2019.
- [39] Z. Yi, “Solar photovoltaic (pv) distributed generation systems-control and protection,” Ph.D. dissertation, The George Washington University, 2017.
- [40] Z. Yi and A. H. Etemadi, “A novel detection algorithm for line-to-line faults in photovoltaic (pv) arrays based on support vector machine (svm),” in *2016 IEEE Power and Energy Society General Meeting (PESGM)*, July 2016, pp. 1–4.
- [41] —, “Fault detection for photovoltaic systems based on multi-resolution signal decomposition and fuzzy inference systems,” *IEEE Transactions on Smart Grid*, vol. 8, no. 3, pp. 1274–1283, May 2017.
- [42] X. Liu, A. Aichhorn, L. Liu, and H. Li, “Coordinated control of distributed energy storage system with tap changer transformers for voltage rise mitigation under high photovoltaic penetration,” *IEEE Transactions on Smart Grid*, vol. 3, no. 2, pp. 897–906, June 2012.
- [43] C. L. Masters, “Voltage rise: the big issue when connecting embedded generation to long 11 kv overhead lines,” *Power Engineering Journal*, vol. 16, no. 1, pp. 5–12, Feb 2002.
- [44] Y. Ueda, K. Kurokawa, T. Tanabe, K. Kitamura, and H. Sugihara, “Analysis results of output power loss due to the grid voltage rise in grid-connected photovoltaic power generation systems,” *IEEE Transactions on Industrial Electronics*, vol. 55, no. 7, pp. 2744–2751, July 2008.
- [45] Y. Xu, W. Zhang, W. Liu, and F. Ferrese, “Multiagent-based reinforcement learning

- for optimal reactive power dispatch,” *IEEE Transactions on Systems, Man, and Cybernetics, Part C (Applications and Reviews)*, vol. 42, no. 6, pp. 1742–1751, 2012.
- [46] T. Yu, H. Wang, B. Zhou, K. Chan, and J. Tang, “Multi-agent correlated equilibrium $q(\lambda)$ learning for coordinated smart generation control of interconnected power grids,” *IEEE Transactions on Power Systems*, vol. 30, no. 4, pp. 1669–1679, 2015.
- [47] C. Wei, Z. Zhang, W. Qiao, and L. Qu, “Reinforcement-learning-based intelligent maximum power point tracking control for wind energy conversion systems,” *IEEE Transactions on Industrial Electronics*, vol. 62, no. 10, pp. 6360–6370, 2015.
- [48] R. Tonkoski, D. Turcotte, and T. H. M. EL-Fouly, “Impact of high pv penetration on voltage profiles in residential neighborhoods,” *IEEE Transactions on Sustainable Energy*, vol. 3, no. 3, pp. 518–527, July 2012.
- [49] R. A. Mastromauro, M. Liserre, and A. Dell’Aquila, “Control issues in single-stage photovoltaic systems: Mppt, current and voltage control,” *IEEE Transactions on Industrial Informatics*, vol. 8, no. 2, pp. 241–254, 2012.
- [50] Y. Ueda, K. Kurokawa, T. Tanabe, K. Kitamura, and H. Sugihara, “Analysis results of output power loss due to the grid voltage rise in grid-connected photovoltaic power generation systems,” *IEEE Transactions on Industrial Electronics*, vol. 55, no. 7, pp. 2744–2751, July 2008.
- [51] R. Tonkoski, L. A. C. Lopes, and T. H. M. El-Fouly, “Coordinated active power curtailment of grid connected pv inverters for overvoltage prevention,” *IEEE Transactions on Sustainable Energy*, vol. 2, no. 2, pp. 139–147, April 2011.

- [52] S. Alyami, Y. Wang, C. Wang, J. Zhao, and B. Zhao, “Adaptive real power capping method for fair overvoltage regulation of distribution networks with high penetration of pv systems,” *IEEE Transactions on Smart Grid*, vol. 5, no. 6, pp. 2729–2738, Nov 2014.
- [53] M. E. Baran and I. M. El-Markabi, “A multiagent-based dispatching scheme for distributed generators for voltage support on distribution feeders,” *IEEE Transactions on power systems*, vol. 22, no. 1, pp. 52–59, 2007.
- [54] W. K. Yap, L. Havas, E. Overend, and V. Karri, “Neural network-based active power curtailment for overvoltage prevention in low voltage feeders,” *Expert Systems with Applications*, vol. 41, no. 4, pp. 1063–1070, 2014.
- [55] O. Gagrica, P. H. Nguyen, W. L. Kling, and T. Uhl, “Microinverter curtailment strategy for increasing photovoltaic penetration in low-voltage networks,” *IEEE Transactions on Sustainable Energy*, vol. 6, no. 2, pp. 369–379, 2015.
- [56] L. Kane and G. W. Ault, “Evaluation of wind power curtailment in active network management schemes,” *IEEE Transactions on Power Systems*, vol. 30, no. 2, pp. 672–679, 2015.
- [57] Z. Yi and A. H. Etemadi, “Line-to-line fault detection for photovoltaic arrays based on multiresolution signal decomposition and two-stage support vector machine,” *IEEE Transactions on Industrial Electronics*, vol. 64, no. 11, pp. 8546–8556, Nov 2017.
- [58] B. Seal, “Common functions for smart inverters, version 3,” 2013.
- [59] F. L. Albuquerque, A. J. Moraes, G. C. Guimarães, S. M. Sanhueza, and A. R. Vaz, “Photovoltaic solar system connected to the electric power grid operating as active

- power generator and reactive power compensator,” *Solar Energy*, vol. 84, no. 7, pp. 1310–1317, 2010.
- [60] A. Ballanti, F. Pilo, A. Navarro-Espinosa, and L. F. Ochoa, “Assessing the benefits of pv var absorption on the hosting capacity of lv feeders,” in *Innovative Smart Grid Technologies Europe (ISGT EUROPE), 2013 4th IEEE/PES*. IEEE, 2013, pp. 1–5.
- [61] J. Zhao, Y. Wang, C. Wang, F. Lin, and L. Y. Wang, “Maximizing the penetration of plug-in electric vehicles in distribution network,” in *Transportation Electrification Conference and Expo (ITEC), 2013 IEEE*. IEEE, 2013, pp. 1–6.
- [62] B. Zhao, z. Xu, C. Xu, C. Wang, and F. Lin, “Network partition based zonal voltage control for distribution networks with distributed pv systems,” *IEEE Trans. Smart Grid*, vol. PP, no. 99, pp. 1–1, 2017.
- [63] K. Benjelloun and E. K. Boukas, “Mean square stochastic stability of linear time-delay system with markovian jumping parameters,” *IEEE Transactions on Automatic Control*, vol. 43, no. 10, pp. 1456–1460, Oct 1998.
- [64] M. Dahleh and M. A. Dahleh, “On slowly time-varying systems,” *Automatica*, vol. 27, no. 1, pp. 201 – 205, 1991.
- [65] L. Y. Wang and G. Zames, “Local-global double algebras for slow h infin; adaptation. ii. optimization of stable plants,” *IEEE Transactions on Automatic Control*, vol. 36, no. 2, pp. 143–151, Feb 1991.
- [66] “Ieee standard for interconnecting distributed resources with electric power systems,” *IEEE Std 1547-2003*, pp. 1–28, July 2003.
- [67] H. M. Ayres, W. Freitas, M. C. D. Almeida, and L. C. P. D. Silva, “Method for de-

- termining the maximum allowable penetration level of distributed generation without steady-state voltage violations,” *IET Generation, Transmission Distribution*, vol. 4, no. 4, pp. 495–508, April 2010.
- [68] F. Dinger, “The analysis on photovoltaic electricity generation status, potential and policies of the leading countries in solar energy,” *Renewable and Sustainable Energy Reviews*, vol. 15, no. 1, pp. 713 – 720, 2011.
- [69] D. Bian, M. Kuzlu, M. Pipattanasomporn, S. Rahman, and Y. Wu, “Real-time co-simulation platform using opal-rt and opnet for analyzing smart grid performance,” in *2015 IEEE Power & Energy Society General Meeting*. IEEE, 2015, pp. 1–5.
- [70] D. Bian, M. Kuzlu, M. Pipattanasomporn, and S. Rahman, “Assessment of communication technologies for a home energy management system,” in *ISGT 2014*. IEEE, 2014, pp. 1–5.
- [71] —, “Analysis of communication schemes for advanced metering infrastructure (ami),” in *2014 IEEE PES General Meeting— Conference & Exposition*. IEEE, 2014, pp. 1–5.
- [72] D. Bian, M. Kuzlu, M. Pipattanasomporn, S. Rahman, and D. Shi, “Performance evaluation of communication technologies and network structure for smart grid applications,” *arXiv preprint arXiv:1901.11509*, 2019.
- [73] Y. Yan, D. Shi, D. Bian, B. Huang, Z. Yi, and Z. Wang, “Small-signal stability analysis and performance evaluation of microgrids under distributed control,” *IEEE Transactions on Smart Grid*, 2018.
- [74] L. Mirkin and Z. J. Palmor, “Control issues in systems with loop delays,” *Handbook of Networked and Embedded Control Systems*, pp. 627–648, 2005.

- [75] “Ieee standard for synchrophasors for power systems,” *IEEE Std C37.118-2005 (Revision of IEEE Std 1344-1995)*, pp. 01–57, 2006.
- [76] H. Wu, K. S. Tsakalis, and G. T. Heydt, “Evaluation of time delay effects to wide-area power system stabilizer design,” *IEEE Transactions on Power Systems*, vol. 19, no. 4, pp. 1935–1941, Nov 2004.
- [77] A. K. Singh and B. C. Pal. (2013) IEEE PES Task Force on Benchmark Systems for Stability Controls Report on the 68-bus, 16-machine, 5-area system. [Online]. Available: <http://eioc.pnnl.gov/benchmark/ieeess/>
- [78] R. Dey, S. Ghosh, G. Ray, and A. Rakshit, “ H_∞ load frequency control of interconnected power systems with communication delays,” *International Journal of Electrical Power & Energy Systems*, vol. 42, no. 1, pp. 672 – 684, 2012.
- [79] K. Zhou, J. C. Doyle, K. Glover *et al.*, *Robust and optimal control*. Prentice Hall Upper Saddle River, NJ, 1996, vol. 40.
- [80] G. Zames, “On the input-output stability of time-varying nonlinear feedback systems part one: Conditions derived using concepts of loop gain, conicity, and positivity,” *IEEE Transactions on Automatic Control*, vol. 11, no. 2, pp. 228–238, Apr 1966.
- [81] X.-M. Zhang, Q.-L. Han, and X. Yu, “Survey on recent advances in networked control systems,” *IEEE Transactions on Industrial Informatics*, vol. 12, no. 5, pp. 1740–1752, 2016.
- [82] H. Ali and D. Dasgupta, “Effects of time delays in the electric power grid,” in *International Conference on Critical Infrastructure Protection*. Springer, 2012, pp. 139–154.

- [83] J. Zhang and A. D. Domínguez-García, “On the impact of communication delays on power system automatic generation control performance,” in *2014 North American Power Symposium (NAPS)*, Sept 2014, pp. 1–6.
- [84] B. Naduvathuparambil, M. C. Valenti, and A. Feliachi, “Communication delays in wide area measurement systems,” in *Proceedings of the Thirty-Fourth Southeastern Symposium on System Theory (Cat. No.02EX540)*, 2002, pp. 118–122.
- [85] K. Tomsovic, D. E. Bakken, V. Venkatasubramanian, and A. Bose, “Designing the next generation of real-time control, communication, and computations for large power systems,” *Proceedings of the IEEE*, vol. 93, no. 5, pp. 965–979, May 2005.
- [86] H. Bevrani and T. Hiyama, “On load - frequency regulation with time delays: Design and real-time implementation,” *IEEE Transactions on Energy Conversion*, vol. 24, no. 1, pp. 292–300, March 2009.
- [87] Ibraheem, P. Kumar, and D. P. Kothari, “Recent philosophies of automatic generation control strategies in power systems,” *IEEE Transactions on Power Systems*, vol. 20, no. 1, pp. 346–357, Feb 2005.
- [88] X. Yu and K. Tomsovic, “Application of linear matrix inequalities for load frequency control with communication delays,” *IEEE Transactions on Power Systems*, vol. 19, no. 3, pp. 1508–1515, Aug 2004.
- [89] L. Jiang, W. Yao, Q. H. Wu, J. Y. Wen, and S. J. Cheng, “Delay-dependent stability for load frequency control with constant and time-varying delays,” *IEEE Transactions on Power Systems*, vol. 27, no. 2, pp. 932–941, May 2012.
- [90] C. K. Zhang, L. Jiang, Q. H. Wu, Y. He, and M. Wu, “Delay-dependent robust

- load frequency control for time delay power systems,” *IEEE Transactions on Power Systems*, vol. 28, no. 3, pp. 2192–2201, Aug 2013.
- [91] S. Wen, X. Yu, Z. Zeng, and J. Wang, “Event-triggering load frequency control for multiarea power systems with communication delays,” *IEEE Transactions on Industrial Electronics*, vol. 63, no. 2, pp. 1308–1317, Feb 2016.
- [92] B. Naduvathuparambil, M. C. Valenti, and A. Feliachi, “Communication delays in wide area measurement systems,” in *Proceedings of the Thirty-Fourth Southeastern Symposium on System Theory*, 2002, pp. 118–122.
- [93] G. Beale, “Phase lead compensator design using bode plots,” *Course Literature*, 2008.
- [94] Y. Zhang, L. Dong, and Z. Gao, “Load frequency control for multiple-area power systems,” in *American Control Conference, 2009. ACC’09*. IEEE, 2009, pp. 2773–2778.
- [95] M. Thomson and D. G. Infield, “Network power-flow analysis for a high penetration of distributed generation,” *IEEE Transactions on Power Systems*, vol. 22, no. 3, pp. 1157–1162, 2007.
- [96] H. Saadat, *Power System Analysis*. The McGraw-Hill Companies, 1999.
- [97] X. Yu and K. Tomsovic, “Application of linear matrix inequalities for load frequency control with communication delays,” *IEEE Transactions on Power Systems*, vol. 19, no. 3, pp. 1508–1515, Aug 2004.
- [98] C. Dou, D. Yue, J. M. Guerrero, X. Xie, and S. Hu, “Multiagent system-based distributed coordinated control for radial dc microgrid considering transmission time delays,” *IEEE Transactions on Smart Grid*, vol. PP, no. 99, pp. 1–12, 2016.

- [99] L. Jiang, W. Yao, Q. H. Wu, J. Y. Wen, and S. J. Cheng, “Delay-dependent stability for load frequency control with constant and time-varying delays,” *IEEE Transactions on Power Systems*, vol. 27, no. 2, pp. 932–941, May 2012.
- [100] S. Weckx, C. Gonzalez, and J. Driesen, “Combined central and local active and reactive power control of pv inverters,” *IEEE Transactions on Sustainable Energy*, vol. 5, no. 3, pp. 776–784, July 2014.
- [101] T. Esum and P. L. Chapman, “Comparison of photovoltaic array maximum power point tracking techniques,” *IEEE Transactions on Energy Conversion*, vol. 22, no. 2, pp. 439–449, June 2007.
- [102] X. Liu, A. Aichhorn, L. Liu, and H. Li, “Coordinated control of distributed energy storage system with tap changer transformers for voltage rise mitigation under high photovoltaic penetration,” *IEEE Transactions on Smart Grid*, vol. 3, no. 2, pp. 897–906, June 2012.
- [103] H. Wirth and K. Schneider, “Recent facts about photovoltaics in germany,” *Fraunhofer ISE*, p. 92, 2015.
- [104] S. Moosavian, N. Rahim, J. Selvaraj, and K. Solangi, “Energy policy to promote photovoltaic generation,” *Renewable and Sustainable Energy Reviews*, vol. 25, pp. 44 – 58, 2013.
- [105] M. Wu, Y. He, J.-H. She, and G.-P. Liu, “Delay-dependent criteria for robust stability of time-varying delay systems,” *Automatica*, vol. 40, no. 8, pp. 1435 – 1439, 2004.
- [106] D. Bian, M. Pipattanasomporn, and S. Rahman, “A human expert-based approach

- to electrical peak demand management,” *IEEE Transactions on Power Delivery*, vol. 30, no. 3, pp. 1119–1127, 2015.
- [107] D. Bian, D. Shi, M. Pipattanasomporn, M. Kuzlu, and S. Rahman, “Mitigating the impact of renewable variability with demand-side resources considering communication and cyber security limitations,” *IEEE Access*, vol. 7, pp. 1379–1389, 2019.
- [108] Z. Liang, D. Bian, X. Zhang, D. Shi, R. Diao, and Z. Wang, “Optimal energy management for commercial buildings considering comprehensive comfort levels in a retail electricity market,” *Applied Energy*, vol. 236, pp. 916–926, 2019.
- [109] D. Shi, X. Chen, Z. Wang, X. Zhang, Z. Yu, X. Wang, and D. Bian, “A distributed cooperative control framework for synchronized reconnection of a multi-bus microgrid,” *IEEE Transactions on Smart Grid*, vol. 9, no. 6, pp. 6646–6655, 2018.
- [110] X. Zhang, D. Shi, Z. Wang, Z. Yu, X. Wang, D. Bian, and K. Tomsovic, “Bilevel optimization based transmission expansion planning considering phase shifting transformer,” in *2017 North American Power Symposium (NAPS)*. IEEE, 2017, pp. 1–6.
- [111] S. P. Meyn and R. L. Tweedie, *Markov chains and stochastic stability*. Springer Science & Business Media, 2012.
- [112] D. Singh and R. Misra, “Effect of load models in distributed generation planning,” *IEEE Transactions on Power Systems*, vol. 22, no. 4, pp. 2204–2212, 2007.
- [113] N. Terkovic, S. A. Neild, M. Lowenberg, and R. Szalai, “Substructurability: the effect of interface location on a real-time dynamic substructuring test,” *Proceedings*

of the Royal Society of London A: Mathematical, Physical and Engineering Sciences, vol. 472, no. 2192, 2016.

- [114] P. Park, “A delay-dependent stability criterion for systems with uncertain time-invariant delays,” *IEEE Transactions on Automatic Control*, vol. 44, no. 4, pp. 876–877, Apr 1999.
- [115] K. Zhou, J. C. Doyle, K. Glover *et al.*, *Robust and optimal control*. Prentice hall New Jersey, 1996, vol. 40.
- [116] W. D. Wang, C. L. Zhang, W. J. Wang, and C. Fu, “Study of slime water concentration measurement and influencing factors with ultrasonic attenuation theory,” in *Advanced Materials Research*, vol. 347. Trans Tech Publ, 2012, pp. 1764–1768.
- [117] “U.s. renewable energy technical potentials: A gis-based analysis,” <https://www.nrel.gov/docs/fy12osti/51946.pdf>, accessed: 2017.
- [118] “Photovoltaics,” <https://en.wikipedia.org/wiki/Photovoltaics>, accessed: 2017.
- [119] “Solar cells,” <http://www.chemistryexplained.com/Ru-Sp/Solar-Cells.html>, accessed: 2017.
- [120] “An introduction to solar cell introduction,” <https://archive.cnx.org/contents/dd0537a2-fb5d-439d-8feb-bf2e50656dae@1/an-introduction-to-solar-cell-technology#id1170062050442>, accessed: 2017.
- [121] “Solar cell,” https://en.wikipedia.org/wiki/Solar_cell, accessed: 2017.
- [122] “Sunshot 2030,” accessed: 2017. [Online]. Available: <https://energy.gov/eere/solar/sunshot-2030>
- [123] M. A. Green, K. Emery, Y. Hishikawa, W. Warta, and E. D. Dunlop, “Solar cell

- efficiency tables (version 45),” *Progress in photovoltaics: research and applications*, vol. 23, no. 1, pp. 1–9, 2015.
- [124] “Control issues in systems with loop delays,” <http://leo.technion.ac.il/publications/LoopDelayTutor/LoopDelayT.pdf>, accessed: 2017.
- [125] C. Dou, D. Yue, J. M. Guerrero, X. Xie, and S. Hu, “Multiagent system-based distributed coordinated control for radial dc microgrid considering transmission time delays,” *IEEE Transactions on Smart Grid*, vol. 8, no. 5, pp. 2370–2381, Sept 2017.
- [126] P. N. Vovos, A. E. Kiprakis, A. R. Wallace, and G. P. Harrison, “Centralized and distributed voltage control: Impact on distributed generation penetration,” *IEEE Transactions on Power Systems*, vol. 22, no. 1, pp. 476–483, Feb 2007.
- [127] S. Weckx and J. Driesen, “Optimal local reactive power control by pv inverters,” *IEEE Transactions on Sustainable Energy*, vol. 7, no. 4, pp. 1624–1633, Oct 2016.
- [128] Renewable 2016 global status report. [Online]. Available: <http://www.ren21.net/status-of-renewables/global-status-report/>
- [129] Optimal materials and deposition technique lead to cost-effective solar cell with best-ever conversion efficiency. [Online]. Available: <http://www.nrel.gov/docs/fy12osti/55741.pdf>
- [130] M. Hosenuzzaman, N. Rahim, J. Selvaraj, M. Hasanuzzaman, A. Malek, and A. Nahar, “Global prospects, progress, policies, and environmental impact of solar photovoltaic power generation,” *Renewable and Sustainable Energy Reviews*, vol. 41, pp. 284 – 297, 2015.
- [131] E. J. Coster, J. M. Myrzik, B. Kruimer, and W. L. Kling, “Integration issues of

- distributed generation in distribution grids,” *Proceedings of the IEEE*, vol. 99, no. 1, pp. 28–39, 2011.
- [132] Y. P. Agalgaonkar, B. C. Pal, and R. A. Jabr, “Distribution voltage control considering the impact of pv generation on tap changers and autonomous regulators,” *IEEE Transactions on Power Systems*, vol. 29, no. 1, pp. 182–192, 2014.
- [133] O. Homaei, A. Zakariazadeh, and S. Jadid, “Real-time voltage control algorithm with switched capacitors in smart distribution system in presence of renewable generations,” *International Journal of Electrical Power & Energy Systems*, vol. 54, pp. 187–197, 2014.
- [134] M. Oshiro, K. Tanaka, A. Uehara, T. Senjyu, Y. Miyazato, A. Yona, and T. Funabashi, “Optimal voltage control in distribution systems with coordination of distribution installations,” *International Journal of Electrical Power & Energy Systems*, vol. 32, no. 10, pp. 1125–1134, 2010.
- [135] R. Caldon, M. Coppo, and R. Turri, “Coordinated voltage control in mv and lv distribution networks with inverter-interfaced users,” in *PowerTech (POWERTECH), 2013 IEEE Grenoble*. IEEE, 2013, pp. 1–5.
- [136] L. Carradore and R. Turri, “Distributed co-ordinated power management in mv electrical networks,” in *Universities Power Engineering Conference (UPEC), 2010 45th International*. IEEE, 2010, pp. 1–5.
- [137] China targets 70 gigawatts of solar power to cut coal reliance. [Online]. Available: <https://www.bloomberg.com/news/articles/2014-05-16/china-targets-70-gigawatts-of-solar-power-to-cut-coal-reliance>
- [138] N. Terkovics, S. A. Neild, M. Lowenberg, R. Szalai, and B. Krauskopf, “Substruc-

- turability: the effect of interface location on a real-time dynamic substructuring test,” *Proceedings of the Royal Society of London A: Mathematical, Physical and Engineering Sciences*, vol. 472, no. 2192, 2016.
- [139] D. Chen and R. R. Mohler, “Neural-network-based load modeling and its use in voltage stability analysis,” *IEEE Transactions on Control Systems Technology*, vol. 11, no. 4, pp. 460–470, 2003.
- [140] L. M. Hajagos and B. Danai, “Laboratory measurements and models of modern loads and their effect on voltage stability studies,” *IEEE Transactions on Power Systems*, vol. 13, no. 2, pp. 584–592, May 1998.
- [141] S. M. Lynch, *Introduction to applied Bayesian statistics and estimation for social scientists*. Springer Science & Business Media, 2007.
- [142] J. A. Paulos, “The mathematics of changing your mind,” *New York Times (US)*, 2011.
- [143] R. Al Abri, E. F. El-Saadany, and Y. M. Atwa, “Optimal placement and sizing method to improve the voltage stability margin in a distribution system using distributed generation,” *IEEE transactions on power systems*, vol. 28, no. 1, pp. 326–334, 2013.
- [144] J. Zhao, Z. Wang, and J. Wang, “Robust time-varying load modeling for conservation voltage reduction assessment,” *IEEE Transactions on Smart Grid*, vol. 9, no. 4, pp. 3304–3312, July 2018.
- [145] Y. Bao, L. Y. Wang, C. Wang, and Y. Wang, “Hammerstein models and real-time system identification of load dynamics for voltage management,” *IEEE Access*, vol. 6, pp. 34 598–34 607, 2018.

- [146] G. W. Chang, C. I. Chen, and Y. J. Liu, "A neural-network-based method of modeling electric arc furnace load for power engineering study," *IEEE Transactions on Power Systems*, vol. 25, no. 1, pp. 138–146, Feb 2010.
- [147] V. Vignesh, S. Chakrabarti, and S. Srivastava, "Classification and modelling of loads in power systems using svm and optimization approach," in *Power & Energy Society General Meeting, 2015 IEEE*. IEEE, 2015, pp. 1–5.
- [148] C. M. Carlo, "Markov chain monte carlo and gibbs sampling," *Lecture notes for EEB*, vol. 581, 2004.
- [149] C. Fu, C. Wang, and S. Alyami, "An lmi based stability margin analysis for active pv power control of distribution networks with time-invariant delays," *arXiv preprint arXiv:1804.06903*, 2018.
- [150] J. Zhao, Y. Wang, C. Wang, F. Lin, and L. Y. Wang, "Maximizing the penetration of plug-in electric vehicles in distribution network," in *2013 IEEE Transportation Electrification Conference and Expo (ITEC)*, June 2013, pp. 1–6.
- [151] M. C. Best, T. Gordon, and P. Dixon, "An extended adaptive kalman filter for real-time state estimation of vehicle handling dynamics," *Vehicle System Dynamics*, vol. 34, no. 1, pp. 57–75, 2000.
- [152] C.-W. Ten and Y. Tang, *Electric Power: Distribution Emergency Operation*. CRC Press, 2018.

PUBLICATIONS

1. Li, Haifeng , Chen, Qing , Fu, Chang , Yu, Zhe , Shi, Di and Wang, Zhiwei, “Bayesian Estimation on Load Model Coefficients of ZIP and Induction Motor Model” *Energies*, vol. 12, no. 3, pp 547, 2019.
2. Fu, Chang, Yu, Zhe, Shi, Di, Li, Haifeng, Wang, Caisheng and Wang, Zhiwei, “Bayesian Estimation Based Parameter Estimation for Composite Load” *Accepted by 2019 IEEE Power & Energy society General Meeting*, 2019
3. Fu, Chang , Wang, Caisheng and Alyami, Saeed , “An LMI Based Stability Margin Analysis for Active PV Power Control of Distribution Networks with Time-Invariant Delays” *2018 IEEE Power Energy Society General Meeting (PESGM)*, Aug 2018.
4. Zhao, Zhongyang, Fu, Chang, Wang, Caisheng, and Miller, Carol J., “Improvement to the Prediction of Fuel Cost Distributions Using ARIMA Model” *2018 IEEE Power Energy Society General Meeting (PESGM)*, Aug. 2018, DOI: 10.1109/PESGM.2018.858598
5. Fu, Chang, Wang, Caisheng, Miller, Carol J. and Wang, Yang. “Characterization and distribution model for fuel costs in electricity market” *2017 International Energy and Sustainability Conference (IESC)*, Oct. 2017, DOI: 10.1109/IESC.2017.8167479.
6. Alyami, Saeed , Wang, Caisheng and Fu, Chang, “Development of autonomous schedules of controllable loads for cost reduction and pv accommodation in residential distribution networks” *2015 IEEE Electrical Power and Energy Conference (EPEC)*, 2015, DOI: 10.1109/EPEC.2015.7379931

7. Fu, Chang, Wang, Caisheng, Wang, Leyi, and Shi, Di. "An Alternative Method for Multi-area Load Frequency Control with Communication Delays", Under Review.
8. Fu, Chang, Wang, Caisheng and Wang, Leyi, "Active PV Power Control with Communication Delay for Voltage Regulation of Distribution Networks", Under Review.

Posters Presented

1. Fu, Chang, "An LMI Based Stability Margin Analysis for Active PV Power Control of Distribution Networks with Time-Invariant Delays," *2018 IEEE Power Energy Society General Meeting*, Aug 11, 2018, Portland, OR, USA.
2. Fu, Chang, "Active PV Power Control with Communication Delay for Voltage Regulation of Distribution Networks," *2017 IEEE Power Energy Society General Meeting*, Aug 13, 2017, Chicago, IL, USA.
3. Fu, Chang, "Reliability evaluation of Battery Energy Storage," *IEEE Southeast Michigan section (SEM) fall conference*, Nov.17, 2015, U-M Dearborn, MI, USA.
4. Fu, Chang, "Characterization and Prediction of Fuel Costs for Electrical Power Generation," *Big data & business analytics symposium*, March 23-24, 2016, Wayne State University, Detroit, MI, USA.

Patent

1. Yu, Zhe, Wang, Yishen, Li, Haifeng, Fu, Chang, Wang, Zhiwei, and Shi, Di. "An Approach of Parameter Estimation for Composite Load Based on Bayesian Estimation", Patent Application Number: US 62/756.387

ABSTRACT**ANALYSIS AND MITIGATION OF THE IMPACTS OF DELAYS IN
CONTROL OF POWER SYSTEMS WITH RENEWABLE ENERGY
SOURCES**

by

CHANG FU**August 2019****Advisor** : Dr. Caisheng Wang**Major** : Electrical and Computer Engineering**Degree** : Doctor of Philosophy

With the integration of renewable resources, electric vehicles and other uncertain resources into the power grid, a variety of control methodologies and algorithms have been proposed to increase the stability and reliability of the operation system. Load modeling is a critical part of such analysis since it significantly impacts the accuracy of the simulation in power system, as well as stability and reliability analysis. Traditional composite load model parameter identification problems in the power system can be essentially ascribed to optimization problems, and the identified parameters are point estimations subject to different constraints. These conventional point estimation based composite load modeling approaches suffer from disturbances and noises and provide limited information on the system dynamics. In this thesis, a statistic (Bayesian Estimation) based distribution estimation approach is proposed for developing composite load models, including static (ZIP) and dynamic (Induction Motor) parts, by implementing the Gibbs sampling. The proposed method provides a distribution estimation of coefficients for load models and is robust to measurement errors.

Overvoltage is another urgent issue that needs to be addressed, especially in a high PV

penetration level system. Various approaches including the real power control through photovoltaic (PV) inverters have been proposed to mitigate such impact. However, most of the existing methods did not include communication delays in the control loop. Communication delays, short or long, are inevitable in the PV voltage regulation loop and can not only deteriorate the system performance with undesired voltage quality but also cause system instability. In this thesis, a method is presented to convert the overvoltage control problem via PV inverters for multiple PVs into a problem of single-input-single-output (SISO) systems. The method can handle multiple PVs and different communication delays. The impact of communication delays is also systematically analyzed, and the maximum tolerable delay is rigorously obtained. Different from linear matrix inequality (LMI) techniques that have been extensively studied in handling systems with communication delays, the proposed method gives the necessary and sufficient condition for obtaining a controller, and the design procedure is explicitly and constructively given in the paper. The effectiveness of the proposed method is verified by the simulation studies on a distribution feeder and the widely-used 33-bus distribution test system.

The similar design strategy can be utilized to mitigate delay impacts in Load frequency control (LFC) as well. LFC has been considered as one of the most important frequency regulation mechanisms in modern power systems. One of the inevitable problems involved in LFC over a wide area is communication delay. In this thesis, an alternative design method is proposed to devise delay compensators for LFC in one or multiple control areas. For one-area LFC, a sufficient and necessary condition is given for designing a delay compensator. For multi-area LFC with area control errors (ACEs), it is demonstrated that each control area can have its delay controller designed as that in a one-area system if the index of coupling among the areas is below the threshold value determined by the

small gain theorem. The effectiveness of the proposed method is verified by the simulation studies on LFCs with communication delays in one and multiple interconnected areas with and without time-varying delays, respectively.

AUTOBIOGRAPHICAL STATEMENT

Education

PhD	Wayne State University, Detroit, MI, USA	2019
M.S.	China University of Mining & Technology, Beijing, China	2013
B.S.	Hefei University of Technology, Hefei, Anhui, China	2009

Personal Details

Full Name	Chang Fu
E-mail Address	changfuapply4job@gmail.com
Date of Birth (mm/dd/yyyy)	03/24/1987
City of Birth	Huainan Anhui
Country of Birth	China

Work Experience

May 2018 - Dec 2018	Associate Researcher, GEIRINA, San Jose, CA, USA
Sep 2014 - May 2018	Graduate Teaching Assistant, Wayne State University, Detroit, USA